NAVAL POSTGRADUATE SCHOOL

MONTEREY, CALIFORNIA

THESIS

FORWARD ERROR CORRECTION ENCODING ON THE MULTIPLE INPUT/MULTIPLE OUTPUT FREE SPACE OPTICAL COMMUNICATIONS CHANNEL

by

Paul C. Keeley

June 2019

Thesis Advisor:	Raymond R. Buettner Jr.
Co-Advisor:	David R. Canright
Second Reader:	Peter R. Ateshian

THIS PAGE INTENTIONALLY LEFT BLANK

REPORT DOCUMENTATION PAGE			*Form Approved OMB No. 0704-0188*

1. AGENCY USE ONLY *(Leave blank)*	**2. REPORT DATE** June 2019	**3. REPORT TYPE AND DATES COVERED** Master's thesis

4. TITLE AND SUBTITLE
FORWARD ERROR CORRECTION ENCODING ON THE MULTIPLE INPUT/MULTIPLE OUTPUT FREE SPACE OPTICAL COMMUNICATIONS CHANNEL

5. FUNDING NUMBERS

6. AUTHOR(S) Paul C. Keeley

7. PERFORMING ORGANIZATION NAME(S) AND ADDRESS(ES)
Naval Postgraduate School
Monterey, CA 93943-5000

8. PERFORMING ORGANIZATION REPORT NUMBER

9. SPONSORING / MONITORING AGENCY NAME(S) AND ADDRESS(ES)
N/A

10. SPONSORING / MONITORING AGENCY REPORT NUMBER

11. SUPPLEMENTARY NOTES The views expressed in this thesis are those of the author and do not reflect the official policy or position of the Department of Defense or the U.S. Government.

12a. DISTRIBUTION / AVAILABILITY STATEMENT
Approved for public release. Distribution is unlimited.

12b. DISTRIBUTION CODE
A

13. ABSTRACT (maximum 200 words)

As a high bandwidth, narrow beamwidth channel, free space optical (FSO) communications can potentially achieve high data rates with a low probability of detection and intercept. However, in addition to the additive white Gaussian noise typical of radio frequency communications, atmospheric turbulence adds random, relatively long duration fades to the channel, which significantly decrease overall throughput. This thesis explores how various forward error correction (FEC) techniques affect the channel capacity of a multiple input/multiple output (MIMO) system. A statistical model of the channel is developed from the existing literature. Thirteen coding and modulation schemes are implemented in software and tested against this channel model under different simulated levels of noise and turbulence. Codes are compared by characteristics such as energy per bit and outage thresholds to determine which characteristics of the different codes most critically affect performance. Key performance indicators for each code include average bit error rate, overall throughput, and variability. A recommendation is made to implement variable-level coding in future advanced technology demonstrators or prototypes developed for the FSO MIMO system.

14. SUBJECT TERMS free space optical communications, forward error correction, low probability of intercept, low probability of detect	**15. NUMBER OF PAGES** 171
	16. PRICE CODE

17. SECURITY CLASSIFICATION OF REPORT	**18. SECURITY CLASSIFICATION OF THIS PAGE**	**19. SECURITY CLASSIFICATION OF ABSTRACT**	**20. LIMITATION OF ABSTRACT**
Unclassified	Unclassified	Unclassified	UU

NSN 7540-01-280-5500

Standard Form 298 (Rev. 2-89)
Prescribed by ANSI Std. 239-18

THIS PAGE INTENTIONALLY LEFT BLANK

Approved for public release. Distribution is unlimited.

FORWARD ERROR CORRECTION ENCODING ON THE MULTIPLE INPUT/MULTIPLE OUTPUT FREE SPACE OPTICAL COMMUNICATIONS CHANNEL

Paul C. Keeley
Major, United States Marine Corps
BS, The Citadel, 2007

Submitted in partial fulfillment of the
requirements for the degrees of

MASTER OF SCIENCE IN INFORMATION WARFARE SYSTEMS ENGINEERING

and

MASTER OF SCIENCE IN APPLIED MATHEMATICS

from the

NAVAL POSTGRADUATE SCHOOL
June 2019

Approved by: Raymond R. Buettner Jr.
Advisor

David R. Canright
Co-Advisor

Peter R. Ateshian
Second Reader

Dan C. Boger
Chair, Department of Information Sciences

Wei Kang
Chair, Department of Applied Mathematics

THIS PAGE INTENTIONALLY LEFT BLANK

ABSTRACT

As a high bandwidth, narrow beamwidth channel, free space optical (FSO) communications can potentially achieve high data rates with a low probability of detection and intercept. However, in addition to the additive white Gaussian noise typical of radio frequency communications, atmospheric turbulence adds random, relatively long duration fades to the channel, which significantly decrease overall throughput. This thesis explores how various forward error correction (FEC) techniques affect the channel capacity of a multiple input/multiple output (MIMO) system. A statistical model of the channel is developed from the existing literature. Thirteen coding and modulation schemes are implemented in software and tested against this channel model under different simulated levels of noise and turbulence. Codes are compared by characteristics such as energy per bit and outage thresholds to determine which characteristics of the different codes most critically affect performance. Key performance indicators for each code include average bit error rate, overall throughput, and variability. A recommendation is made to implement variable-level coding in future advanced technology demonstrators or prototypes developed for the FSO MIMO system.

THIS PAGE INTENTIONALLY LEFT BLANK

TABLE OF CONTENTS

LIST OF FIGURES

LIST OF TABLES

THIS PAGE INTENTIONALLY LEFT BLANK

LIST OF ACRONYMS AND ABBREVIATIONS

2D	two-dimensional
AWGN	additive white Gaussian noise
BEC	binary erasure channel
BER	bit error rate
BPPM	binary pulse position modulation
BSC	binary symmetric channel
COBRA	color barcode streaming for smartphone systems
CSI	channel state information
DoD	Department of Defense
FEC	forward error correction
FPGA	field programmable gate array
FSO	free space optical
LDPC	low-density parity check
LED	light-emitting diode
MIMO	multiple input, multiple output
ML	maximum likelihood
OOC	optical orthogonal codes
OOK	on-off keying
PPM	pulse-position modulation
QR	quick response
RSC	recursive systematic convolutional
RF	radio frequency
ROI	region of interest
RZ	return to zero
SISO	single input, single output
SI/SO	soft input/soft output
SNR	signal to noise ratio
TALON	Tactical Line-of-Sight Optical Network

THIS PAGE INTENTIONALLY LEFT BLANK

I. THE FSO COMMUNICATIONS CHALLENGE

A. BACKGROUND

Threat actors throughout the world have developed sophisticated electronic warfare techniques which can be used to jam or target friendly radio-frequency (RF) emissions. However, the strength of the highly networked Joint Force to apply lethality at the lowest level requires the ability to communicate data from the tactical edge. Therefore, the Joint Force needs to develop options for tactical communications in a RF-denied environment. One option to augment existing communications systems is the use of free space optical (FSO) communications. As a high bandwidth, narrow beamwidth channel, FSO communications can potentially achieve high data rates with a low probability of detection and intercept. Single input, single output (SISO) systems such as the Tactical Line-of-Sight Optical Network (TALON) are currently being pursued by the Department of Defense (DoD). However, SISO systems are susceptible to line of sight limitations and high levels of atmospheric loss. Multiple input, multiple output (MIMO) optical systems have the potential to overcome these limitations by providing spatial diversity and redundancy to the transmission. This thesis explores ways to take advantage of this diversity and redundancy to efficiently and effectively encode transmissions.

Use cases envisioned include communications between dispersed tactical units such as reconnaissance elements, firing units or scout observers. Ranges could vary from less than 500 m (as in a dispersed artillery battery), to 10 or more kilometers as might be experienced by elements conducting expeditionary advanced base operations. Additionally, FSO systems could be used to provide a short-term, high-rate datalink capacity between surface units and unmanned or manned aerial relays.

B. PROBLEM STATEMENT

In addition to the additive white Gaussian noise (AWGN) typical of RF communications, atmospheric turbulence adds random, relatively long duration fades to the terrestrial optical channel which significantly decrease overall throughput. Conventional error correction methods applied to the data stream would require a

tremendous amount of memory to compensate for these fades. A MIMO system using arrays of parallel emitters can potentially mitigate the effects of these perturbations by applying error correction across the parallel streams of data. Recent thesis work at the Naval Postgraduate School developed a MIMO link-layer protocol using quick response (QR) codes for FSO communications channel encoding. However, this protocol did not include temporal forward error correction (FEC) and was not tested using a noisy channel model. Decoding errors that were experienced even under noiseless testing propagated forwards and backwards on the transmitted stream. An improved encoding method is needed for this channel to be feasible. This thesis formulates and tests several improved channel encoding schemes for the MIMO FSO communications channel using both temporal and spatial dimensions to correct for errors.

C. PURPOSE STATEMENT

The goal is to enable the development of a feasible MIMO FSO communications system with tactical application to the problem of effective command and control in an RF-denied, degraded or exploited environment. This will provide a key capability identified in multiple concept documents including the Department of the Navy's *Cooperative Strategy for 21st Century Seapower*, the *Marine Operating Concept*, *Littoral Operations in a Contested Environment*, and the *Marine Corps Concept for Command and Control*. This research could also be valuable to the commercial telecommunications sector and additionally has potential applicability to machine-to-machine communications and non-line of sight communications.

D. OBJECTIVE

The objective is to determine an improved atmospheric channel encoding method considering both temporal and spatial dimensions to correct for errors. Achieving this objective will improve overall reliability and throughput for various MIMO array sizes using the FSO communications channel.

E. RESEARCH QUESTIONS

Principal question: How might FEC encoding techniques be applied to improve the reliability and efficiency of the MIMO FSO communications channel?

Secondary question: How reliable/efficient is the current, unmodified QR scheme?

Secondary question: Are there other options for spatial encoding that provide similar or higher reliability/efficiency rates?

Secondary question: How do such spatial or temporal encoding schemes affect overall throughput on a MIMO FSO communications system?

F. RESEARCH METHOD

This thesis develops and implements several encoding/decoding algorithms in software as part of a basic physical layer for the proposed MIMO FSO communications system. These algorithms are tested with a channel simulator exhibiting statistical characteristics typical of the atmospheric FSO communications channel. This simulator adds simulated random noise to the stream of transmitted two-dimensional (2D) symbols, and also produces the effects of random fades.

To realistically simulate these effects, a model is developed drawing on the large body of existing work in the field. Using a pseudo-random stream of binary data as input for each test run, instead of transmitting and receiving data through an atmospheric channel, binary write/read operations are performed and errors are introduced according to the error rates described by the model.

The problems of pointing, acquisition and tracking are not addressed in this thesis. Neither are methods for overcoming atmospheric attenuation in the channel.

G. DATA, OBSERVATION AND ANALYSIS METHOD

A quantitative analysis of performance between the various encoding/decoding methods is conducted during the testing phase of this thesis. Performance is measured using achieved bit error rates for each encoding/decoding technique as determined by the successful reconstruction of the input stream in the receiver. A second metric is the coding

efficiency of each method. This performance data is measured across multiple levels of turbulence and noise and is compared to the predicted performance of the channel with no FEC applied.

H. POTENTIAL BENEFITS, LIMITATIONS AND RECOMMENDATIONS

The primary benefit of this study is an improved encoding scheme. A secondary benefit is the improvement of existing prototypical technology demonstrators, specifically by developing a working physical layer and applying forward error correction methods within the layer. Limitations include the testing method (simulation), which may introduce sources of error not found in the final implementation and which may ignore other sources of error unique to the final implementation. Recommendations as to the feasibility of the tactical application of the MIMO FSO communications channel will result from this study.

II. LITERATURE REVIEW

A. FSO COMMUNICATIONS CHANNEL

Kaushal and Kaddoum (2015) identify absorption, scattering and atmospheric turbulence as three primary factors affecting FSO communications in the terrestrial setting. Absorption and scattering may be classified as atmospheric attenuation, whereas atmospheric turbulence leads to channel fading. An extensive treatment of atmospheric turbulence may be found in Majumdar's Advanced Free Space Optics (2015), which identifies beam scintillation (measured by irradiance), beam steering, image dancing, beam spread, and spatial coherence degradation among other deteriorations of the laser beam due to atmospheric effects. In addition to the attenuation and fading due to these atmospheric effects, Khatoon, Cowley and Letzepis (2011) discuss more traditional noise effects on the channel which include additive Gaussian noise due to background radiation, shot noise from the detection process, and thermal noise from the receiver. External to the receiver, they identify sources of noise to include ambient radiation from the sun or other light-producing bodies.

A mathematical model incorporating the effects of noise and fading is developed by Al-Habash, Andrews and Phillips (2001), and is treated at greater length by Andrews and Phillips in *Laser Propagation Through Random Media* (2005). These developments propose the gamma-gamma distribution to model atmospheric fading due to turbulence. Other proposed models are surveyed by Jolly and Parikh (2011) and include the lognormal and negative exponential distributions; however, the gamma-gamma distribution is identified as the most widely applicable to a range of turbulence conditions. A relatively complete model, which provides a convenient form for geometric loss and applies the gamma-gamma distribution for irradiance to a binary pulse position modulation (PPM) scheme, may be found in Chatzidiamantis, Karagiannidis, Kriezis, Michalopoulos, and Schober (2013).

The International Telecommunications Union Radiocommunication Sector (ITU-R) (2007) provides a variety of representative parameters that may be used when modeling

the attenuation, scattering and fading properties of the atmospheric channel. Work sponsored by the Naval Research and Army Research Laboratories provides additional empirical data relating to these parameters, particularly in how the Rytov variance (a measure of irradiance or scintillation) is strongly related to levels of solar irradiance and wind speed (Bucaille, Davidson & Ricklin, 2004; Eaton, Gilbreath, Oh, Ricklin & Vallestero, 2004).

Chan (2006) provides a different model for evaluating the reliability of optical communications by considering the probability of outage and modeling the system as a finite state machine, rather than simply considering the overall (stationary) bit-error rate (BER). However, his turbulence model is based on previous work (Chan and Lee, 2004) using the less relevant lognormal distribution rather than the gamma-gamma distribution.

Kaushal and Kaddoum (2015) discuss various mitigation techniques including spatial and temporal diversity and aperture averaging, as well as various encoding techniques. Spatial diversity and aperture averaging increase the number of transmitters, receivers or both, resulting in more overall power collected on the receiver side. Spatial diversity alone may be considered as a repetition scheme. Temporal diversity refers to transmitting the same signal multiple times; by itself, it is also a repetition scheme. Advanced FEC techniques will be covered in a later section. Chan (2006) focuses on the performance gains provided by spatial diversity using PPM and other modulation techniques. While he includes temporal scrambling or interleaving as a mitigation technique, his discussion does not include more sophisticated forms of either spatial or temporal error correction. Alouini, Yang and Gao (2014) propose a different type of diversity scheme where a single transmitter with multiple apertures collects and analyzes channel state information (CSI) and uses this to select the best user among a diverse collection of single-aperture receivers; this scheme is applicable to multi-user scheduling gain but not to our single data-stream application. Akella, Yuksel and Kalyanaraman (2007) examine a multi-channel FSO design which employs optical orthogonal codes (OOC) to overcome the beam divergence problem. However, their analysis is confined to instantaneous error rates and does not account for temporal FEC techniques.

B. CHANNEL CAPACITY ESTIMATION

Claude Shannon's seminal work on the mathematics of communications (1949) defined the capacity of a communications channel in what is popularly known as the Shannon limit. Anguita, Djordjevic, Neifeld and Vasic (2005) analyze the effects of temporal error-correction codes on achieved Shannon capacity of optical atmospheric channels experiencing turbulence; however, the modulation scheme they consider is asymmetric on-off keying (OOK) which significantly changes the statistical characteristics and information-carrying capacity of the channel from a symmetric scheme such as binary PPM. Fafalios, Karagianni, Nistazakis, Tombras and Tsigopoulos (2009) develop a closed-form expression for the average capacity of symmetric SISO optical wireless channel employing PPM in the presence of atmospheric turbulence, modeled using the gamma-gamma distribution. This development is applicable since it may be directly extended to the parallel or MIMO channel considered in this thesis.

C. FORWARD ERROR CORRECTING CODES

Classic FEC codes include algebraic codes such as Hamming, Golay, Nordstrom-Robinson, Reed-Muller and Reed-Solomon codes. All of these codes involve the introduction of redundant data which allows the received code to be correctly decoded despite some level of errors or loss in the transmission over a noisy channel (Roman, 1997). Chapter III provides detailed explanations of the particular code variations used during the testing phase. Further discussion may be found in Hamming (1950), Golay (1949), Nordstrom and Robinson (1967), Preparata (1968), Reed (1954), Muller (1954), and Reed and Solomon (1960). Of note, Kudekar, Kumar, Mondelli, Pfister, Sasoglu and Urbank (2017) prove that Reed-Muller codes achieve capacity on erasure channels, which refer to communication channels in which signals can be lost as well as corrupted by noise.

Maximum likelihood (ML) decoding (the process of determining which codeword was most likely to have been sent given a series of symbols received) may be classified as hard or soft, depending on whether input or output values are rendered simply as binary decisions or as decisions with reliability estimations attached. These reliability estimations may be used by the decoding algorithm or downstream processes to improve performance

(Berrou, 2010). Furthermore, as described by Saptharishi, Shpilka, and Volk (2016), error correcting codes have different levels of performance depending on whether the setting is in context of worst case errors (the Hamming or adversarial model, see Hamming (1950)) or random errors, as in Shannon's model (1949). In a worst case setting, given a minimum distance d between codewords, one can guarantee correct decoding from at most $(d-1)/2$ errors or $d-1$ erasures. In the random case, an optimal code is one which can recover from a fraction of random errors with an arbitrarily high probability (which trades off with coding rate, or efficiency). Saptharishi et al. develop an efficient decoding algorithm for decoding first-order Reed-Muller codes with high probability of success in the random case. Vardy (1993) presents both hard- and soft-decision decoding algorithms for the Nordstrom-Robinson code. Ashikhmin and Litsyn (1996) provide a number of efficient ML decoding algorithms for Reed-Muller and Nordstrom-Robinson codes, for both the hard and soft decoding cases.

List decoding is an approach which uses the Hamming model yet provides correction capability beyond the guaranteed maximum bound. It may be applied to both hard and soft decoding. This method returns a list of likely codewords instead of the single most likely codeword (Saptharishi et al.). Ashikhmin and Litsyn provide an algorithm for list decoding first order Reed-Muller codes. Carrasco and Johnston provide an extensive treatment of the Guruswami-Sudan algorithm for list decoding of Reed-Solomon codes.

As Berrou (2010) writes, attempts to improve on the algebraic codes led to the introduction of convolutional and concatenated codes in the 1950s and 1960s. Convolutional codes perform operations on message bits to add redundant data to the temporal message stream. One important family of convolutional codes are the recursive systematic convolutional (RSC) codes, which feed outputs of each convolution back into the process. Concatenated codes combine the operations of less complex codes in series or in parallel to provide a more complex level of error correction (Berrou).

Turbo codes, which were developed in the early 1990s, apply techniques from both families of codes and were the first realization in practice of an encoding scheme which approached the Shannon limit. This achievement spurred the rediscovery of low-density

parity check (LDPC) codes which offer similar levels of error correction performance (Kienle, 2014).

D. APPLICATION OF FEC TECHNIQUES TO FSO COMMUNICATIONS

Kaushal and Khadoum (2015) identify that the memory requirement to naively implement traditional forward error control (FEC) schemes on the temporal data stream leads to impractically complex receiver designs. They survey several combinations of turbo, LDPC and Reed-Solomon codes with modulation schemes such as PPM and OOK.

Davidson and Koh (1988) examine the application of a convolutional code to a turbulent optical channel. They determine that this application provides a decrease in BER although significant interleaving depths would be required to combat the effects of the relatively long fades. Another examination of coding gain provided by convolutional coding is found in Cheng, Holzman and Yang (2013). This study provides analytical expressions for BER bounds. However, they use an asymmetric, OOK modulation scheme and a K distribution for the irradiance variable, not the gamma-gamma distribution, and their results are thus only applicable to strong turbulence conditions. Bourennane, Caussé, Khalighi and Xu (2008) examine the application of convolutional, Reed-Solomon, concatenated convolutional and Reed-Solomon, and turbo-codes in the temporal dimension to an OOK FSO system. They conclude that convolutional codes are best used when expecting weak turbulence and turbo-codes were best for strong turbulence. However, they also used an asymmetric modulation scheme (OOK).

Javornik, Jelovcan, Koudelka, Leitgeb and Muhammed (2007) analyze the coding gain provided by applying Reed-Solomon encoding to the line-coding step for a PPM signal. Aperture diversity combined with Reed-Solomon coding was found to overcome scintillation fluctuations, however variations in other attenuating factors caused bursty errors beyond the error-correcting capability of the single-level Reed-Solomon code. Djordjevic, Neifeld and Vasic (2006) propose a multilevel coding scheme that encodes parallel streams of data from L users using LDPC codes, and then converts these streams into Q-ary PPM symbols where $Q = log_2 L$. These symbols are then transmitted using a spatially diverse array of transmitters and receivers using a repetition code, and are decoded

back into L separate data streams on the receiver end. They observed significant coding gains using various combinations of array sizes and LDPC constraints. As with Alouini et al., this is more applicable to a multiple-access scenario than our single data stream scenario, although the Q-ary PPM provides one way to obtain orthogonal optical symbols.

E. 2D CODES

The principles behind algebraic codes are applicable to two-dimensional representations of data including 2D barcodes such as QR codes. Details of the implementation of the QR code are in the International Standards Organization (ISO) standard ISO/IEC 18004:2015 (2015). Several attempts have been made in the last two decades to use 2D codes to transmit data wirelessly using an optical channel. Work at the Naval Postgraduate School has included the proposal of QR symbols as a modern digital semaphore for use between manned or unmanned ships or aircraft, as well as testing of various transmission and receiver technologies by the Consortium for Robotics and Unmanned Systems Education and Research (Richter, 2013 and Lucas, 2013). Other systems using machine readable codes may be found in Rohs (2005), Madhavapeddy, Scott, Sharp, and Upton (2005), and U.S. Patent No. 7020327B2 (2006).

Felder (2018) demonstrates that QR symbols can be used dynamically to transmit lengthy data streams using an array of LEDs and a camera. Equipment limitations prevented testing at high framerates. No temporal FEC was used, however, so single QR symbol decoding errors led to propagation of the errors across multiple symbols. Fath, Schubert and Haas (2014) describe a system using smartphone cameras and in-flight entertainment screens which employed modified QR symbols to encode the data. Their initial attempts to use conventional QR symbols (ie, with only a spatial FEC dimension) resulted in poor data and bit error rates. They achieved a significant performance improvement by using only the format of the QR symbols but encoding the data stream with a temporal FEC scheme. They did not apply a combination of temporal and spatial FEC techniques.

Other schemes to transmit data via dynamic 2D codes include PixNet and COBRA. PixNet encodes a data stream into a series of 2D liquid crystal display symbols, using a RS

block code to provide instantaneous error correction. Similar to Felder's experimental setup, a camera is used to receive the transmitted symbols which are rectified and decoded—allowing for off-axis (ie, non-line of sight) transmission. This system was tested against various levels of QR codes with varying success. However, the symbol size is 81x81 which is impractical to achieve using current laser technology since it would require a 6,561-laser array (Ahmed, Katabi, and Perli, 2010). COBRA (Color Barcode Streaming for Smartphone Systems) uses color as an additional dimension to encode a data stream into a sequence of symbols designed for display and capture using smartphone screens and cameras. No error correction is employed however, and the markedly different propagation characteristics of different wavelengths over long distances would seem to preclude an easy translation of this concept to a laser array (Hao, Xing and Zhou, 2012). Hranilovic and Kschischang (2006) introduce a pixelated wireless optical channel, using arrays of amplitude-modulated transmitters and receivers. Unfortunately, while their matched-pixel case is theoretically analogous to our MIMO concept, the modulation scheme and noise model is designed for very short ranges and their results are thus too far removed from the long-range atmospheric transmission problem considered by this thesis to be applicable.

F. CONCLUSIONS

No study has yet explored the combination of both temporal and spatial coding schemes to the MIMO FSO long-range communications channel. This thesis therefore fills a gap in determining whether—and when—such a combination of coding techniques is feasible, necessary and desirable.

THIS PAGE INTENTIONALLY LEFT BLANK

III. RESEARCH METHODOLOGY

This chapter first develops the statistical characteristics of the channel perturbed by noise and turbulence. This leads to the statement of a channel model which, with selected parameters, is used to determine bit error rates (BER) for each testing run. The implementation of the channel model for simulation is described. The foundations of algebraic coding are then developed, with a focus on the specific families of codes used in the testing phase. Specific configurations used in testing are categorized as high-, mid-, and low-rate codes over several given array sizes. This development is followed by a brief discussion of the physical layer of the TCP/IP stack, and an outline of which elements of this layer were created for the testing. Variables to be isolated during tested are identified and defined. Finally, the research hypotheses are stated.

A. STATISTICAL CHANNEL CHARACTERISTICS

This thesis closely follows the work of Al-Habash et al. (2001) and Andrews and Phillips (2005) in the development of the statistical characteristics of the atmospheric channel. The optical signal to noise ratio (OSNR) will be used. The model assumes a direct (non-coherent) detection receiver and divergent Gaussian lasers, with a plane-wave approximation at the receiver. Furthermore, it is assumed that there is enough spatial diversity to consider each laser individually.

Information is modulated onto an optical beam which passes through an atmospheric channel to a receiver. Using OOK, transmission at a fixed power level P_{tx} represents a binary 1 and no power represents a binary 0. The power received is converted into current and measured by the detector. The signal current measured is affected by several factors as seen below:

$$i_S = G_{rx} L_{geo} L_{atm} I P_{tx} \tag{3.1.1}$$

where G_{rx} is the receiver gain, L_{geo} is the geometric loss factor, L_{atm} is the atmospheric loss factor, and I is the irradiance or intensity of the optical wave. Of these factors, receiver gain, and geometric and atmospheric losses are determined by system design and

configuration or by slowly changing atmospheric conditions on a time-scale of minutes to hours. These will be considered to be constant for the purposes of the model.

Of interest instead is the behavior of the channel at intervals of milliseconds or less. At this timescale, the primary factor influencing detection is the turbulence in the channel, which directly affects irradiance, denoted *I*. Chan (2006) and Bourennane et al. (2008) consider turbulence to follow a timescale on the order of 1–100 ms. At an even shorter timescale is the modulated signal, which for simplicity is taken to be 100 MHz, yielding a bit-window T_b = 10ns. Beyond this, noise is considered to be instantaneous.

The receiver measures total current flow at the receiver denoted by $i = i_S + i_N$ where i_N is the result of noise at the detector and i_S represents the current induced by the optical signal, subject to fluctuations in intensity produced by turbulence. The detector will record a binary 1 received if *i* registers higher than some threshold value i_T, and will record a 0 otherwise. The probability of accurate detection is developed in the following sections, considering the effects of turbulence and noise separately.

1. Turbulence

Al-Habash et al. (2001) describe how atmospheric turbulence produces a fluctuation in the irradiance of the received signal quantified by the scintillation index, which is defined as

$$\sigma_I^2 = \frac{\langle I^2 \rangle}{\langle I \rangle^2} - 1, \tag{3.1.2}$$

where *I* is the irradiance or intensity of the optical wave. Under weak fluctuation regimes, the scintillation index is proportional to the Rytov variance

$$\chi^2 = 1.23 C_n^2 k^{7/6} d^{11/6}, \tag{3.1.3}$$

where C_n^2 is the refractive index structure parameter ($m^{-2/3}$), $k = 2\pi/\lambda$ is the optical wavenumber (m^{-1}), and *d* is the link distance (m). Moderate fluctuations are characterized by Rytov variances near 1, while strong turbulence regimes have Rytov variances as high as 5 or 6 (al-Habash et al.). As developed by Andrews and Phillips (2005), this irradiance

I may be considered as the product of the irradiance I_x due to large-scale disturbances or eddies and the irradiance I_y due to small-scale eddies. If I is taken to be normalized with unit mean, then the second moment of irradiance is given by Andrews and Phillips as

$$\left\langle I^2 \right\rangle = \left\langle I_x^2 \right\rangle \left\langle I_y^2 \right\rangle = (1+\sigma_{I_x}^2)(1+\sigma_{I_y}^2), \tag{3.1.4}$$

which yields an implied scintillation index of

$$\sigma_I^2 = (1+\sigma_{I_x}^2)(1+\sigma_{I_y}^2) - 1 = \sigma_{I_x}^2 + \sigma_{I_y}^2 + \sigma_{I_x}^2 \sigma_{I_y}^2 . \tag{3.1.5}$$

Keeping in mind the plane wave approximation, the model may be simplified by taking the inner scale of turbulence to be zero. Large- and small-scale variances may then be calculated from the following expressions provided by Andrews and Phillips:

$$\sigma_{I_x}^2 \cong \exp\left[\frac{0.49\chi^2}{(1+1.11\chi^{12/5})^{7/6}} \right] - 1, \tag{3.1.6}$$

$$\sigma_{I_y}^2 \cong \exp\left[\frac{0.51\chi^2}{(1+0.69\chi^{12/5})^{7/6}} \right] - 1. \tag{3.1.7}$$

The inverses of these variances are denoted as α and β respectively and represent the effective number of large- and small-scale scattering cells within the turbulent atmospheric channel (Andrews & Phillips).

To find the distribution of the irradiance fluctuations, al-Habash et al. (2001) first consider each of I_x, I_y to be gamma-distributed, with probability density functions (PDFs) described by

$$\begin{aligned} p_{I_x}(I_x) &= \frac{\alpha(\alpha I_x)^{\alpha-1}}{\Gamma(\alpha)} \exp(-\alpha I_x), \alpha > 0, I_x > 0, \\ p_{I_x}(I_x) &= \frac{\beta(\beta I_x)^{\beta-1}}{\Gamma(\beta)} \exp(-\beta I_y), \beta > 0, I_y > 0. \end{aligned} \tag{3.1.8}$$

Next, they fix I_x and write $I_y = I/I_x$ to form the conditional PDF

$$p_{I_y}(I \mid I_x) = \frac{\beta(\beta I / I_x)^{\beta-1}}{I_x \Gamma(\beta)} \exp(-\beta I / I_x), I > 0 \tag{3.1.9}$$

where I_x is the conditional mean value of I. Finally, by taking the average of this conditional PDF over the distribution of I_x, they obtain the unconditional irradiance distribution

$$p(I) = \int_0^\infty p_{I_y}(I \mid I_x)\, p_{I_x}(I_x) dI_x = \frac{2(\alpha\beta)^{(\alpha+\beta)/2}}{\Gamma(\alpha)\Gamma(\beta)} I^{(\alpha+\beta)/2-1} K_{\alpha-\beta}(2\sqrt{\alpha\beta I}), I > 0 \tag{3.1.10}$$

Here, $K_\nu(.)$ is the modified Bessel function of order ν. This distribution is known as the gamma-gamma distribution (Al-Habash et al., 2001).

Considering only irradiance, Andrews and Phillips (2005) determine the unconditional probability of an outage due to the signal current being below some threshold i_T in the following manner:

$$\Pr_{fade} = \Pr(s \le i_T) = \int_0^{i_T} p_I(s) ds, \tag{3.1.11}$$

where s is used in place of i_S for clarity. Alternatively, the probability of detection of a turbulent signal is $1 - \Pr_{fade}$. Figure 1 shows the channel in a fade (I = 0.45), where the faded signal in red is being received below the threshold value of 0.5.

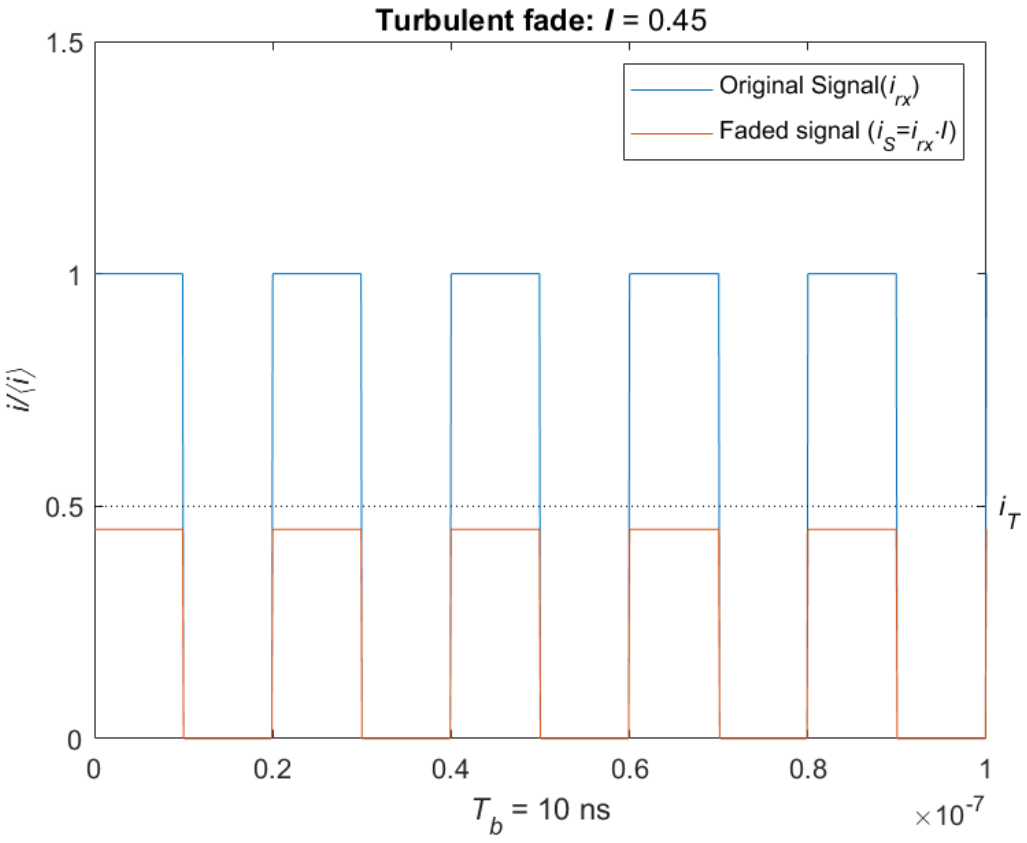

Figure 1. Square Wave Faded by Turbulence

Figure 2 shows the fluctuations in irradiance simulated on a moderately turbulent channel ($\chi^2 = 1$) with a channel coherence time of 10 ms. This figure was created using inverse transform sampling of the CDF in MATLAB. Note that the average normalized irradiance (depicted using a dotted black line) is still equal to 1. A threshold value $i_T = 0.5$ is depicted using a dashed red line. Observe that the irradiance levels fall below this threshold on 27 different occasions. Thus, using this i_T results in nearly 30% loss due to fading; this channel is unusable.

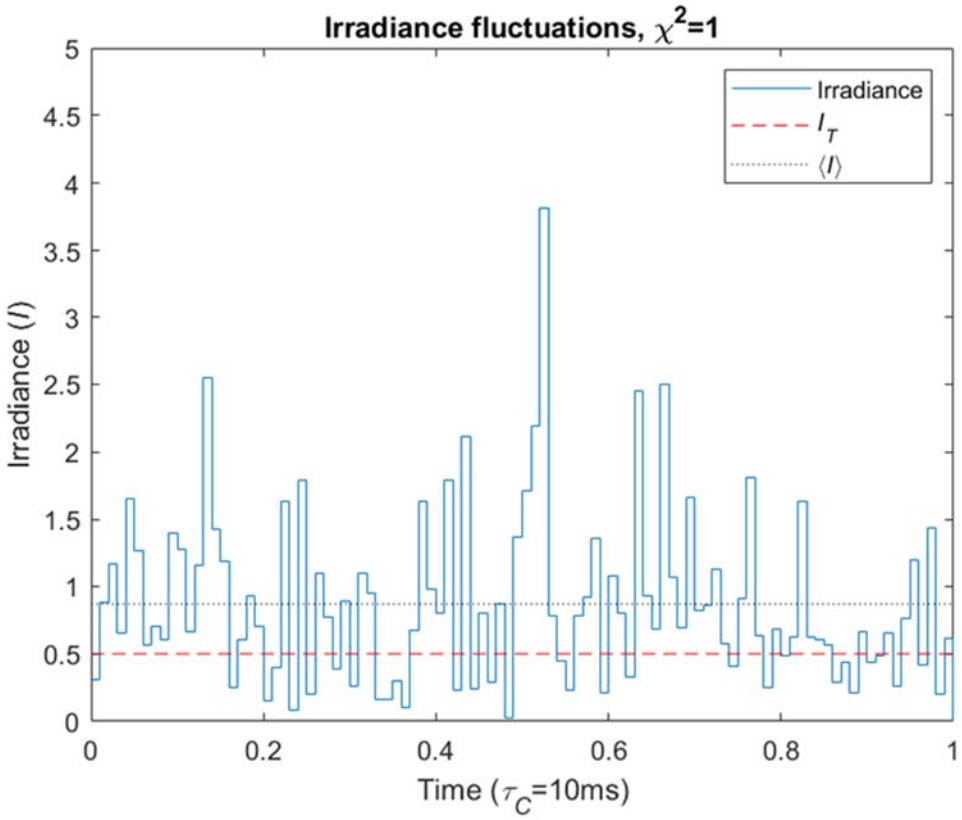

Figure 2. Simulated Irradiance Levels, Moderate Turbulence

Outage probabilities for a laser array of some size n may now be calculated given simply the Rytov variance χ^2 and a threshold i_T. Under the assumption that the spatial diversity of the lasers is greater than the coherence size of the turbulent cells, outage probabilities may be calculated independently for each laser. Thus, the probability that any k lasers are in a deep fade simultaneously (ie, due only to irradiance) is

$$\Pr(k \text{ lasers faded}) = \binom{n}{k} \left(\Pr_{fade}\right)^k \left(1-\Pr_{fade}\right)^{n-k}. \tag{3.1.12}$$

If t is taken to be some threshold value at or above which the channel is unusable, the probability that the multi-laser channel is in an outage is therefore

$$\Pr(\text{Outage}) = \sum_{i=t}^{n} \binom{n}{i} \left(\Pr_{fade}\right)^i \left(1-\Pr_{fade}\right)^{n-i}. \tag{3.1.13}$$

2. Noise

Following Andrews and Phillips (2005), to determine SNR no distinction is here made between detector shot noise due to environmental sources and the various internal sources of system noise. The Central Limit Theorem may then be invoked, allowing the total system noise to be considered additive white Gaussian noise (AWGN), with zero mean and variance $\sigma_N^2 = \frac{N_0}{2}$. N_0 is the familiar kTB_N where T = combined noise temperature and B_N = noise bandwidth. Assuming a matched filter, $B_N \approx 1/T_b$,where T_b is the duration of the bitwindow. Andrews and Phillips denote the instantaneous OSNR (hereafter SNR_0) as

$$SNR_0 = \frac{i_S}{\sigma_N}, \tag{3.1.14}$$

and provide the standard PDF for random noise

$$p_N(i) = \frac{1}{\sqrt{2\pi}\sigma_N} \exp\left(-\frac{i^2}{N_0}\right). \tag{3.1.15}$$

By integrating this PDF from some threshold value i_T to infinity, they formulate the probability of a false alarm as

$$\Pr_{FA} = \int_{i_T}^{\infty} p_N(i)di = \frac{1}{2} erfc\left(\frac{i_T}{\sqrt{2}\sigma_N}\right), \tag{3.1.16}$$

where erfc(.) is the complementary error function. Given a signal i_S, and ignoring the effects of turbulence, the output current i from the matched filter has the following Gaussian PDF with mean i_S

$$p_{S+N}(i) = \frac{1}{\sqrt{2}\sigma_N} \exp\left[-\frac{(i-i_S)^2}{2\sigma_N^2}\right]. \tag{3.1.17}$$

Similarly, the probability of detection is therefore

$$\Pr_D \text{ (noise alone)} = \int_{i_T}^{\infty} p_{S+N}(i)di = \frac{1}{2} \text{erfc}\left(\frac{i_T - i_S}{\sqrt{2}\sigma_N}\right), \tag{3.1.18}$$

with the probability of an instantaneous fade due to noise being $1-\Pr_D$ (Andrews & Phillips). Figure 3 shows a square wave at full strength but combined with AWGN at the receiver, illustrating the distortions in the wave shape at near instantaneous time-scales.

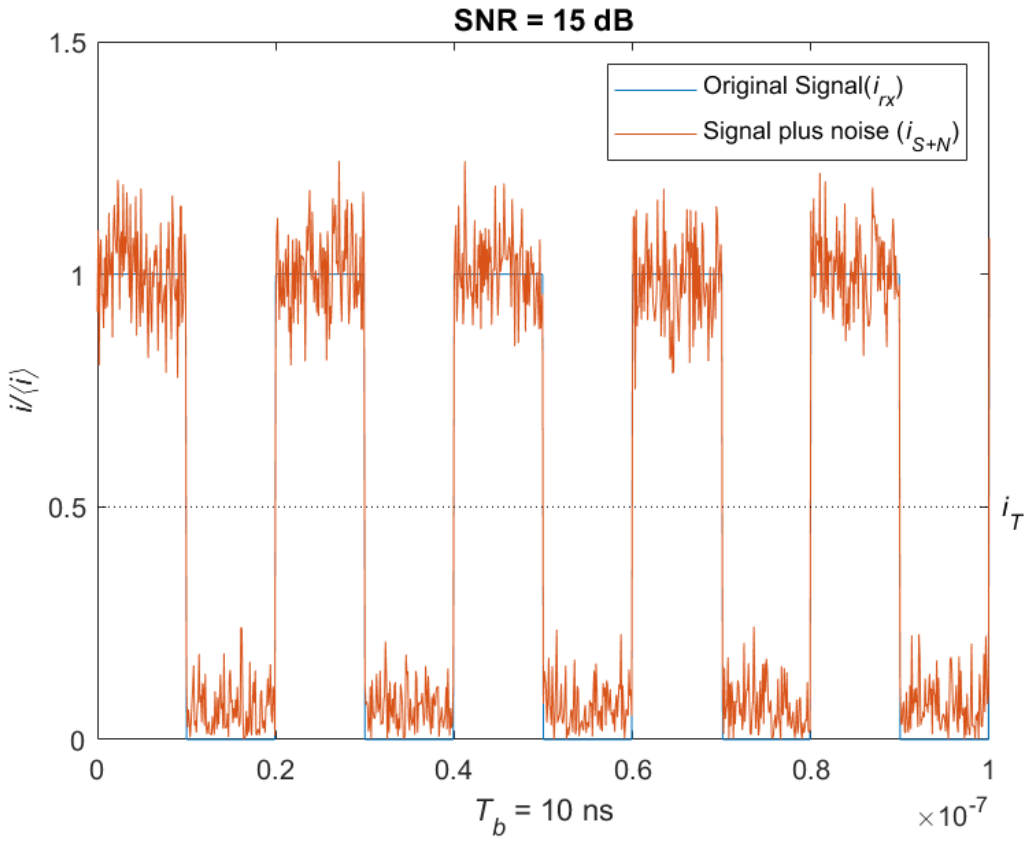

Figure 3. Square Wave Combined with Noise at the Receiver

3. Noise and Fading

The instantaneous probability of detection of a signal transmitted through a turbulent, noisy channel may now be calculated. As indicated by Andrews and Phillips (2005), this may be found by conditioning the probability of detecting the signal plus noise over the variation in the signal induced by irradiance:

$$\Pr_D = \int_0^\infty \int_{i_T}^\infty p_I(s) p_{S+N}(i \mid s) di ds = \frac{1}{2} \int_0^\infty p_I(s) \operatorname{erfc}\left(\frac{i_T - s}{\sqrt{2}\sigma_N} \right) ds. \qquad (3.1.19)$$

$\Pr_{FA}$ is not affected by turbulence and is thus as stated in equation (3.1.16). Figure 4 shows a square wave both faded by turbulence and combined with AWGN at the receiver. This is the full picture of the detection problem this thesis is trying to solve.

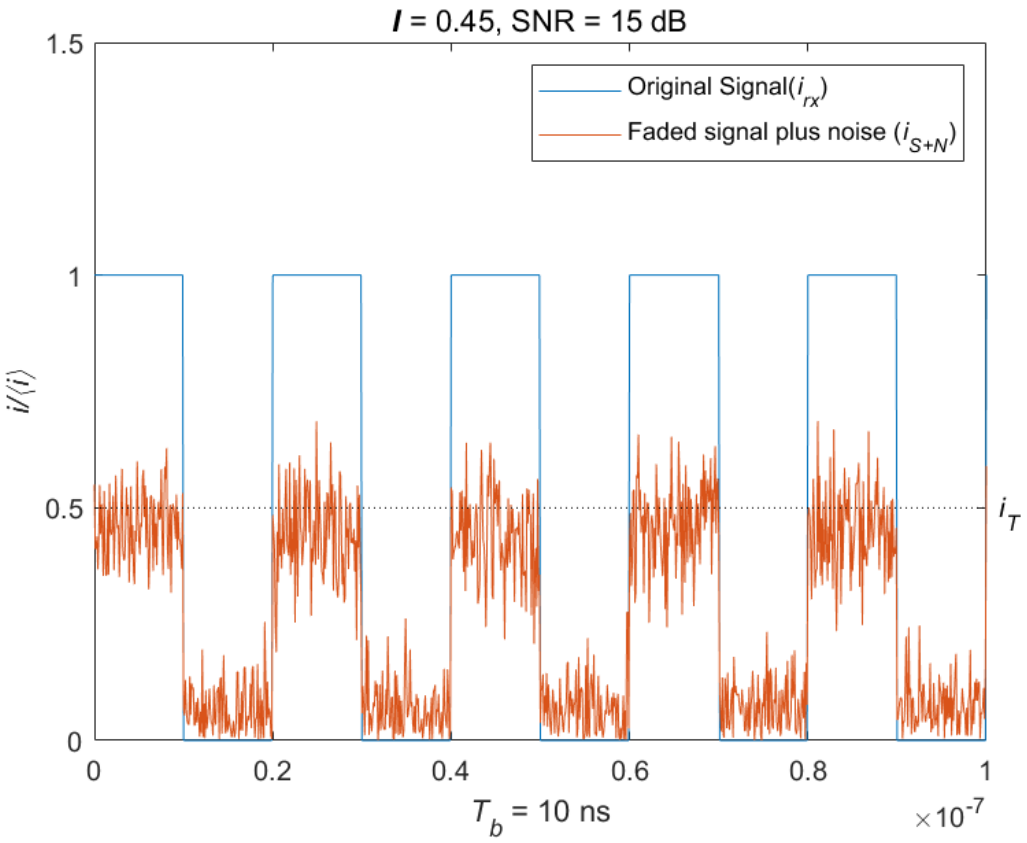

Figure 4. Faded Square Wave Combined with AWGN

B. THE CHANNEL MODEL

Using the above development, the atmospheric channel may now be modeled in the presence of turbulence and noise. Since this thesis investigates the performance of coding schemes across the spectrum of channel conditions, two techniques found within the literature will be combined. The most common technique is that provided by Andrews and

Phillips (2005) which uses the two probabilities developed above to determine the average bit error rate, or $\langle BER \rangle$. An advantage of this technique is that it may be applied to both low and high SNR regimes.

A critique leveled at this technique by Chan (2006) is that characterizing channel performance using the $\langle BER \rangle$ overestimates the channel reliability since it neglects the temporal aspect of fading on the channel, which may last between 1–100 ms. At high data rates (Gb/s per laser), this produces significant memory in the channel. He puts forward a different model which applies to the case where the SNR due to atmospheric and geometric attenuation is high, while turbulence may be low to severe. Channel capacity here primarily depends on turbulence—or, equivalently, on the probability that the channel is not in an outage due to turbulent fading.

This model combines the two approaches in a manner similar to that advanced by Bourennane et al. (2008), which treats the probability of a fade as a slowly varying channel characteristic, while noise (from all sources) is considered to vary symbol to symbol. However, this thesis does not make the assumption made by Bourennane et al. of perfect channel state information (specifically including the measurement of ambient light at the receiver), in keeping with the desire to minimize system cost and complexity. Additionally, Chan's estimate of deep fade duration (1 to 100 ms) is used to establish fading block lengths, which are significantly longer than the durations used by Bourennane et al.'s.

1. The Combined Approach

This thesis therefore uses a block-fading channel model, in which the irradiance parameter I is fixed for a series of sequential symbols. Since there is generally no correlation between turbulence strength and the length of fades (Bourennane et al., 2008) the empirical data provided by Chan (2006) is taken and block times are uniformly distributed between 1 and 100 ms. The channel is thus modeled as a series of blocks of these random lengths, with the probability that any given block is in a fade given by $\Pr_{fade}$. Based on this probability, a determination of fade/availability is made at the beginning of each block, and the result is applied to each bit-window until the end of the block.

Unfortunately, the single $\Pr_D$ of Equation 3.1.19 is not enough for the modeling purposes required—it assumes a stationary, ergodic process which will produce the correct statistics but does not accurately reflect the memory of the channel. To capture the effect of the temporal nature of the fading, the channel simulation considers the conditional probabilities of detection of a signal within noise based on whether the channel has been modeled to be in an outage or to be available. To simplify calculations, the signal received in a fade is assumed to be zero and, when available, is assumed to be full strength. Thus, the probabilities of detection given either a fade or availability are:

$$\Pr_{D|fade} = \Pr_{FA} = \int_{i_T}^{\infty} p_N(i)di = \frac{1}{2}\operatorname{erfc}\left(\frac{i_T}{\sqrt{2}\sigma_N}\right), \tag{3.1.20}$$

$$\Pr_{D|avail} = \frac{1}{2}\operatorname{erfc}\left(\frac{i_T - s}{\sqrt{2}\sigma_N}\right). \tag{3.1.21}$$

using *D|fade* to refer to detection within a fade or outage, and *D|avail* to mean detection given availability of the channel. Equivalently, the probability of a miss is described by $\Pr_{miss} = 1 - \Pr_{D|Avail}$.

Considering the transmitted symbol to be a random signal X and the received symbol to be a random signal Y, the forward channel probabilities Pr(Y was received | X was sent) are as below:

$$\begin{aligned}
&\Pr(y = 0 \mid x = 0) = 1 - \Pr_{FA}, \\
&\Pr(y = 1 \mid x = 0) = \Pr_{FA}, \\
&\Pr(y = 0 \mid x = 1) = \Pr_{fade}(1 - \Pr_{D|fade}) + (1 - \Pr_{fade})(1 - \Pr_{D|avail}), \\
&\Pr(y = 1 \mid x = 1) = (1 - \Pr_{fade})(\Pr_{D|avail}) + \Pr_{fade}\Pr_{D|fade}.
\end{aligned} \tag{3.1.22}$$

These yield the two, asymmetric forward error probabilities

$$\begin{aligned}
&\Pr_0(\text{Err}) = \Pr_{fade}(1 - \Pr_{D|fade}) + (1 - \Pr_{fade})(1 - \Pr_{D|avail}), \\
&\Pr_1(\text{Err}) = \Pr_{FA}.
\end{aligned} \tag{3.1.23}$$

Assuming a random signal, where 0 and 1 are considered to be equally likely over any lengthy transmission, the average BER is thus

$$\langle BER \rangle = \frac{1}{2}\left[\Pr_0(\text{Err}) + \Pr_1(\text{Err})\right]. \tag{3.1.24}$$

As stated before, this average rate does not fully capture the usability of the channel since it does not preserve the temporal duration of a typical fade; however it will be useful to use as a baseline for comparison with the achieved error rates using a given error correction technique.

2. Effects of Modulation on Channel Capacity

It is apparent that, using OOK, this channel is asymmetric. The probability of receiving a binary 1 in error is unchanging regardless of turbulence on the channel, while the probability of receiving a binary 0 in error depends on the irradiance. Clearly, in a high SNR regime, given any appreciable probability of fading and assuming a random signal, the value 0 will be detected more frequently than 1, leading to a decrease in entropy overall. The asymmetric OOK channel is visualized in Figure 5.

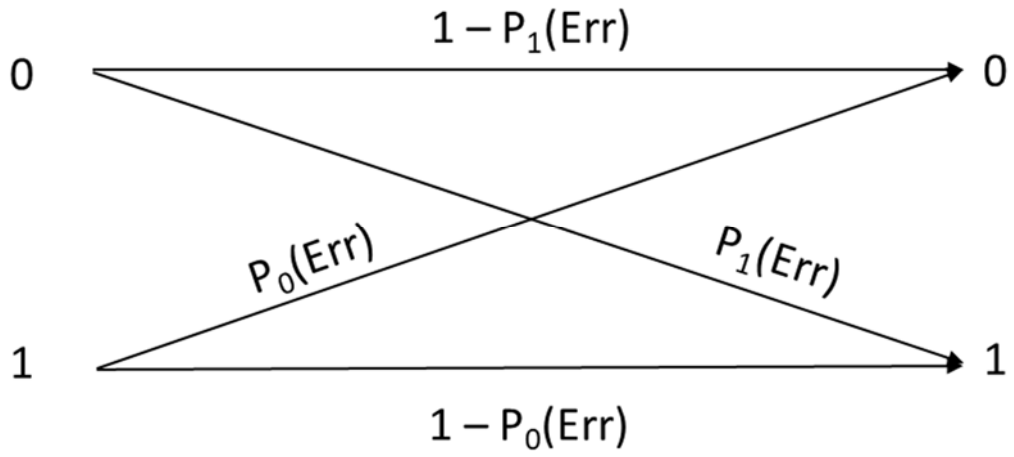

Figure 5. Asymmetric OOK Channel

Modulating the signal using binary pulse position modulation (BPPM) will overcome this asymmetry although it will decrease the bandwidth by half. BPPM transmits both an “on” and an “off” signal in some order to represent binary 0 or 1. Using this

modulation scheme, the received vector of current measurements across the bit-window is denoted $\mathbf{i}_R = [i_{S+N}, i_N]$. An erasure occurs when the vector $\mathbf{i_r} = \mathbf{I}$ or $\mathbf{0}$; that is, when the current induced by both the received signal plus noise and noise alone is above the threshold value i_T, or when both are below i_T. Either situation is ambiguous. On the other hand, an error occurs when $i_{S+N} < i_T$ and $i_N \geq i_T$ for a received symbol.

Considering the transmitted symbol as a random vector **T** and received symbol as a random vector **R**, it is desired to determine the forward channel probabilities Pr(**r** was received | **t** was sent). Let **A** = {01,10} be the subset of the binary code over two positions {00, 01, 10, 11} using the map $0 \to 01$ and $1 \to 10$. Additionally, denote an erasure by the symbol $\varepsilon \to \{00,11\}$; thus, the possible outcomes at the receiver are {0,1,ε}. Equation 3.1.19 now holds and the relevant probabilities are

$$\begin{aligned} &\Pr(\text{Correct}) = \Pr(\mathbf{r} \mid \mathbf{t} = \mathbf{r}) = \Pr_D(1 - \Pr_{FA}), \\ &\Pr(\text{Error}) = \Pr(\mathbf{r} \mid \mathbf{t} \neq \mathbf{r}, \mathbf{r} \in \mathbf{A}) = (1 - \Pr_D)\Pr_{FA}, \\ &\Pr(\text{Erasure}) = \Pr(\mathbf{r} \mid \mathbf{r} \notin \mathbf{A}) = (1 - \Pr_D)(1 - \Pr_{FA}) + \Pr_D \Pr_{FA}. \end{aligned} \tag{3.1.25}$$

This mapping allows the channel to be modeled as a binary erasure channel (with symmetric erasure and error probabilities), as depicted in Figure 6.

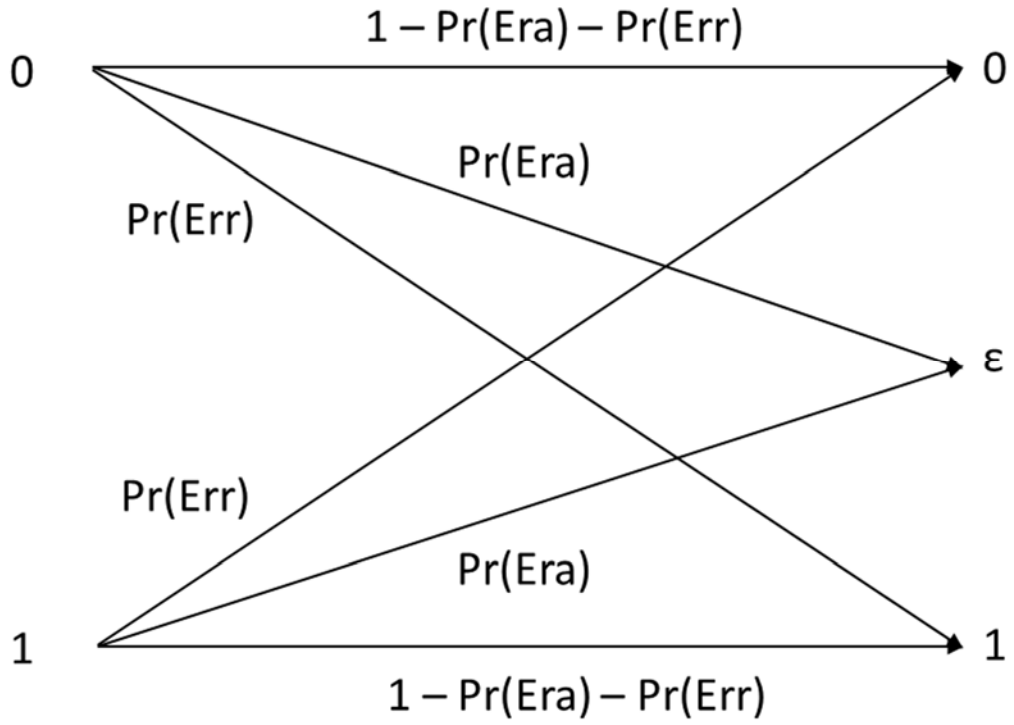

Figure 6. BPPM Binary Erasure Channel

3. The Channel Simulator

A two-step Monte Carlo approach is used for the channel simulation. Probabilities are applied to each simulated laser in turn, since by assumption there is enough spatial diversity to ensure independence. A total of *n* passes as described below are therefore performed.

First the length of the block is calculated, drawing a value uniformly from 1–100 ms. At 100 MHz, this corresponds to a block of 100,000-10,000,000 bits. The probability that the laser is in a turbulent fade during this block is then calculated, using the Pr_{fade} described by Equation 3.1.13. If so, the entire block is assessed to be in a fade and the $Pr_{D|fade}$ is applied to all binary 1s in the block. If not, the channel is assessed to be available and the $Pr_{D|avail}$ is applied to all binary 1s in the block. Either way, the Pr_{FA} is applied to all binary 0s. Figures 7 (which bears some similarity to the Markov process diagrammed by Chan (2006)) and 8 illustrate this two-step process.

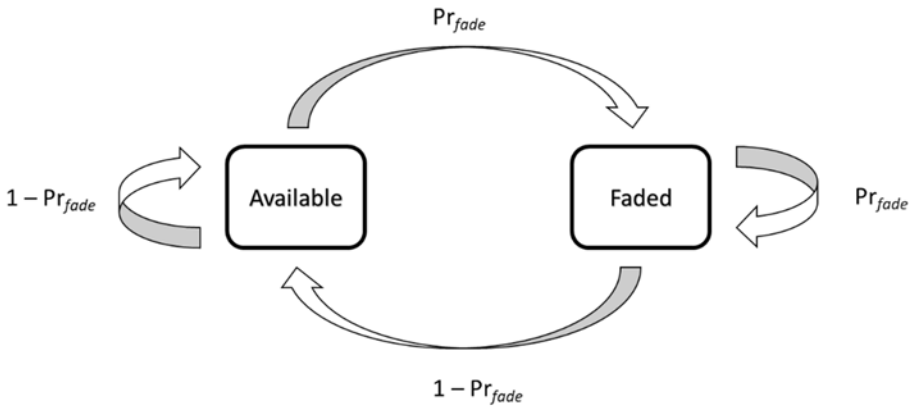

Figure 7. Channel States with Transition Probabilities

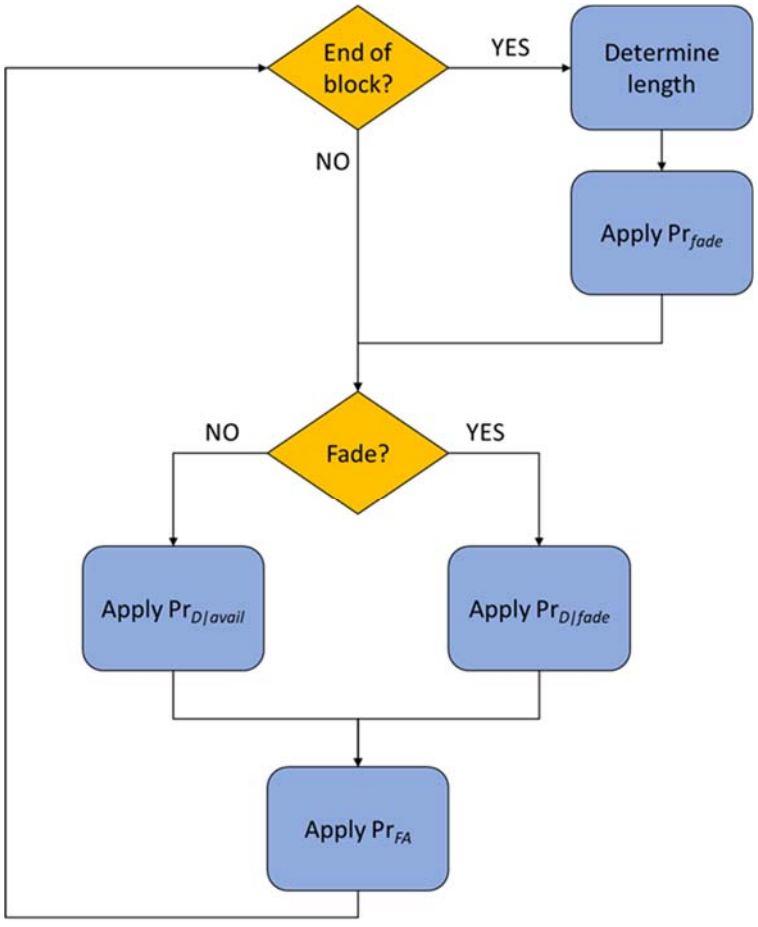

Figure 8. Channel Simulation Flowchart

Random number generation is performed using the 64-bit Mersenne Twister provided by the C++ Standard Template Libraries <random> library. Using the upper bound of the channel coherence time (100 ms), each block of 10 Msymbols is treated as a single sample, and input files are chosen of a size large enough to collect approximately 100 samples per SNR testing point.

C. CODING SCHEMES

Different combinations of well-known coding schemes may be applied to overcome the errors introduced by the atmospheric channel. These schemes are characterized by their efficiency (or coding rate) and their error correction capacity. This thesis tests a variety of codes which may be categorized as low-, mid- and high-rate, using array sizes of 8, 16, 24 and 32 lasers. Below, the basic principles of algebraic codes are developed followed by outlines of the mathematical structure behind each of the encoding schemes used.

1. Foundations

A *message* refers to a string of binary data to be transmitted over some channel. To provide error correction capability, an operation or set of operations is performed on the values in the different positions, or *coordinates*, of the message, to produce a *codeword*. These operations involve the addition of *redundant* bits, and these redundant bits are used to perform error correction. A *systematic* code is one in which each bit of the message is present in an unaltered form. A *non-systematic* code is one in which some or all of the original message bits are obscured or altered. Such a code requires an additional step of *source decoding* to recover the message after error checking and correction has occurred.

Block codes take inputs of a fixed length and map these uniquely to codewords of a different fixed length. The mapping process is known as *source encoding*. This codeword length is denoted as n, and is the first of three parameters used to classify such codes. A block code which maps inputs of length m to outputs of length n has a *code rate* of m/n, which allows us to compare the efficiency of different codes. For a given code, the *code alphabet* is the set of all possible codewords. The cardinality of this set is called the *size* of a code, and is denoted as M. This is the second defining parameter of a block code.

For a given bit-string, its *Hamming weight* is defined as the number of 1s found in the string. The *Hamming distance* between two strings is defined as the number of positions in which the strings differ. Given a code ***C***, the smallest Hamming distance between any two codewords is defined as the code's *minimum distance,* denoted *d.* This is the third important parameter, and a block code may thus be characterized as a (*n*, *M*, *d*)-code.

An important class of codes is known as *linear codes,* which establish a mapping between the *code alphabet* and the elements of a field (typically a finite field). Roman's (1997) notation and development will be followed closely throughout the following discussion of necessary linear algebraic concepts. The notation $\mathbb{F}_q^n$ is used to denote the set of strings of length *n* over a field of size *q*, where *q* is a prime power. The addition of such strings modulo *q* is defined as the component-wise addition (modulo *q*) of the coordinates of the string. Taking the elements of $\mathbb{F}_q$ as scalars, scalar multiplication may be defined as component-wise multiplication over $\mathbb{F}_q$. As Roman notes, under these two operations this set forms a vector space over $\mathbb{F}_q$. A non-empty subset *S* of $\mathbb{F}_q^n$, together with these two operations, is itself a vector space if it is closed under addition and scalar multiplication; this is referred to as a *subspace* of $\mathbb{F}_q^n$. A *generating set for S* is a nonempty set of strings $G \subseteq S$ such that every string in *S* may be expressed as a linear combination of strings in *G.* A basis of *S* is a minimal generating set for *S*. Roman notes that all bases for *S* have the same size, which is called the *dimension* of *S.* Additionally, for any basis *B* of *S*, *B* is linearly independent. A further useful operation is the inner product $\mathbf{x} \cdot \mathbf{y} = x_1 y_1 + x_2 y_2 + ... + x_n y_n$, where all operations are taken over $\mathbb{F}_q$. If $\mathbf{x} \cdot \mathbf{y} = 0$, $\mathbf{x}$ and $\mathbf{y}$ are considered *orthogonal* to each other.

Roman (1997) now defines a linear code as a code $\boldsymbol{C} \subseteq \mathbb{F}_q^n$ which is also a subspace of $\mathbb{F}_q^n$. The dimension of a linear code is denoted as *k* and is often used in place of *M* to characterize the size of a linear code, using square brackets in place of parentheses to denote an [*n, k, d*]-code. Source encoding is equivalent to matrix multiplication modulo *q* between message strings of length *k* and a given basis for ***C***. Such a basis is referred to as a *generator matrix* for ***C*** (Roman).

After transmitting the codeword across a noisy or lossy channel, the receiver detects the *senseword*, which may or may not be the codeword transmitted. *Maximum likelihood decoding* is used to determine which codeword is most likely to have been sent, given a received senseword. Using the terminology established above, it is well-known that a (*n, M, d*)-code is capable of detecting $d-1$ errors with certainty, and correcting up to $\left\lfloor \frac{d-1}{2} \right\rfloor$ errors with certainty. These limits are referred to as the hard-decision *error detection and correction capacities* of the code.

Following Roman (1997), the set of all strings orthogonal to some string $\mathbf{a} \in \mathbb{F}_q^n$ is called the orthogonal complement of **a**, or $\{\mathbf{a}\}^\perp$. This set is a subspace of $\mathbb{F}_q^n$ and is thus is a linear code. Now for some string $\mathbf{x} \in \mathbb{F}_q^n$, the inner product $\mathbf{x} \cdot \mathbf{a} = 0$ if and only if $\mathbf{x} \in \{\mathbf{a}\}^\perp$. The expanded inner product $\mathbf{x} \cdot \mathbf{a} = x_1 a_1 + x_2 a_2 + ... + x_n a_n = 0$ is referred to as a *parity check equation* for the code $\{\mathbf{a}\}^\perp$.

Considering some linear code $\boldsymbol{C} \subseteq \mathbb{F}_q^n$, the set of strings orthogonal to each string in $\boldsymbol{C}$ is referred to as the orthogonal complement of $\boldsymbol{C}$, or $\boldsymbol{C}^\perp$. This itself is a linear code, and is referred to as the *dual code* of $\boldsymbol{C}$. Any basis of $\boldsymbol{C}^\perp$ may be taken as a generator matrix for $\boldsymbol{C}^\perp$. Call such a generator matrix A. Note that for any codeword $\mathbf{c} \in \boldsymbol{C}$, any row of A may be taken as a parity check equation. Then a set of n parity check equations for $\boldsymbol{C}$ may be expressed in matrix form as simply the generator matrix of $\boldsymbol{C}^\perp$, A. By performing matrix multiplication of a senseword **x** with the transpose of this matrix, a vector **s** referred to as the *syndrome* of the senseword may be obtained:

$$\mathbf{x}A^t = \begin{bmatrix} x_1 & x_2 & \dots & x_n \end{bmatrix} \begin{pmatrix} a_{11} & a_{12} & \dots & a_{1n} \\ a_{21} & a_{22} & \dots & a_{2n} \\ \vdots & \vdots & \vdots & \vdots \\ a_{s1} & a_{s2} & \dots & a_{sn} \end{pmatrix}^t = \begin{bmatrix} s_1 & s_2 & \dots & s_n \end{bmatrix} = \mathbf{s}. \quad (3.1.26)$$

A syndrome of **0** indicates that the transmission was correct, within the error detection capacity of the code. As Roman points out, the generator matrix of a code is also the parity check matrix for the dual code. This is particularly useful for *self-dual* codes, in other words those for which $\boldsymbol{C} = \boldsymbol{C}^{\perp}$ (Roman).

As developed by MacWilliams and Sloane (2006), a linear code for which any cyclic shift of a codeword is also a codeword is termed a *cyclic* code. Thus, if $c = c_0c_1\ldots c_{n\text{-}1}$ is a codeword in some cyclic code $\boldsymbol{C}$, then $c_{n\text{-}1}c_2\ldots c_{n\text{-}2}$ is also a codeword in $\boldsymbol{C}$. Algebraically, an association may be made between a vector $c = [c_1\, c_2\, \ldots\, c_n]$ in $\mathbb{F}_q$ and a polynomial $c(x) = c_0 + c_1x + \cdots c_{n-1}x^{n-1}$, where $c_i \in \mathbb{F}_q$. Using the notation $F[x]$ to denote the set of polynomials in the variable x having coefficients from some field F, MacWilliams and Sloane consider the ring $R_n = F[x]/(x^n - 1)$, which are the residue classes of $F[x]$ modulo $x^n - 1$. Noting that multiplying by x corresponds to a cyclic shift in R_n, they define an *ideal* of R_n as a linear subspace of R_n such that if $c(x)$ is an element of the ideal, then so is $xc(x)$. In algebraic terms, then, a cyclic code $\boldsymbol{C}$ of length n may be viewed as an ideal of R_n. By multiplying some fixed polynomial $g(x)$ by every element of R_n, an ideal referred to as a *principal ideal* may be generated. The polynomial $g(x)$ is thus called the *generator polynomial* of such an ideal. MacWilliams and Sloane prove that every ideal in R_n is a principal ideal. Since every cyclic code of length n may be described as an ideal in R_n, every cyclic code therefore has a generator polynomial.

MacWilliams and Sloane (2006) define a "Hadamard matrix of order n as an $n \times n$ matrix of +1's and -1's with the property that $HH^t = nI$ " (p.44). Key to the subsequent use of these matrices is the fact that the real inner product of any row or column of a Hadamard matrix with itself is n, and with any other row is 0. MacWilliams and Sloane provide the following recursive construction for all Hadamard matrices of order 2^m, also known as Sylvester matrices:

$$H_1 = (1) \tag{3.1.27}$$

$$H_{2m} = \begin{pmatrix} H_m & H_m \\ H_m & -H_m \end{pmatrix} \tag{3.1.28}$$

A *Hadamard transform* of a row vector may be obtained by matrix multiplication with a Hadamard matrix; this is the same as taking the discrete Fourier transform of the vector (MacWilliams & Sloane, 2006). The useful properties listed above may be observed by examining a small Hadamard matrix, such as H_4 below.

$$H_4 = \begin{pmatrix} 1 & 1 & 1 & 1 \\ 1 & -1 & 1 & -1 \\ 1 & 1 & -1 & -1 \\ 1 & -1 & -1 & 1 \end{pmatrix} \tag{3.1.29}$$

Clearly, H_4 is symmetric. Every row of H_4 is orthogonal to the other rows of H_4; thus, if one takes the Hadamard transform of any given row of H_4, the result will have 0s in every position except for that corresponding to the original row, which will have a value of four. These properties hold true in the general case; thus, the Hadamard transform of the third row (or transposed column) of H_n will be $(0, 0, n, 0, \ldots, 0)$ (MacWilliams & Sloane, 2006).

A binary Hadamard matrix may be obtained by mapping (1, -1) onto $\mathbb{Z}_2$. This allows for efficient operations in software, particularly when using the Nordstrom-Robinson and Reed-Muller codes. Such a matrix, denoted as B_n, is seen below, with the mapping $1 \to 0$ and $-1 \to 1$:

$$B_4 = \begin{pmatrix} 0 & 0 & 0 & 0 \\ 0 & 1 & 0 & 1 \\ 0 & 0 & 1 & 1 \\ 0 & 1 & 1 & 0 \end{pmatrix} \tag{3.1.30}$$

Note that the Hamming distance between any two rows or columns is exactly half the order of the matrix.

For use in software, the modified Hadamard transform of a row vector may be defined by replacing the component-wise multiplication step with component-wise addition over $\mathbb{Z}_2$, followed by summing the result using ordinary addition over the non-

negative integers. In terms of bit-strings, given a string **s** of n bits, first exclusive-or (XOR) with each row of B_n, and then take the Hamming weight of the resulting n strings. When a given row of the binary matrix is transformed, the result will be a vector of non-zero values (specifically, $n/2$) except for the position corresponding to the row that was transformed, which will be zero. The same applies to the transform of the complement of a row, except that instead of zero the value corresponding to the position of the original row will be n.

2. Specific Codes Used

Four families of linear codes and one non-linear code are used in the testing phase: repetition codes, first order Reed-Muller codes, Golay codes, Reed-Solomon codes, and the Nordstrom-Robinson code. In addition to repetition codes and Reed-Solomon codes being tested alone, concatenated codes are formed using Reed-Solomon codes in combination with Reed-Muller, Golay, and Nordstrom-Robinson codes.

a. The Repetition Codes

As the name implies, a repetition code $\boldsymbol{R}_n$ maps {0,1} to {00…0, 11…1}, where each codeword is n bits long. The minimum distance d is thus equal to n. There are only two words in such a code, therefore giving it parameters (n, 2, n). Using OOK, this coding and modulation scheme has a rate of $1/n$, and can correct $\left\lfloor \frac{n-1}{2} \right\rfloor$ errors. Codes used during the testing phase of this thesis include $\boldsymbol{R}_8$, $\boldsymbol{R}_{16}$, $\boldsymbol{R}_{24}$, and $\boldsymbol{R}_{32}$.

b. First Order Reed-Muller Codes

As detailed by Roman (1997), the Reed-Muller codes are a family of binary linear codes whose parameters are such that, for any positive integer m, and all integers r where $0 \le r \le m$, the rth order Reed-Muller code $\boldsymbol{RM}(r,m)$ has parameters

$$n = 2^m, M = 2^{1+\binom{m}{1}+\ldots+\binom{m}{r}}, d = 2^{m-r} \qquad (3.1.31)$$

In the case of first order codes, these are $[2^m, m+1, 2^{m-1}]$-codes.

The code may be constructed in several ways. One construction, provided by Roman (1997), builds all of the first order $\boldsymbol{RM}(1,m)$ codes through the following inductive definition:

(1) $\boldsymbol{RM}(1,1) = \{ 00, 01, 11, 10 \}$

(2) For $m \geq 1$, $\boldsymbol{RM}(1,m+1) = \{cc \mid \forall c \in \boldsymbol{RM}(1,m)\} \cup \{cc^c \mid \forall c \in \boldsymbol{RM}(1,m)\}$,

where c^c denotes the complement of c. Another construction is provided by MacWilliams and Sloane (1977) by taking as codewords the rows of a binary Hadamard-Sylvester matrix of order 2^m, together with the complement of this matrix. For example, $\boldsymbol{RM}(1,2)$ is below and is formed by $\begin{pmatrix} B_4 \\ B_4^c \end{pmatrix}$.

$$R(1,2) = \left(\begin{array}{cccc} 0 & 0 & 0 & 0 \\ 0 & 1 & 0 & 1 \\ 0 & 0 & 1 & 1 \\ 0 & 1 & 1 & 0 \\ \hline 1 & 1 & 1 & 1 \\ 1 & 0 & 1 & 0 \\ 1 & 1 & 0 & 0 \\ 1 & 0 & 0 & 1 \end{array}\right) \tag{3.1.32}$$

All of the 1st-order Reed-Muller codes may be represented in this way. The software developed for testing source encodes by indexing each of the 2^{m+1} rows using the integer representations of m+1 bits, and then maps groups of m+1 message bits to the corresponding row.

To decode, the software computes the Hadamard transform of the received senseword. As noted above, the values of this transform (assuming no errors) will be 2^{m-1} for all positions except that corresponding to the transmitted codeword, which will be either 0 or 2^m. Without loss of generality, assume that the codeword is from the upper half of the matrix and thus will have a transform value of 0. The m bits indexing this position therefore make up the encoded message. Should a single error have occurred, then the senseword will no longer be orthogonal to any column of the binary Hadamard matrix. The Hadamard

transform will then contain an entry of 1, with some other entry being $2^{m-1} - 1$. Now if the number of errors is less than 2^{m-2}, then the scalar corresponding to the transmitted codeword will be less than any other value in the transform. If the number of errors is equal to 2^{m-2}, then the scalar corresponding to the transmitted codeword will itself be 2^{m-2}, and there will be at least one other entry with this value, making it impossible to correctly decode. Thus, the error correction capacity of this code is $2^{m-2}-1$, which is the same as $\left\lfloor \frac{d-1}{2} \right\rfloor$, as predicted by theory.

Since this code encodes $m+1$ data bits into 2^m-bit codewords, it is a $\frac{m+1}{2^m}$-rate code. To code for erasure detection, the BPPM scheme detailed in the previous section is applied. Thus, each symbol is directly followed by its complement in the transmitted stream. Considering the inductive definition provided by Roman (1997) at the beginning of this section, this maps the $m+1$ original bits into a subset of the ***RM***$(1,m+1)$ code, which has parameters $[2^{m+1}, m+2, 2^m]$. Correcting for errors in ***RM***$(1,m+1)$ is thus equivalent to correcting for erasures in ***RM***$(1,m)$ yielding the desired erasure correction capacity. However, the coding rate has been halved to $\frac{m+1}{2^{m+1}}$. To decode, the two symbols are combined at the receiver to form a 2^{m+1} senseword, and decoding is performed as described above using the left half of the binary Hadamard-Sylvester matrix $B_{2^{m+1}}$.

For the testing phase of this thesis, we use ***RM***(1,3), ***RM***(1,4), and ***RM***(1,5) corresponding to 8-, 16- and 32-laser arrays. Using BPPM, these have rates of 1/4, 5/32, and 6/64.

c. The Nordstrom-Robinson Code

Many possible constructions exist for the extended Nordstrom-Robinson ($\mathcal{NR}$) code, which is an optimum [16,8,6]-code. It is only used with the 16-laser array. For simplicity and efficient decoding, this thesis uses the construction based on ***RM***(1,4) as described by Adoul (1987). Following Berlekamp (1971), he forms the ***NR*** code by taking the union of seven cosets of weight six of ***RM***(1,4) with ***RM***(1,4). The coset leaders used

are listed below. Note that the minimum distance between any two coset leaders is six. They have been modified from Adoul's paper to express over $\mathbb{Z}_2$.

$$\begin{aligned}
c_0 &= (0\ 0\ 0\ 0\ 0\ 0\ 0\ 0\ 0\ 0\ 0\ 0\ 0\ 0\ 0\ 0)\\
c_1 &= (0\ 0\ 0\ 0\ 0\ 0\ 1\ 1\ 0\ 1\ 1\ 0\ 0\ 1\ 0\ 1)\\
c_2 &= (0\ 0\ 0\ 0\ 0\ 1\ 1\ 0\ 0\ 1\ 0\ 1\ 1\ 1\ 0\ 0)\\
c_3 &= (0\ 0\ 0\ 0\ 0\ 1\ 0\ 1\ 0\ 0\ 1\ 1\ 0\ 1\ 1\ 0)\\
c_4 &= (0\ 0\ 0\ 1\ 0\ 1\ 1\ 1\ 0\ 1\ 0\ 0\ 0\ 0\ 1\ 0)\\
c_5 &= (0\ 0\ 0\ 1\ 0\ 1\ 0\ 0\ 0\ 0\ 0\ 1\ 1\ 0\ 1\ 1)\\
c_6 &= (0\ 0\ 0\ 1\ 0\ 0\ 0\ 1\ 0\ 1\ 1\ 1\ 1\ 0\ 0\ 0)\\
c_7 &= (0\ 0\ 0\ 1\ 0\ 0\ 1\ 0\ 0\ 0\ 1\ 0\ 1\ 1\ 1\ 0)
\end{aligned} \tag{3.1.33}$$

Source encoding is done in software by taking an eight-bit message $\boldsymbol{m} = m_1m_2m_3m_4m_5m_6m_7m_8$ and splitting it into a three-bit vector and a five-bit vector: $\boldsymbol{m} = l_1l_2l_3\ r_4r_5r_6r_7r_8$. The ***l***-vector is used as a decimal value to select a coset leader indexed from the above table. The ***r***-vector is encoded into ***RM***(1,4) using the binary Hadamard-Sylvester matrix B_{16} below:

$$B_{16} = \begin{pmatrix}
0&0&0&0&0&0&0&0&0&0&0&0&0&0&0&0\\
0&1&0&1&0&1&0&1&0&1&0&1&0&1&0&1\\
0&0&1&1&0&0&1&1&0&0&1&1&0&0&1&1\\
0&1&1&0&0&1&1&0&0&1&1&0&0&1&1&0\\
0&0&0&0&1&1&1&1&0&0&0&0&1&1&1&1\\
0&1&0&1&1&0&1&0&0&1&0&1&1&0&1&0\\
0&0&1&1&1&1&0&0&0&0&1&1&1&1&0&0\\
0&1&1&0&1&0&0&1&0&1&1&0&1&0&0&1\\
0&0&0&0&0&0&0&0&1&1&1&1&1&1&1&1\\
0&1&0&1&0&1&0&1&1&0&1&0&1&0&1&0\\
0&0&1&1&0&0&1&1&1&1&0&0&1&1&0&0\\
0&1&1&0&0&1&1&0&1&0&0&1&1&0&0&1\\
0&0&0&0&1&1&1&1&1&1&1&1&0&0&0&0\\
0&1&0&1&1&0&1&0&1&0&1&0&0&1&0&1\\
0&0&1&1&1&1&0&0&1&1&0&0&0&0&1&1\\
0&1&1&0&1&0&0&1&1&0&0&1&0&1&1&0
\end{pmatrix} \tag{3.1.34},$$

selecting the row indexed by the decimal value corresponding to $\boldsymbol{r}$. For $16 \le \mathbf{r} < 32$, the complement of the row indexed by $\mathbf{r} - 16$ is chosen. The coset leader is then XOR'd with the $\mathcal{R}(1,4)$ codeword to yield the $\boldsymbol{NR}$ codeword. Finally, this is coded for erasure using BPPM as in the previous section, which means that both the codeword and its complement are transmitted one after the other. Since the $\boldsymbol{NR}$ code is a 1/2-rate code, when combined with BPPM modulation the result is 1/4-rate.

Decoding uses Hadamard transforms and follows the algorithm outlined by Adoul (1987) fairly closely. As with $\boldsymbol{RM}(1,4)$ code, decoding is performed using the left half B_{32}. For every codeword transmitted, two sensewords $\mathbf{x}$ and $\mathbf{y}$ are received. Join these together to make a 32-bit string $\boldsymbol{s} = \mathbf{xy}$. Similarly, join each of the coset leaders in 3.1.34 with its respective complement, and call these $\boldsymbol{c}_i'$. For $0 \le i < 8$, take the modified Hadamard transform (as defined in section 3.C.1, and disregarding the last sixteen values of each transform) of $\boldsymbol{s} +_2 \boldsymbol{c}_i'$, where $+_2$ denotes addition over $\mathbb{Z}_2$. Index these results as vectors of 16 elements $\boldsymbol{t}_i = (t_{i,1},\ldots t_{i,16})$. For any codeword, if no more than 2 errors have occurred, then of the 128 scalar products thus obtained (taken as entries of the vectors $\boldsymbol{t}_i$) one and only one scalar product will be in the range $14 < h_{i,j} \le 16$ (or $0 \le h_{i,j} < 2$, if the codeword is a complement of a row of B_{16}). A maximum scalar product $t_{i,j}$ so identified indicates that row $\boldsymbol{h}_j$ of B_{16} was transmitted, translated by $\boldsymbol{t}_i$. A minimum value means that row $\boldsymbol{h}_{j+16}$ was transmitted. By appending the three bits corresponding to i to the five bits corresponding to j (or $j + 16$), the message has been recovered (Adoul).

d. The Golay(24) Code

The Golay (24) code $\boldsymbol{G}_{24}$ is a [24, 12, 8]-code, which is capable of correcting up to 7 erasures. It is used with the 24-laser array. Roman (1997) defines it using the following matrix:

$$A = \begin{pmatrix} 0 & 1 & 1 & 1 & 1 & 1 & 1 & 1 & 1 & 1 & 1 & 1 \\ 1 & 1 & 1 & 0 & 1 & 1 & 1 & 0 & 0 & 0 & 1 & 0 \\ 1 & 1 & 0 & 1 & 1 & 1 & 0 & 0 & 0 & 1 & 0 & 1 \\ 1 & 0 & 1 & 1 & 1 & 0 & 0 & 0 & 1 & 0 & 1 & 1 \\ 1 & 1 & 1 & 1 & 0 & 0 & 0 & 1 & 0 & 1 & 1 & 0 \\ 1 & 1 & 1 & 0 & 0 & 0 & 1 & 0 & 1 & 1 & 0 & 1 \\ 1 & 1 & 0 & 0 & 0 & 1 & 0 & 1 & 1 & 0 & 1 & 1 \\ 1 & 0 & 0 & 0 & 1 & 0 & 1 & 1 & 0 & 1 & 1 & 1 \\ 1 & 0 & 0 & 1 & 0 & 1 & 1 & 0 & 1 & 1 & 1 & 0 \\ 1 & 0 & 1 & 0 & 1 & 1 & 0 & 1 & 1 & 1 & 0 & 0 \\ 1 & 1 & 0 & 1 & 1 & 0 & 1 & 1 & 1 & 0 & 0 & 0 \\ 1 & 0 & 1 & 1 & 0 & 1 & 1 & 1 & 0 & 0 & 0 & 1 \end{pmatrix} \tag{3.1.35}$$

The generator matrix for $\boldsymbol{G}_{24}$ is of the form $G = [I_{12} \mid A],$ where I_{12} is the identity matrix of size 12. Alternatively, one may also form the generator matrix as $[A \mid I_{12}]$. Under either construction, $\boldsymbol{G}_{24}$ is a systematic code. It is also self-dual (Roman). As implemented in this thesis, a 12-bit message $\boldsymbol{m}$ is encoded by multiplying $\boldsymbol{m}G_1$ over $\mathbb{Z}_2$. As with the two previous codes, this is then coded for erasure correction by employing BPPM, which effectively reduces the rate of the code from 1/2 to 1/4.

Using this modulation scheme, the Golay code may be decoded for mixed error and erasure corrections up to the theoretical limits. Two sensewords are detected at the receiver for each codeword transmitted. By XOR'ing these with each other, erasures may be located as defined in section 3.B.2. If no erasure is detected, only the first senseword is decoded. Otherwise, after complementing the second senseword, the general procedure is to correct and decode both sensewords. If both sensewords decode successfully, the resulting corrected codewords are compared. If they are the same, then the algorithm strips out the systematic data from the first and proceeds to the next pair of received sensewords. If not, the corrected words are compared to the sensewords in all locations not affected by erasures. The corrected word which shows the fewest changes outside of the erasures is then selected as the most likely word.

The decoding procedure follows Roman's (1997) development closely. Since $\boldsymbol{G}_{24}$ is self-dual, he uses the two generator matrices as parity check matrices. Let $G_1 = [I_{12} \mid A]$ and let $G_2 = [A \mid I_{12}]$. Let **x** be the received senseword, and assume that **e** is an error vector containing 3 or fewer errors. Using Roman's notation, consider **e = fg** where **f** and **g** are both 12 bits long. Compute both syndromes:

$$S_1 = \mathbf{e}G_1^t = [\mathbf{f} \mid \mathbf{g}]\begin{bmatrix} I_{12} \\ A \end{bmatrix} = \mathbf{f} + \mathbf{g}A, \tag{3.1.36}$$

$$S_2 = \mathbf{e}G_2^t = [\mathbf{f} \mid \mathbf{g}]\begin{bmatrix} A \\ I_{12} \end{bmatrix} = \mathbf{f}A + \mathbf{g}. \tag{3.1.37}$$

Obviously, if $S_1 = S_2 = 0$, then no errors have occurred and the systematic data may be recovered directly. Otherwise, Roman identifies three possibilities.

(1) If $w(\mathbf{f}) = 0$ and $1 \le w(\mathbf{g}) \le 3$, then $\mathbf{e} = \mathbf{0}\mathbf{g} = \mathbf{0}S_2$. Furthermore, since the sum of 3 or fewer rows of G_1 has weight at least 8, and the contribution from I_{12} is at most 3, then $w(S_1) = w(\mathbf{g}A) \ge 5$ and $w(S_2) = w(\mathbf{g}) \le 3$.

(2) Similarly, if $w(\mathbf{g}) = 0$ and $1 \le w(\mathbf{f}) \le 3$, then $\mathbf{e} = \mathbf{f}\mathbf{0} = S_1\mathbf{0}$. We observe that in this case $w(S_1) = w(\mathbf{f}) \le 3$ and $w(S_2) \ge 5$.

(3) If $w(\mathbf{f}) \ge 1$ and $w(\mathbf{g}) \ge 1$, then the weight of both syndromes will be greater than or equal to 5.

Since encoding was performed with G_1, if case 1 holds then there was no corruption of the systematic portion of the message. The information set can then be extracted directly. If case 2 holds, then $\mathbf{e} = S_1\mathbf{0}$. This vector may then be added to the senseword to compute the corrected information set.

In the final case, Roman outlines two possibilities:

(4) $w(\mathbf{f}) = 1, w(\mathbf{g}) = 1$ or 2.

(5) $w(\mathbf{f}) = 2, w(\mathbf{g}) = 1.$

In order to isolate the error strings, he then iterates through a set of up to 24 additional syndrome computations. He uses the notation $\mathbf{e}_i$ to denote a length-12 vector having a 1 in the ith position, and zeros in the remaining positions. In case 4, $\mathbf{f} = \mathbf{e}_i$ for some i. Then for $1 \le u \le 12,$ the following holds:

$$\mathbf{s}_u = (\mathbf{x} + \mathbf{e}_u \mathbf{0})G_2^t = (\mathbf{e} + \mathbf{e}_u \mathbf{0})G_2^t = (\mathbf{e}_i \mathbf{g} + \mathbf{e}_u \mathbf{0})G_2^t = \mathbf{e}_i A + \mathbf{g} + \mathbf{e}_u A \qquad (3.1.38)$$

Thus, when $u = i,\ w(\mathbf{s}_u) = w(\mathbf{g}) = 1$ or 2. For all other $u,\ w(\mathbf{s}_u) \ge 4$. Because the chosen generating matrix was G_1, the error string $\mathbf{e}_i$ thus identified can be used to correct the systematic portion of the senseword.

In case 5, $\mathbf{f} = \mathbf{e}_i + \mathbf{e}_j$ for some $i \ne j$. Then for $1 \le u \le 12$,

$$\mathbf{s}_u = (\mathbf{x} + \mathbf{e}_u \mathbf{0})G_2^t = (\mathbf{e} + \mathbf{e}_u \mathbf{0})G_2^t = ((\mathbf{e}_i + \mathbf{e}_j)\mathbf{g} + \mathbf{e}_u \mathbf{0})G_2^t = \mathbf{e}_i A + \mathbf{e}_j A + \mathbf{g} + \mathbf{e}_u A \qquad (3.1.39)$$

Now $w(\mathbf{s}_u) \ge 4$ for all u. A similar set of calculations using G_1^t must be made as seen below (which has been corrected from the 1997 Roman text):

$$\mathbf{t}_u = (\mathbf{x} + \mathbf{0}\mathbf{e}_u)G_1^t = (\mathbf{e} + \mathbf{0}\mathbf{e}_u)G_1^t = (\mathbf{f}\mathbf{e}_k + \mathbf{0}\mathbf{e}_u)G_1^t = \mathbf{f} + \mathbf{e}_k A + \mathbf{e}_u A \qquad (3.1.40)$$

If $\mathbf{g} = \mathbf{e}_k$, then when $\mathbf{u} = \mathbf{k}$, $w(\mathbf{t}_u) = 1$ or 2. Moreover, $\mathbf{t}_k = \mathbf{f}$, which again is all that is needed to correct the systematic portion of the senseword (Roman).

e. Reed-Solomon Codes

Reed-Solomon codes are especially useful for the correction of burst errors. This thesis therefore uses a Reed-Solomon code as the outer encoder for all concatenated codes to compensate for the occasional failed channel symbol (due to random noise inducing an uncorrectable error on an isolated Golay code symbol, for example). This thesis also uses Reed-Solomon codes alone at each of the array test sizes (8, 16, 24 and 32). For software

implementation, the Schifra Reed-Solomon error correcting code library is used under the guidelines of the GNU General Public License (version 2). Therefore, a summary of the characteristics of Reed-Solomon codes will be provided rather than a detailed description of coding and decoding methods.

As outlined by MacWilliams and Sloane (2006), Reed-Solomon codes are members of a particular group of cyclic codes known as BCH codes. A BCH code of designed distance D is a cyclic code over $\mathbb{F}_q^n$ if the generator polynomial $g(x)$ is the lowest degree monic polynomial over $\mathbb{F}_q$ with a string of $D-1$ consecutive powers of α as zeros, where α is a primitive n^{th} root of unity of $\mathbb{F}_q$. (As before, q is a prime power.) They prove that such a code has minimum distance $d \geq D$ and dimension $k \geq n - m(D-1)$, where m is the multiplicative order of q modulo n— in other words the smallest integer m satisfying the condition that $n \mid q^m - 1$.

MacWilliams and Sloane (2006) then define a Reed-Solomon (***RS***) code over $\mathbb{F}_q$ to be a BCH code of length $n = q - 1$. Particular properties of ***RS*** codes include the fact that the minimum distance is equal to the designed distance D, and the dimension $k = n - d + 1$. As Blahut (2003) details, to obtain a t-error correcting ***RS*** code, the designed distance D should be chosen such that $D - 1 = 2t$. Then the generator polynomial may be expressed in canonical form as

$$g(x) = (x-\alpha^b)(x-\alpha^{b+1})\cdots(x-\alpha^{b+D-2}), \tag{3.1.41}$$

where b is a non-negative integer, often taken to be 1, and α is as defined above. This generator polynomial is thus always of degree *2t.* Encoding may be either systematic or non-systematic. Additionally, Blahut proves that a Reed-Solomon code is a maximum-distance code for a given blocklength and dimension.

This thesis uses systematic Reed-Solomon codes over $\mathbb{F}_{2^8}$, which uses symbols of eight bits—a convenient size for use in digital systems. As a matter of notation, ***RS***$(n, D-1)$ over $\mathbb{F}_q$ denotes the Reed-Solomon code over $\mathbb{F}_q$ with blocklength n, and data capacity $n - D + 1$. For the purposes of the outer encoder for all concatenated codes, this thesis uses

the ***RS***(255,32) code over $\mathbb{F}_{2^8}$. This is capable of correcting up to 16 bytes in error (which could be as low as 1 bit in error in 16 different bytes, or up to all 8 bits in error in 16 total bytes). To support interoperability with inner codes whose blocklengths do not divide 8 (ie, $\boldsymbol{G}_{24}$ and the two larger Reed-Muller codes), the output may be padded several bytes of random data. Disregarding padding (which is not used for additional error correction), this code has a rate of 87%, which is multiplied by the rate of any code it is concatenated with to determine the overall coding rate.

For the high-rate encoders, four shortened variations of this primitive code over the same field are used. These include the ***RS***(64,32), ***RS***(128,32), ***RS***(120,20), and ***RS***(128,16) codes, which have been matched to the 8-, 16-, 24- and 32-laser arrays. These variations have rates 1/2, 3/4, 5/6 and 7/8. These are modulated using OOK, where each symbol of the codeword (ie, byte) is transmitted by an individual laser. The parameters are chosen such that each array can handle two lasers in a simultaneous fade, assuming a high SNR. For example, the 1/2 code is matched to the 8-laser array. Each laser will therefore transmit 8 symbols of a given 64-symbol codeword. Since the code has 32 error correction symbols, it can correct up to 16 blocks in error. Thus, even if all data from two lasers were to be lost completely, a given codeword can still be recovered.

3. QR Error Correction

In keeping with the first research question, the error correction scheme used by QR codes is now considered. The vulnerability of the code to errors in the corner detection, timing and format fields will not be considered, since these problems fall under the same category of pointing and tracking issues that are explicitly not considered by this thesis. As described by ISO (2015), each version or size of QR codes has four associated levels of error correction: Low (L), Medium (M), Quartile (Q) and High (H). This error correction is provided by a Reed-Solomon code of an appropriate size over $\mathbb{F}_{2^8}$. At the smallest size, consider the Version 1, Level H QR code, which has a codeword size of 26 bytes. Of these, 9 bytes are systematic and 17 are redundant. This corresponds to the shortened ***RS***(26,17) code over $\mathbb{F}_{2^8}$. This is capable of correcting up to 8 bytes in error, corresponding to the 30% correction capacity advertised. However, as noted above, this could be exceeded by

as few as 9 bits in error, as long as they affect separate bytes, yielding a lower bound for error correction of approximately 4%.

This variation is not specifically tested, since the QR implementation would require a laser array of 208 lasers to merely pass data, which is far beyond the current realistic configurations. (An additional 233 lasers would be needed to display a Version 1 symbol, which has $21 \times 21 = 441$ modules.) However, it is immediately apparent that the physical layout of the QR code is not optimal, since all bits of the symbol would be equally exposed to the effects of fading. This contrasts with the symbol/laser pairing described above, in which the effects of a fade are allowed to produce maximum damage to a given symbol but minimize the total surface area of the codeword exposed to fading effects. The outage probabilities may be calculated in terms of symbol error probabilities. Given an individual laser Pr_{fade}, the probability that an eight-bit symbol contains one or more faded lasers is given by Equation 3.13,

$$\mathrm{Pr}_{SymErr} = \sum_{i=1}^{8} \binom{8}{i} \left(\mathrm{Pr}_{fade}\right)^{i} \left(1 - \mathrm{Pr}_{fade}\right)^{8-i}. \tag{3.1.42}$$

The probability of outage for a QR code of size M bytes with k redundant bytes is thus

$$\Pr(\mathrm{Outage}_{QR}) = \sum_{i=\left\lfloor \frac{k}{2} \right\rfloor}^{M} \binom{M}{i} \left(\mathrm{Pr}_{SymErr}\right)^{i} \left(1 - \mathrm{Pr}_{SymErr}\right)^{M-i}. \tag{3.1.43}$$

D. PHYSICAL LAYER MODEL

The transmission control protocol/Internet protocol (TCP/IP) 5-layer model as described by Comer (2015) is used in the following discussion. Figure 9 is a diagram of this model. As application data created in Layer 5 passes down through the stack, nested headers are added by each protocol layer containing the results of computations performed to ensure that the receiving system will be able to properly reassemble and use the data. Of primary concern is the physical layer, which handles all things related to the physical transmission medium to include hardware interfaces (Comer).

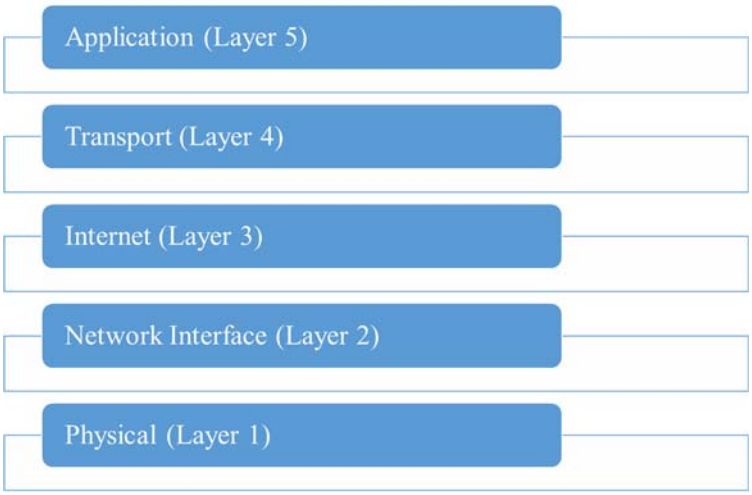

Figure 9. TCP/IP 5-Layer Model

The physical layer receives discrete blocks of data from Layer 2. Because of the nested headers, these blocks include the original application data, along with prepended headers from the transport, Internet and network interface layers. This block of data will be referred to as a datagram rather than a frame, to prevent confusion with terminology often reserved for Layer 3, as well as image-processing terminology. As Comer describes, typical actions performed on the datagram within Layer 1 include data compression, data encryption, channel coding, multiplexing or interleaving, and line coding or modulation.

A rudimentary physical layer is developed for use during the testing phase of this research, as well as for implementation (and future development) with various advanced technology demonstrators at the NPS Cebrowski Institute. All coding is done in C++11 using the GNU Compiler Collection (GCC) version 7.3.0. Of the above listed functions, the focus is on the channel coding, interleaving, and line coding steps. For the concatenated codes, spatial coding is introduced as a sub-step to line coding, breaking this step into symbol coding and modulation. Figure 10 is a schematic of the physical layer as implemented in this thesis.

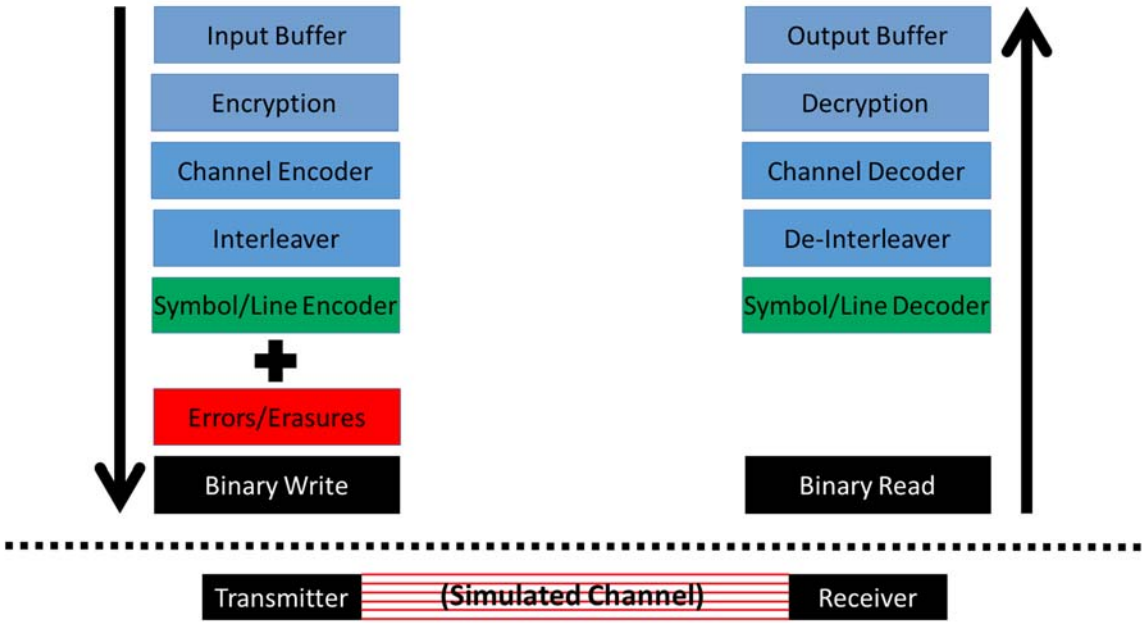

Figure 10. Physical Layer Schematic

For testing, large files filled with the output of /dev/urandom are used to simulate the transmission of upstream data. An encryption step is performed primarily to stand in for future work, since this research does not require high levels of cryptographical security. Data is XOR'd with the output of a 32-bit linear feedback shift register (LFSR) described by the primitive polynomial (modulo 2)

$$x^{32} + x^7 + x^5 + x^3 + x^2 + x + 1, \tag{3.1.44}$$

which produces a maximal length sequence of 2^{32}–1 pseudo-random bits, employing the code provided by Schneier (1996). Data-compression is not performed.

Since the testing implementation simulates the effects of the transmission channel, it does not involve actual transmitters and receivers. For transmission, the final step simply involves a binary write to a file. Likewise, reception involves a binary read from the file created in the transmission step. The atmospheric channel is simulated by an intermediate step where errors are introduced, distributed according to the probabilistic model described above.

E. EXPERIMENT DESIGN

Three primary variations of channel coding, line coding, and modulation are tested on array sizes of 8, 16, 24 and 32 lasers. For high data transmission rates with limited error correction capability, the shortened ***RS***(64,32), ***RS***(128,32), ***RS***(120,20), and ***RS***(128,16) codes are used in conjunction with OOK, yielding rates between 50–87%. For moderate data rates with increased error correction capability, a variety of algebraic inner codes concatenated with the ***RS***(255,32) outer code are tested, using BPPM. These yield overall rates ranging from 8–22%. The concatenated schemes also include byte-wise interleaving in blocks of 1MB between the outer and inner codes. For low data rates with the highest error correction capability, repetition codes of sizes 8, 16, 24 and 32 are tested using OOK, yielding rates of 3–12.5%.

While accurate decoding statistics may be captured at the ***RS*** decoder in the high- and mid-rate cases, we perform instead a byte-wise comparison of the transmitted and received files. This puts all cases on an even evaluation field, since the repetition codes are not able to detect decoding errors. Given the assumption of a random signal, achieved BER is calculated as $\frac{1}{2}\left(\frac{\text{bytes in error}}{\text{total bytes}}\right)$.

Four primary experiments are conducted to determine the effect of the following parameters on system performance: array size, coding scheme, modulation scheme, turbulence levels, SNR and i_T. A transmission rate or optical switching frequency of 100 MHz is used for all experiments. Coding performance is compared at five different levels of turbulence, and several choices of i_T are made to yield varying values of $\Pr_{fade}$. For each level of turbulence, data is collected at 10 different levels of SNR. At each SNR level, 100 data points are collected each representing the transmission of 1,000,000 symbols, which is equivalent to the 100 ms maximum τ_C.

To quantify the effects of noise on the varying levels of FEC, E_b is calculated for each coding and modulation scheme following Carlson and Crilly (2010). Considering the effects of distance and attenuation to be constant, this development will focus on the power received, not the power transmitted. For OOK, the average energy per receiver, per symbol

period may be derived in the following manner. To transmit a "1" the laser transmits at a constant power. As noted above, this induces a current of amplitude i_s on the receiver. The power received (ignoring resistance) is thus i_s^2. To determine the energy received, this power level is integrated over the symbol period:

$$E_{rcv} = \int_0^{T_s} i_s^2 dt = i_s^2 \int_0^{T_s} dt = T_s \times (i_s^2). \tag{3.1.45}$$

Since the laser does not transmit for a "0," the average power received per signal bit is

$$E_{rcv,av} = \frac{T_s}{2} \times \left(i_s^{\,2} + 0^2 \right) = \frac{T_s}{2} \times i_s^2. \tag{3.1.46}$$

E_b may be calculated as

$$E_b = \frac{1}{\text{code rate}} \times E_{rcv,ave} = \frac{1}{\text{code rate}} \times \frac{T_s}{2} \times i_s^{\,2}, \tag{3.1.47}$$

For the repetition codes, this is simply

$$E_{b,rep} = N \times \frac{T_s}{2} \times i_s^{\,2}, \tag{3.1.48}$$

where N is the size of the array. For the concatenated codes using BPPM over twice T_s, this becomes

$$E_{b,conc} = \frac{1}{(\text{outer code rate}) \times (\text{inner code rate})} \times T_s \times i_s^{\,2}. \tag{3.1.49}$$

Equation 3.1.45 yields an approximation for the Reed-Solomon codes, which assumes that the weight spectral density of the various Reed-Solomon codes used are uniformly equivalent to a random signal. Since the variants used are systematic, the systematic data is pseudo-random due to the scrambling step, and the systematic portion of the codes become proportionately larger as the array sizes increases, this approximation should be reasonable.

To quantify the effects of fading on each scheme, Pr(Outage) is calculated as described at the end of Section 3.1:

$$\Pr(\text{Outage}) = \sum_{i=t}^{N} \binom{N}{i} \left(\Pr_{fade}\right)^{i} \left(1 - \Pr_{fade}\right)^{N-i}, \tag{3.1.50}$$

where N is the size of the array and t is a threshold value. For the repetition codes, the fading threshold t is $N/2$. For the concatenated codes, t is $d/2$ where d is the minimum distance of the inner code. For the Reed-Solomon codes, t is 3 by design, as outlined in Section 3.C.3.e. These parameters are summarized in Table 1. Of note, the concatenated Reed-Muller codes have the same Pr(Outage) as the repetition codes of the same size and under the same channel conditions.

Table 1. Code Parameters

Code	$\boldsymbol{E_b / i_s^2}$	$\boldsymbol{N}$	$\boldsymbol{t}$
No FEC	0.50×10^{-8}	All	1
RS(64,32)	1.00×10^{-8}	8	3
RS(128,32)	0.67×10^{-8}	16	3
RS(120,20)	0.60×10^{-8}	24	3
RS(128,16)	0.29×10^{-8}	32	3
RM(1,3) / ***RS***(255,32)	2.30×10^{-8}	8	4
RM(1,4) / ***RS***(255,32)	3.67×10^{-8}	16	8
RM(1,5) / ***RS***(255,32)	6.12×10^{-8}	32	16
NR / ***RS***(255,32)	2.30×10^{-8}	16	6
$\boldsymbol{G}_{24}$ / ***RS***(255,32)	2.30×10^{-8}	24	8
$\boldsymbol{R}_8$	4.00×10^{-8}	8	4
$\boldsymbol{R}_{16}$	8.00×10^{-8}	16	8
$\boldsymbol{R}_{24}$	12.00×10^{-8}	24	12
$\boldsymbol{R}_{32}$	16.00×10^{-8}	32	16

For the first experiment, codes are grouped by array size and compared to determine how choices in coding and modulation schemes affect performance. While this comparison is useful to determine overall trends, the effects of the different parameters are confounding and the subsequent experiments compare specific parameters in isolation to attempt to quantify the effects of each.

The second experiment quantifies the effect of varying i_T while keeping the coding scheme and turbulence levels constant. In the third experiment, Pr(Outage) is kept constant while E_b is varied. The fourth experiment reverses this, keeping E_b constant and varying Pr(Outage).

Two additional experiments are performed with the concatenated codes. The fifth experiment compares the performance of these codes with and without the 1MB interleaver. The sixth experiment compares the concatenated codes to the inner codes alone.

To calculate error probabilities, the distributions developed in the first section of this chapter are used. Representative Rytov variances of 0.04, 0.2, 1, 5 and 25 are selected to cover weak, moderate and strong turbulence regimes. SNR are taken at 5 dB increments from 0 to 50 dB within each turbulence regime. Threshold values i_T are chosen to vary the channel probabilities. Since initial testing runs showed that a Pr_{fade} greater than 15% resulted in unusable channels, the values for Pr_{fade} run from <0.01% to 12.5% in roughly 3% increments. Table 2 summarizes the chosen parameters, while Appendix A contains a full listing of channel probabilities generated from these parameters, along with figures displaying the irradiance PDFs and CDFs. The three values marked with a star are reduced values used in Experiments 2–4.

Table 2. Simulation Testing Parameters

χ^2	i_T	Pr_{fade}
0.04	0.5	0.000675
0.2	0.25*	0.003498
0.2	0.33	0.015002
1	0.125*	0.030532
1	0.2	0.074877
5	0.0625*	0.049086
5	0.125	0.10734
25	0.125	0.12579

F. TESTING HYPOTHESES

(1) Experiment 1

Null Hypothesis: All codes (low-, mid- and high-rates) perform the same under the varied conditions, as measured by $\langle \text{BER} \rangle$.

Alternative Hypothesis: At least one code exhibits a statistically significant difference in performance from each group, under each condition.

(2) Experiment 2

Null Hypothesis: Changing i_T has no effect on code performance.

Alternative Hypothesis: Varying i_T has a statistically significant effect on code performance.

(3) Experiment 3

Null Hypothesis: Varying E_b has no effect on code performance.

Alternative Hypothesis: A change in E_b has a statistically significant effect on code performance.

(4) Experiment 4

Null Hypothesis: Varying Pr(Outage) has no effect on code performance.

Alternative Hypothesis: A change in Pr(Outage) has a statistically significant effect on code performance.

(5) Experiment 5

Null Hypothesis: Removing the interleaver from the concatenated codes does not affect achieved $\langle \text{BER} \rangle$.

Alternative Hypothesis: Presence or absence of the interleaver has a statistically significant impact on achieved $\langle \text{BER} \rangle$ for the concatenated codes.

(6) Experiment 6

Null Hypothesis: Transmission with only the inner code for the concatenated codes has no statistically significant effect on achieved $\langle \text{BER} \rangle$.

Alternative Hypothesis: Removing the outer code will significantly impact performance under all conditions.

THIS PAGE INTENTIONALLY LEFT BLANK

IV. RESULTS

Results of simulation testing are detailed below. After describing the experimental region of interest and the performance indicators, the results of Experiments 1 through 4 are analyzed, followed by an extension of this analysis to QR codes. Finally, Experiments 5 and 6 (dealing only with the concatenated codes) are analyzed. Visualizations of the raw data from each trial are found in Appendix B.

A. EXPERIMENTAL REGION OF INTEREST

Of interest is the usable range (defined in terms of SNR) for a given code at a given threshold value i_T, under certain turbulent conditions as quantified by the Rytov variance. The relevant probabilities are those defined by Equations 3.1.11, 3.1.16, 3.1.20 and 3.1.21 (Pr_{fade}, $Pr_{FA} = Pr_{D|fade}$, and Pr_{miss}). To illustrate their interplay, Figure 11 depicts the probabilities used in simulating the channel conditions for $\chi^2 = 1$, $i_T = 0.2$.

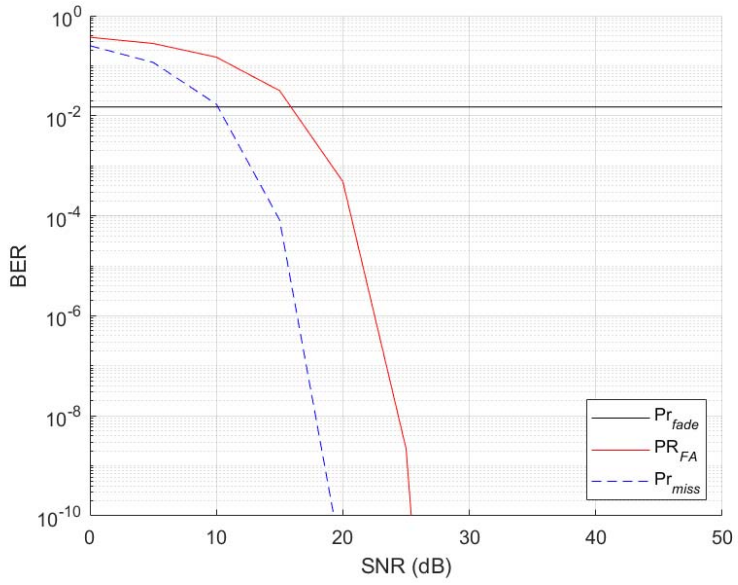

Figure 11. Channel Probabilities for Moderate Turbulence, i_T =0.2

Both the Pr_{FA} and the Pr_{miss} drop off rapidly as SNR increases, while the Pr_{fade} remains constant throughout. ($Pr_{D|fade}$ is equal to Pr_{FA}.) Clearly, once SNR is high enough (25-30 dB), channel performance is primarily due to Pr_{fade}. One may thus evaluate the relative performance of codes by how sensitive they are to the decrease in noise and by how strongly they handle fades once the channel has stabilized. Similar graphs for each set of parameters tested may be found in Appendix A.

Figure 12 shows the data resulting from applying the channel simulator to the $\boldsymbol{R}_8$ code, using the same Rytov variance of 0.2 and threshold i_T of 0.25. Each diamond represents the BER achieved during 0.1 seconds of simulated transmission at 100Mbaud, and there are 100 such data points (representing 10 seconds of transmission time) taken every 5 dB of SNR for a total of 10×10^9 symbols observed. Note that the y-axis (BER) is plotted on a broken logarithmic scale showing detail down to 10^{-9}. The solid black line represents $\langle \text{BER} \rangle$ while the dashed line shows the 95% confidence interval of the mean.

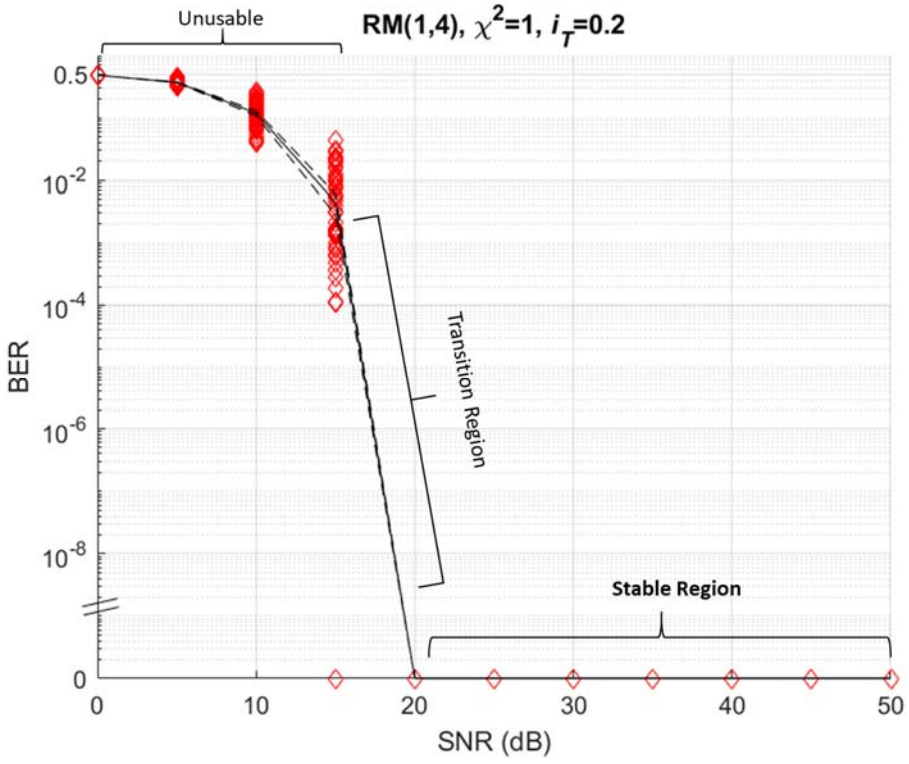

Figure 12. Representative Simulation Output

Three distinct regions are easily seen. From 0 to 15 dB the $\langle \text{BER} \rangle$ is above 10^{-3} and the channel is thus unusable. A sharp transition occurs between 15 and 20 dB. From 20–50 dB, the $\langle \text{BER} \rangle$ settles to zero with no observed variation. Referring back to Figure 10, the transition region noted above corresponds to the initial sharp decrease in Pr_{miss}, while the stable region emerges as Pr_{FA} approaches zero asymptotically between 25 and 30 dB. These three regions are found in all of the results obtained. Performance may thus be quantified by considering: 1) the $\langle \text{BER} \rangle$ obtained in the stable region; 2) the transition point defining the left bound of the stable region; and 3) the amount of variability found in the stable region.

Comparisons are made using either one-way analysis of variations (ANOVA) or a two-sample *t*-test, at 95% significance, over the widest region of interest among the codes being compared. Significant differences are bolded and starred in the charts that follow. Of note, outliers are important. Differences which may not be statistically significant in terms of mean BER (such as a single deep fade within an otherwise stable region) may be considered significant when viewed in light of the difficulties faced by TCP and other higher level protocols when handling a deep fade. Therefore, outliers were not discarded when preparing the data.

B. EXPERIMENT 1: COMPARISON OF CODES BY RATE AND ARRAY SIZE

This experiment compares codes at five different Pr_{fade}, which cover a representative range of turbulence levels marked by Rytov variances of 0.04 (extremely weak) up to 25 (saturation). Threshold values i_T are as listed in Table 2. Simulations are conducted for low-, mid- and high-rate codes for array sizes 8, 16, 24 and 32.

Figures 13–17 show results for these codes, ordered by turbulence level from low to high. Each figure contains four panels corresponding to the four array sizes, and each panel shows the achieved $\langle \text{BER} \rangle$ curves plotted corresponding to the low-, mid- and high-rate codes for the given array size. The dashed line is the "no-code" case, which is calculated from the channel statistics and represents the output of a signal with no FEC

applied. Overall, differences were found between at least two codes in every trial conducted. Thus, the null hypothesis is rejected in each case.

Performance under extremely weak turbulent conditions is typical of an AWGN channel, and is displayed in Figure 13. In the 8-laser array size, the ***RM***(1,3)-based concatenated code reaches a $\langle \text{BER} \rangle$ of 0 at an SNR point of 15 dB. The other codes achieve similar performance at 20 dB, and thus the concatenated code may be said to have a coding gain of 5 dB over the other two codes (although this difference in means was not statistically significant, since all three codes had $\langle \text{BER} \rangle < 10^{-8}$ at the 10 dB SNR point). Both the low- and mid-rate codes used at the 16-laser size show a statistically significant coding gain of at least 5 dB over the ***RS***(128,64) code. With 24 lasers, the concatenated and repetition codes achieve a 10 dB coding gain over the ***RS*** code. This is replicated with 32 lasers.

Table 3 summarizes these results. The stable regions are as defined above, and the mean BER and standard deviation are calculated across this region for each code.

Table 3. Experiment 1 Results, $\chi^2 = 0.04$, $\text{Pr}_{fade} = 0.000675$

Size	**Code**	**Stable Region**	$\bar{X}$	**SD**
	No FEC	20-50 dB	0.000337	n/a
8	***RS***(64,32)	20-50 dB	0	0
	RM(1,3)/***RS***(255,32)	15-50 dB	0	0
	$\boldsymbol{R}_8$	20-50 dB	0	0
16	***RS***(128,32)	**20-50 dB***	0	0
	RM(1,4)/***RS***(255,32)	10-50 dB	0	0
	$\boldsymbol{NR}_{16}$/***RS***(255,32)	15-50 dB	0	0
	$\boldsymbol{R}_{16}$	15-50 dB	0	0
24	***RS***(120,20)	**20-50 dB***	0	0
	$\boldsymbol{G}_{24}$/***RS***(255,32)	10-50 dB	0	0
	$\boldsymbol{R}_{24}$	10-50 dB	0	0
32	***RS***(128,16)	**20-50 dB***	0	0
	RM(1,5)/***RS***(255,32)	10-50 dB	0	0
	$\boldsymbol{R}_{32}$	10-50 dB	0	0

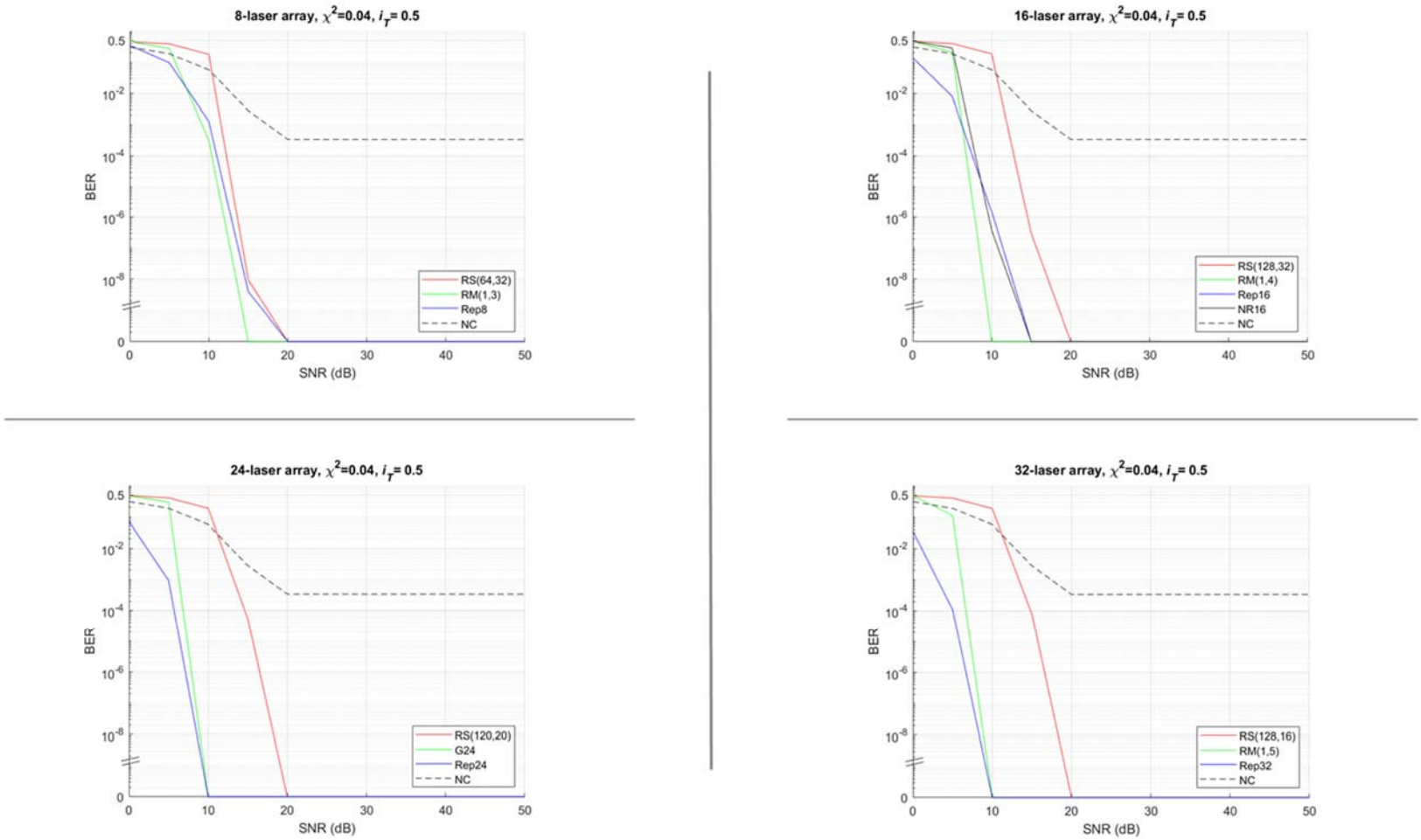

Figure 13. Experiment 1 $\langle \text{BER} \rangle$ Curves, Extremely Weak Turbulence, Pr_{fade} = 0.000675

Under weak turbulent conditions with a Pr_{fade} = 0.015, the high-rate codes fail to achieve satisfactory performance at all sizes, with unstable $\langle BER \rangle$ in the 10^{-4} to 10^{-5} range. The low- and mid-rate codes perform well in the stable region, and in all cases anticipate the drop in Pr_{FA} by 5 or more dB. Table 4 and Figure 14 contain these results.

Table 4. Experiment 1 Results, $\chi^2 = 0.2$, Pr_{fade} = 0.015002

Size	**Code**	**Stable Region**	$\bar{X}$	**SD**
	No FEC	25-50 dB	0.007501	n/a
8	***RS***(64,32)	25-50 dB	6.0271×10^{-5}	1.4763×10^{-3}
	RM(1,3)/***RS***(255,32)	20-50 dB	0	0
	$\boldsymbol{R}_8$	20-50 dB	0	0
16	***RS***(128,32)	**25-50 dB***	9.3959×10^{-5}	1.1078×10^{-3}
	RM(1,4)/***RS***(255,32)	15-50 dB	0	0
	$\boldsymbol{NR}_{16}$/***RS***(255,32)	15-50 dB	0	0
	$\boldsymbol{R}_{16}$	20-50 dB	0	0
24	***RS***(120,20)	**25-50 dB***	2.1300×10^{-4}	1.4143×10^{-3}
	$\boldsymbol{G}_{24}$/***RS***(255,32)	15-50 dB	0	0
	$\boldsymbol{R}_{24}$	15-50 dB	0	0
32	***RS***(128,16)	**20-50 dB***	4.1186×10^{-4}	2.1842×10^{-3}
	RM(1,5)/***RS***(255,32)	10-50 dB	0	0
	$\boldsymbol{R}_{32}$	15-50 dB	0	0

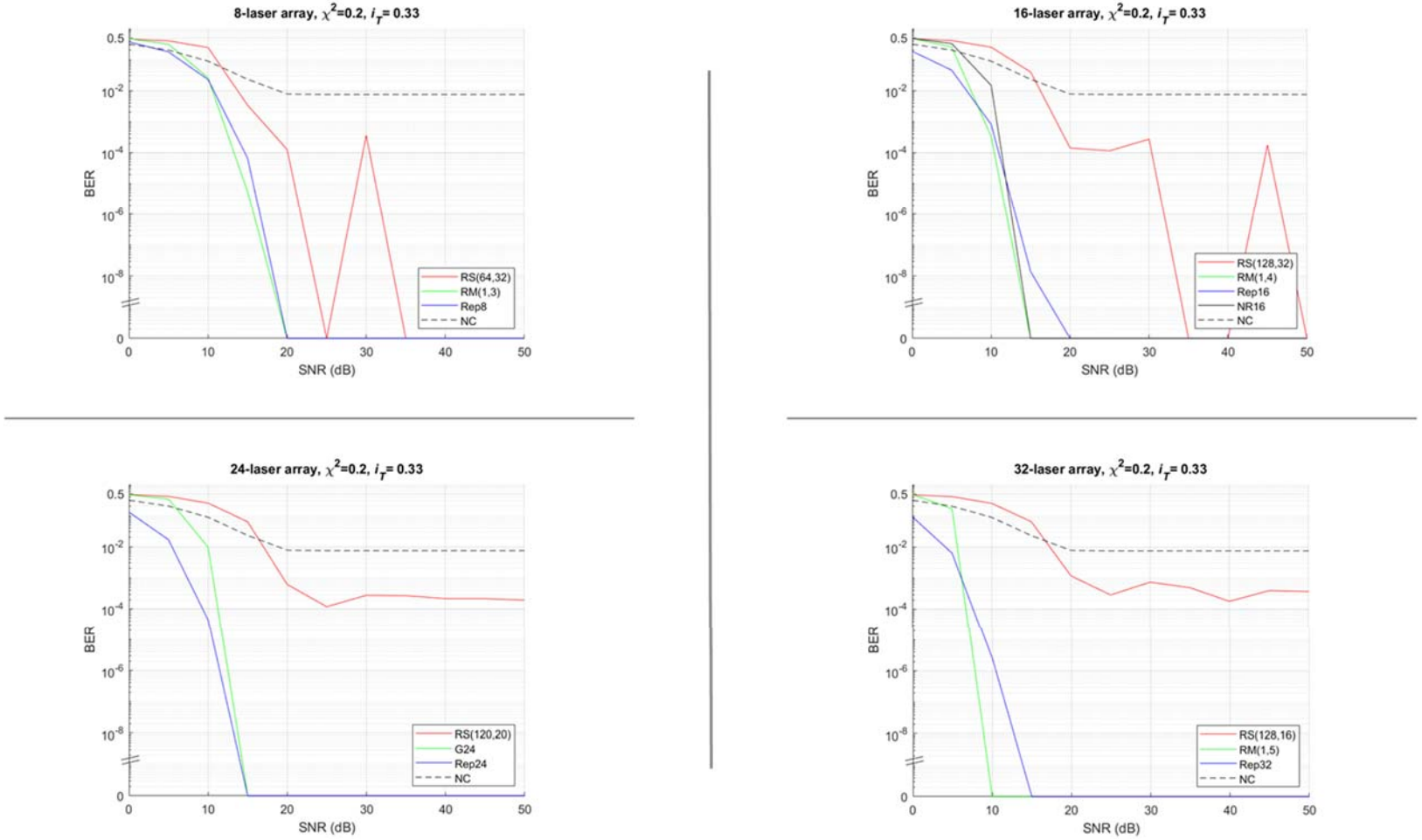

Figure 14. Experiment 1 $\langle \text{BER} \rangle$ Curves, Weak Turbulence, Pr_{fade} = 0.015002

At moderate turbulence, the 8-laser array is no longer usable. Both the $\boldsymbol{R}_8$ and $\boldsymbol{RM}(1,3)/\boldsymbol{RS}(255,32)$ codes exhibit high $\langle \text{BER} \rangle$ and high variability. At the 16- and 24-laser size, the higher-rate concatenated codes (ie, those based on $\boldsymbol{NR}_{16}$ and $\boldsymbol{G}_{24}$) exhibit equally poor performance. At all sizes, the Reed-Muller based concatenated codes and the repetition codes perform similarly, and achieve usable rates at 20 dB for sizes 16 and up. Table 5 and Figure 15 contain these results.

Table 5. Experiment 1 Results, $\chi^2 = 1$, $\text{Pr}_{fade} = 0.074877$

Size	**Code**	**Stable Region**	$\bar{X}$	**SD**
	No FEC	30-50 dB	0.03744	n/a
8	$\boldsymbol{RS}(64,32)$	30-50 dB	3.9812×10^{-3}	1.4557×10^{-2}
	$\boldsymbol{RM}(1,3)/\boldsymbol{RS}(255,32)$	30-50 dB	6.4801×10^{-4}	8.7636×10^{-3}
	$\boldsymbol{R}_8$	30-50 dB	3.0700×10^{-4}	5.0326×10^{-3}
16	$\boldsymbol{RS}(128,32)$	**30-50 dB***	9.8683×10^{-3}	1.8430×10^{-2}
	$\boldsymbol{RM}(1,4)/\boldsymbol{RS}(255,32)$	20-50 dB	0	0
	$\boldsymbol{NR}_{16}/\boldsymbol{RS}(255,32)$	**30-50 dB***	3.9480×10^{-4}	4.3458×10^{-3}
	$\boldsymbol{R}_{16}$	20-50 dB	0	0
24	$\boldsymbol{RS}(120,20)$	30-50 dB	1.9529×10^{-2}	2.2357×10^{-2}
	$\boldsymbol{G}_{24}/\boldsymbol{RS}(255,32)$	30-50 dB	3.8955×10^{-5}	4.6064×10^{-4}
	$\boldsymbol{R}_{24}$	**20-50 dB***	0	0
32	$\boldsymbol{RS}(128,16)$	**30-50 dB***	2.5966×10^{-2}	1.9760×10^{-2}
	$\boldsymbol{RM}(1,5)/\boldsymbol{RS}(255,32)$	20-50 dB	0	0
	$\boldsymbol{R}_{32}$	20-50 dB	0	0

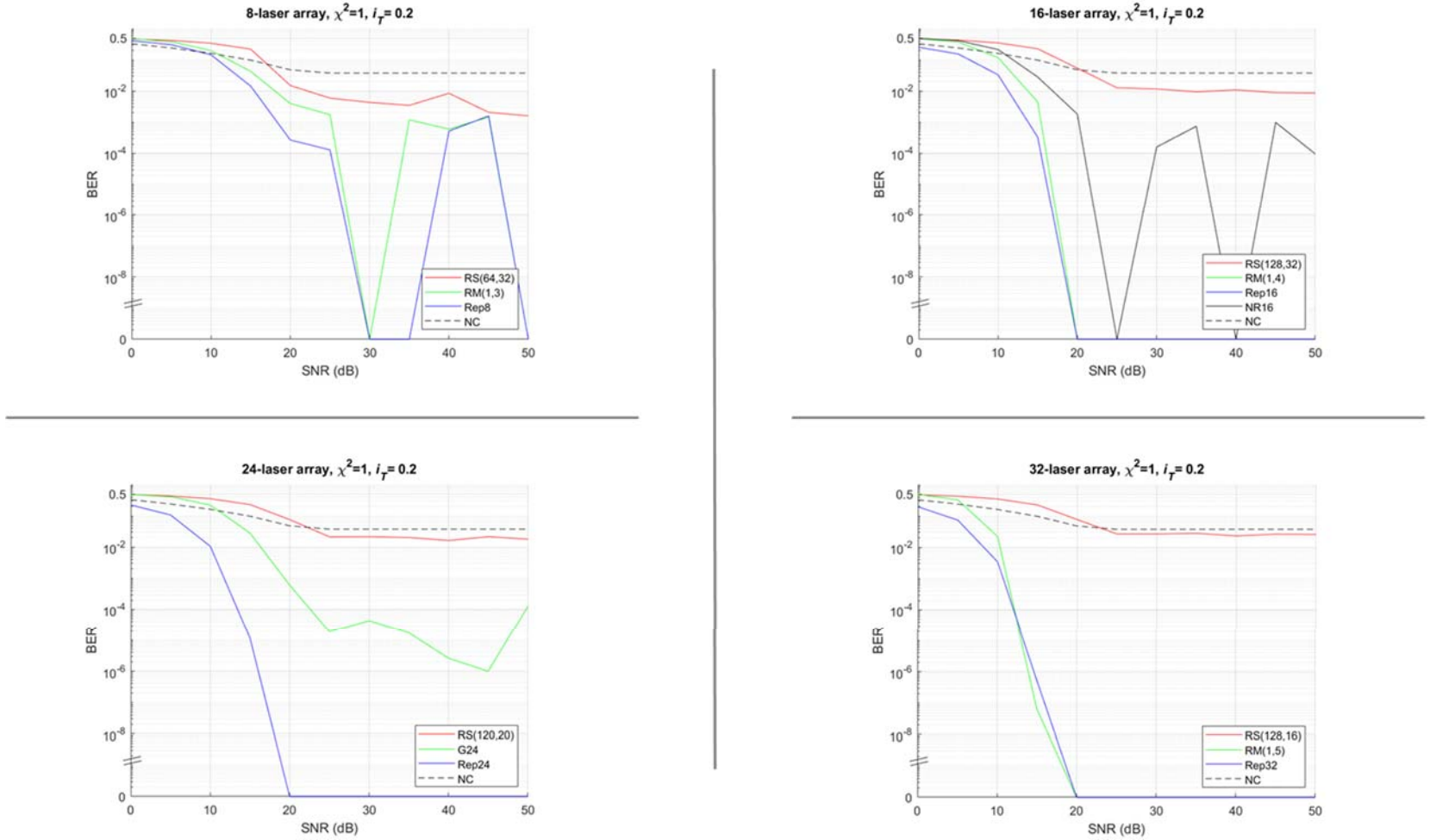

Figure 15. Experiment 1 $\langle$BER$\rangle$ Curves, Moderate Turbulence, Pr_{fade} = 0.074877

At high turbulence, the 16-laser array becomes unusable as well. Only $\boldsymbol{R}_{24}$, $\boldsymbol{R}_{32}$ and the ***RM***(1,5)-based concatenated code achieve a suitable level of performance, at 25 dB for all. As before, the Reed-Muller and repetition codes exhibit similar performance in the regions of interest. These results are displayed in Table 6 and Figure 16.

Table 6. Experiment 1 Results, $\chi^2 = 5$, $Pr_{fade} = 0.10734$

Size	**Code**	**Stable Region**	$\bar{X}$	**SD**
	No FEC	35-50 dB	0.05367	n/a
8	***RS***(64,32)	35-50 dB	8.8345×10^{-3}	2.1651×10^{-2}
	RM(1,3)/***RS***(255,32)	35-50 dB	3.1600×10^{-3}	1.7860×10^{-2}
	$\boldsymbol{R}_8$	35-50 dB	4.1576×10^{-3}	2.2273×10^{-2}
16	***RS***(128,32)	35-50 dB	2.6524×10^{-2}	3.0026×10^{-2}
	RM(1,4)/***RS***(255,32)	30-50 dB	2.0753×10^{-4}	4.6405×10^{-3}
	$\boldsymbol{NR}_{16}$/***RS***(255,32)	35-50 dB	1.8224×10^{-3}	1.1443×10^{-2}
	$\boldsymbol{R}_{16}$	35-50 dB	3.1350×10^{-5}	4.4281×10^{-4}
24	***RS***(120,20)	35-50 dB	3.9718×10^{-2}	2.7168×10^{-2}
	$\boldsymbol{G}_{24}$/***RS***(255,32)	35-50 dB	5.7766×10^{-4}	5.8305×10^{-3}
	$\boldsymbol{R}_{24}$	**25-50 dB***	0	0
32	***RS***(128,16)	**35-50 dB***	4.6092×10^{-2}	2.4030×10^{-2}
	RM(1,5)/***RS***(255,32)	25-50 dB	0	0
	$\boldsymbol{R}_{32}$	25-50 dB	0	0

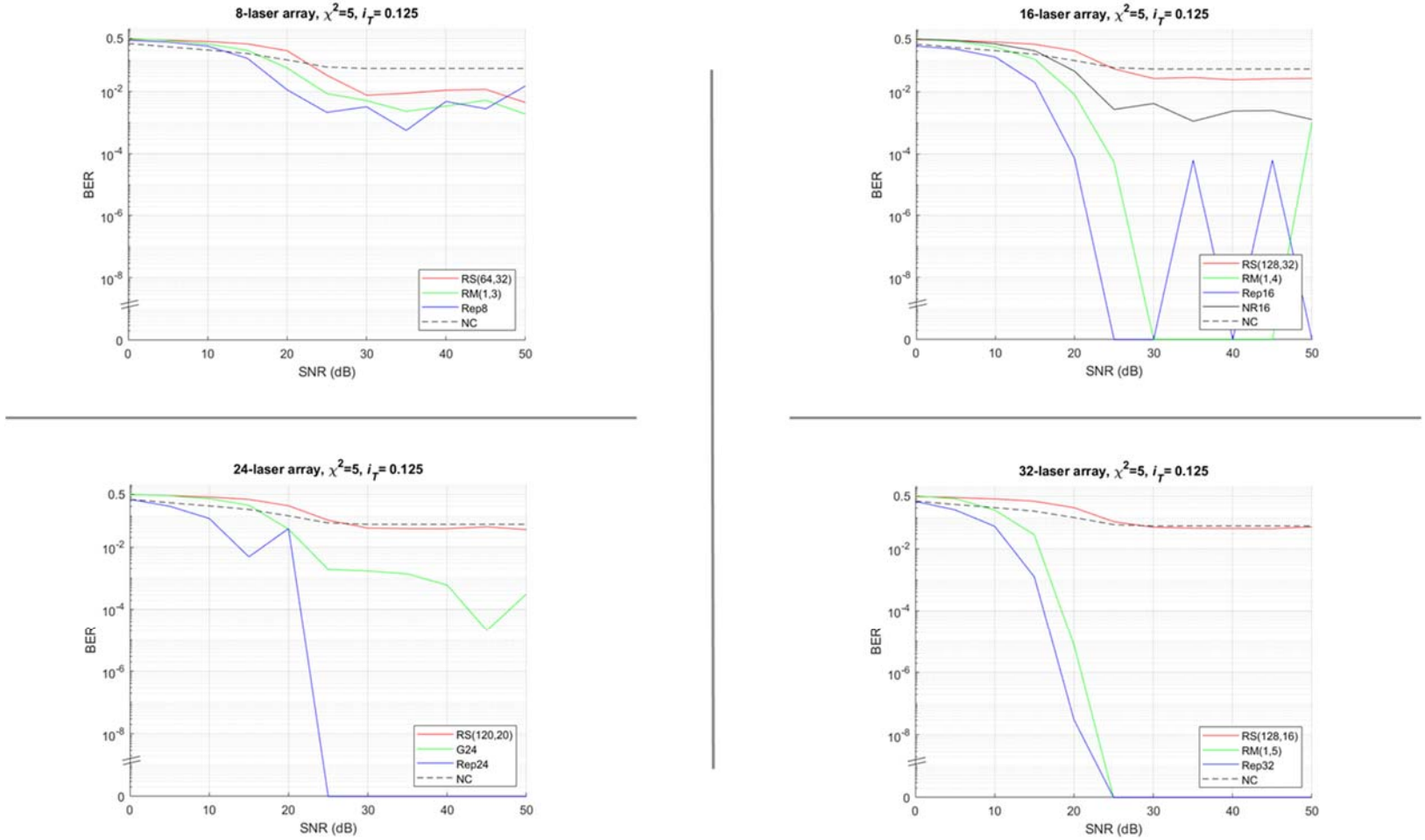

Figure 16. Experiment 1 $\langle \text{BER} \rangle$ curves, Strong Turbulence, Pr_{fade} = 0.10734

These results held for the saturation regime displayed in Table 7 and Figure 17, despite the fact that the threshold value of i_T was held constant at 0.125 for both the strong turbulence and saturation cases. The results for the 16-laser ***RM***(1,4)-based concatenated and repetition codes indicate usability above 35 dB; however, given the previous unsatisfactory results at a lower Pr_{fade} it is expected that actual performance would be too variable over a longer observation time. This is borne out by the variability apparent in the $\boldsymbol{R}_{16}$ code between 25 and 35 dB, which was caused by a single deep fade rather than noise. Otherwise, the same codes that performed satisfactorily under the strong turbulent conditions continued to perform satisfactorily in the saturation regime.

Table 7. Experiment 1 Results, $\chi^2 = 25$, $Pr_{fade} = 0.12579$

Size	**Code**	**Stable Region**	$\bar{X}$	**SD**
	No FEC	35-50 dB	0.062895	n/a
8	***RS***(64,32)	35-50 dB	1.2891×10^{-2}	2.6618×10^{-2}
	RM(1,3)/***RS***(255,32)	35-50 dB	3.8826×10^{-3}	1.8993×10^{-2}
	$\boldsymbol{R}_8$	35-50 dB	3.5028×10^{-3}	1.8183×10^{-2}
16	***RS***(128,32)	**35-50 dB***	3.7047×10^{-2}	3.5793×10^{-2}
	RM(1,4)/***RS***(255,32)	35-50 dB	0	0
	$\boldsymbol{NR}_{16}$/***RS***(255,32)	**35-50 dB***	4.3703×10^{-3}	2.1451×10^{-2}
	$\boldsymbol{R}_{16}$	35-50 dB	0	0
24	***RS***(120,20)	35-50 dB	5.1317×10^{-2}	3.0581×10^{-2}
	$\boldsymbol{G}_{24}$/***RS***(255,32)	35-50 dB	3.0278×10^{-3}	1.4768×10^{-2}
	$\boldsymbol{R}_{24}$	**25-50 dB***	0	0
32	***RS***(128,16)	**35-50 dB***	5.4502×10^{-2}	2.3733×10^{-2}
	RM(1,5)/***RS***(255,32)	25-50 dB	0	0
	$\boldsymbol{R}_{32}$	25-50 dB	0	0

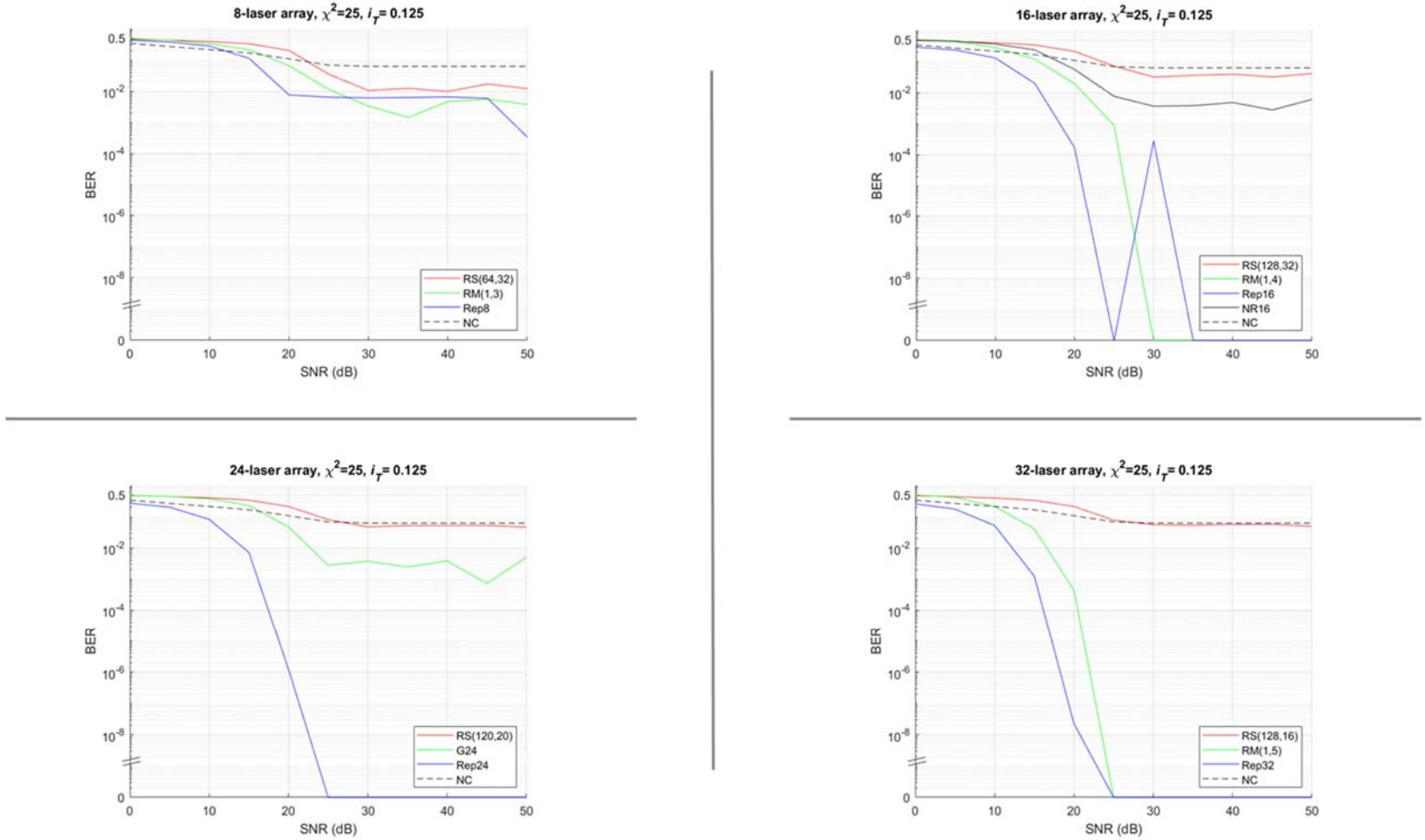

Figure 17. Experiment 1 $\langle \text{BER} \rangle$ Curves, Saturation Regime, Pr_{fade} = 0.12579

C. EXPERIMENT 2: REDUCED THRESHOLD VALUES

This experiment compares the results of high-, mid- and low-rate codes using two different threshold values (i_T). As an example, the channel probabilities for two threshold values are presented for the moderate turbulence case in Figure 18.

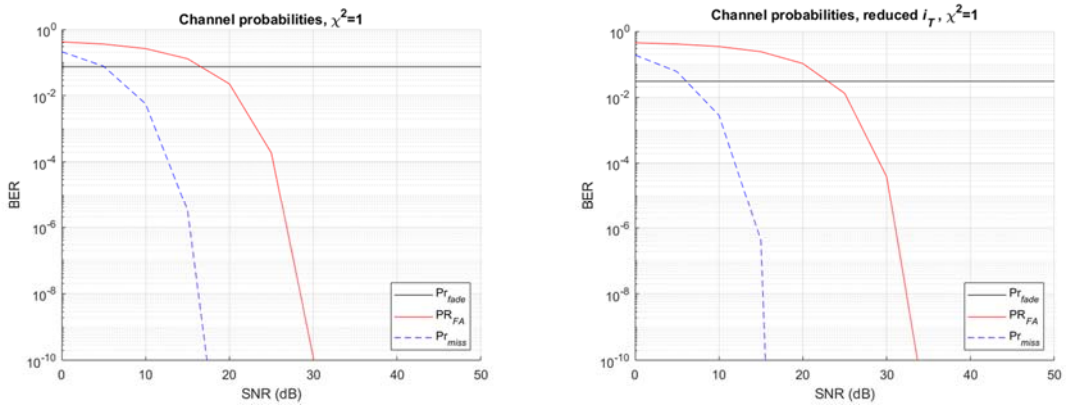

Figure 18. Channel Probabilities Compared, $i_T = 0.33$ (L) and $i_T = 0.25$ (R)

While the two graphs display similar properties, two key differences are that the Pr_{fade} has been reduced and the downwardly asymptotic portion of the Pr_{FA} curve has shifted to the right by nearly 5 dB of SNR. (The Pr_{miss} has decreased in terms of SNR, however not nearly as much as Pr_{FA} has increased.) SNR requirements may thus be traded for protection against fades.

Figures 19–22 show the results of this experiment, grouped by code type. For the high-rate codes, the only appreciable improvement at reasonable levels of i_T was in the low turbulence case where $\chi^2 = 0.2$. For the concatenated and repetition codes, results are displayed for medium and high turbulence ($\chi^2 = 1, 5$). Table 8 summarizes these results. Overall, the null hypothesis was rejected in a little more than half of the cases at the 95% significance level. In nearly every case where differences were observed, either achieved $\langle \text{BER} \rangle$, variability, or both were decreased by a factor of at least 10^{-1}. However, especially when performance was already good, this typically came at a price of approximately 5 dB

of SNR. The only exception was with $\boldsymbol{R}_8$, where variability worsened by an order of magnitude at moderate turbulence. This was caused by a single long-duration fade at 35 dB SNR, and illustrates the sensitivity of the smaller-sized array to even a low probability of fade; the difference, however, did not register as significant.

Table 8. Experiment 2: Varied i_T

Weak Turbulence ($\chi^2 = 0.2$)	***Initial i_T***			***Reduced i_T***		
	SR_0	**$\bar{X}_0$**	**SD_0**	**SR_1**	**$\bar{X}_1$**	**SD_1**
RS(64,32)	25-50 dB	6.0271×10^{-5}	1.4763×10^{-3}	25-50 dB	0	0
RS(128,32)	25-50 dB	9.3959×10^{-5}	1.1078×10^{-3}	**25-50 dB***	0	0
RS(120,20)	25-50 dB	2.1300×10^{-4}	1.4143×10^{-3}	**25-50 dB***	7.2025×10^{-6}	1.7642×10^{-4}
RS(128,16)	25-50 dB	4.1186×10^{-4}	2.1842×10^{-3}	**25-50 dB***	1.9514×10^{-5}	3.5321×10^{-4}
Mod Turbulence ($\chi^2 = 1$)	***Initial i_T***			***Reduced i_T***		
	SR_0	**$\bar{X}_0$**	**SD_0**	**SR_1**	**$\bar{X}_1$**	**SD_1**
RM(1,3)/***RS***(255,32)	30-50 dB	6.4801×10^{-4}	8.7636×10^{-3}	30-50 dB	0	0
RM(1,4)/***RS***(255,32)	20-50 dB	0	0	25-50 dB	0	0
RM(1,5)/***RS***(255,32)	20-50 dB	0	0	20-50 dB	0	0
$\boldsymbol{NR}_{16}$/***RS***(255,32)	30-50 dB	3.9480×10^{-4}	4.3458×10^{-3}	**25-50 dB***	0	0
$\boldsymbol{G}_{24}$/***RS***(255,32)	30-50 dB	3.8955×10^{-5}	4.6064×10^{-4}	**25-50 dB***	0	0
$\boldsymbol{R}_8$	30-50 dB	3.0700×10^{-4}	5.0326×10^{-3}	30-50 dB	5.0637×10^{-4}	1.0127×10^{-2}
$\boldsymbol{R}_{16}$	20-50 dB	0	0	20-50 dB	0	0
$\boldsymbol{R}_{24}$	20-50 dB	0	0	**25-50 dB***	0	0
$\boldsymbol{R}_{32}$	20-50 dB	0	0	**25-50 dB***	0	0
Strong Turbulence ($\chi^2 = 5$)	***Initial i_T***			***Reduced i_T***		
	SR_0	**$\bar{X}_0$**	**SD_0**	**SR_1**	**$\bar{X}_1$**	**SD_1**
RM(1,3)/***RS***(255,32)	35-50 dB	3.1600×10^{-3}	1.7860×10^{-2}	**35-50 dB***	4.4758×10^{-4}	6.0414×10^{-3}
RM(1,4)/***RS***(255,32)	35-50 dB	2.5941×10^{-4}	5.1882×10^{-3}	35-50 dB	0	0
RM(1,5)/***RS***(255,32)	25-50 dB	0	0	25-50 dB	0	0
$\boldsymbol{NR}_{16}$/***RS***(255,32)	35-50 dB	1.8224×10^{-3}	1.1443×10^{-2}	**35-50 dB***	0	0
$\boldsymbol{G}_{24}$/***RS***(255,32)	35-50 dB	5.7766×10^{-4}	5.8305×10^{-3}	35-50 dB	2.2569×10^{-4}	4.5136×10^{-3}
$\boldsymbol{R}_8$	35-50 dB	4.1576×10^{-3}	2.2273×10^{-2}	**35-50 dB***	0	0
$\boldsymbol{R}_{16}$	35-50 dB	3.1350×10^{-5}	4.4281×10^{-4}	35-50 dB	0	0
$\boldsymbol{R}_{24}$	25-50 dB	0	0	**30-50 dB***	0	0
$\boldsymbol{R}_{32}$	25-50 dB	0	0	**30-50 dB***	0	0

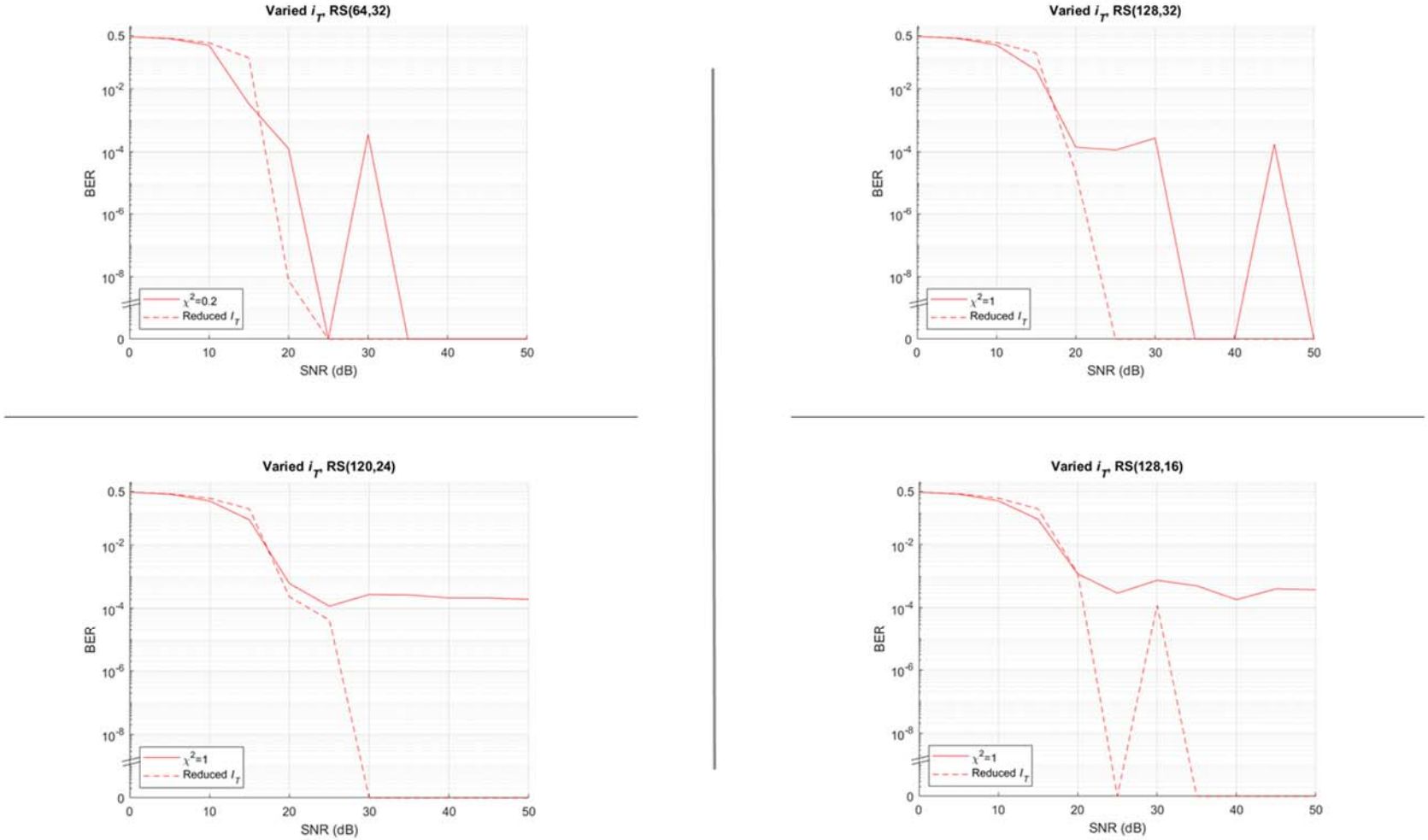

Figure 19. Experiment 2: Reed-Solomon Codes, $\chi^2 = 0.2$

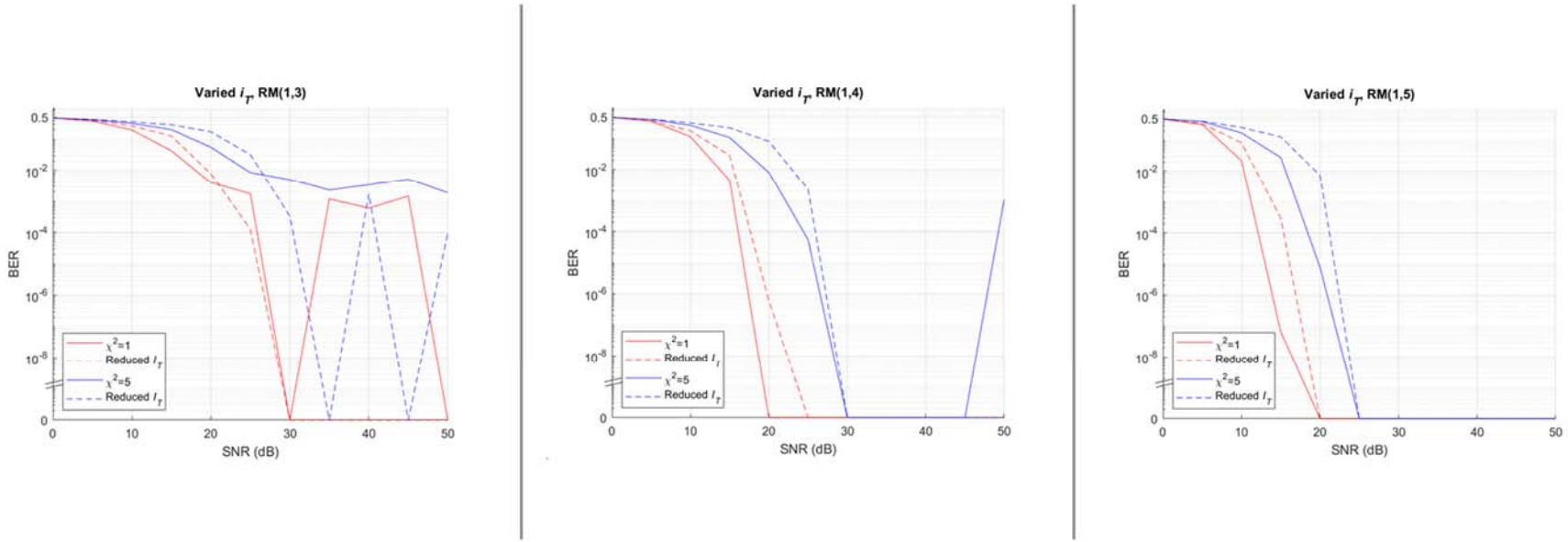

Figure 20. Experiment 2: ***RM***-Based Concatenated Codes, $\chi^2 = 1, 5$

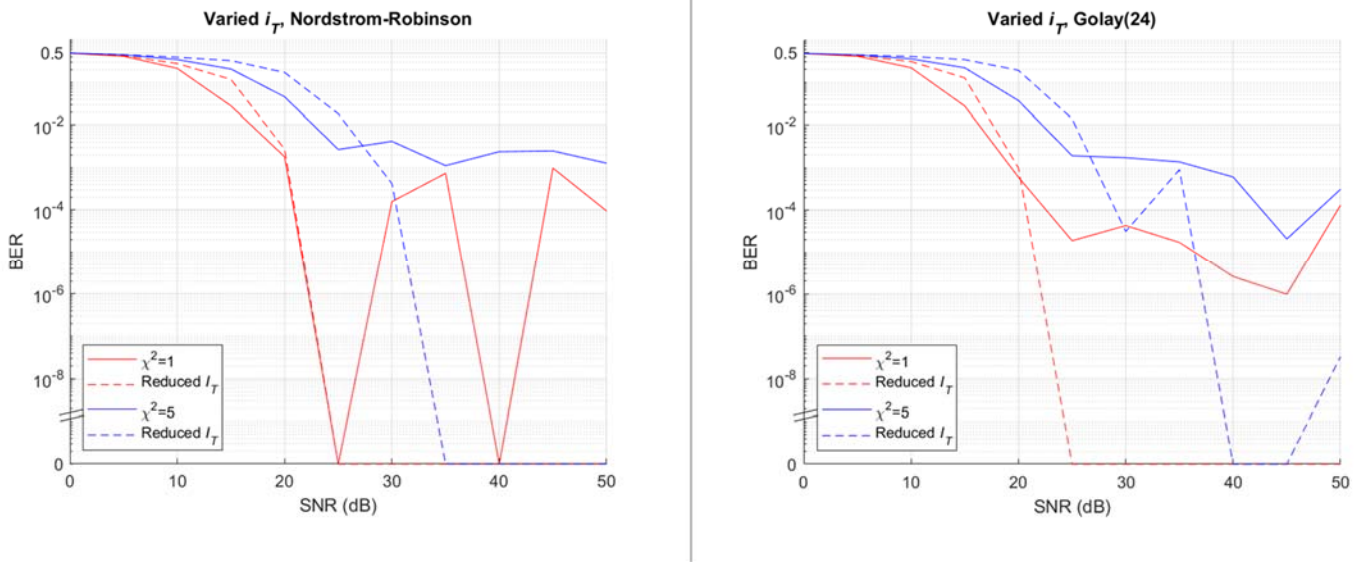

Figure 21. Experiment 2: Nordstrom-Robinson and Golay-based Concatenated Codes, χ^2 = 1,5

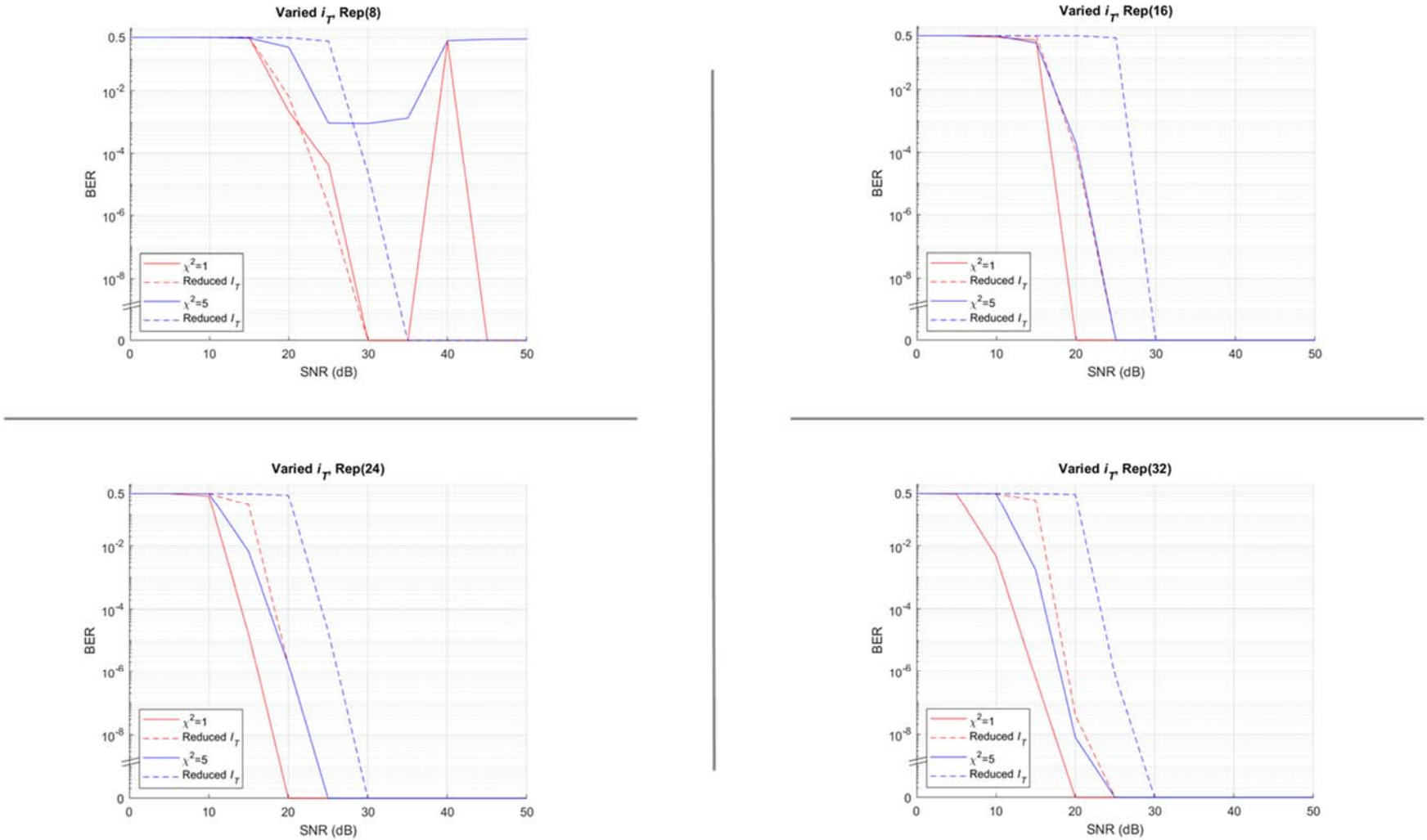

Figure 22. Experiment 2: Repetition codes, $\chi^2 = 1,5$

D. EXPERIMENT 3: EFFECT OF E_B ON PERFORMANCE

This experiment compared the ***RM***-based concatenated codes directly with the repetition codes at the 8-, 16- and 32-laser size. Since both types of codes share the same Pr(Outage) at a given size and channel state, this permits direct comparison of the effect of E_b on performance. At the 8-laser size, no significant differences were observed, and variability in the results was high for one or the other code (or both) at every level of Pr_{fade} observed. Thus, performance may be assessed to be equally poor at all levels, noting again the sensitivity of this array in general to even a single deep fade during the observation periods. No significant differences were found at the 16-laser size. With 32 lasers the ***RM***(1,5)-based concatenated code showed statistically significant coding gains of up to 5 dB at low Pr_{fade}. At the two higher Pr_{fade}, performance was virtually identical as measured by the three chosen indicators.

Therefore, in the majority of cases the null hypothesis failed to be rejected. Normalized E_b was only associated with a performance difference in the larger array sizes—and in inverse proportion, i.e., a lower E_b correlated with a wider stable region. This is possibly explained by the action of the outer code, which handled errors due to noise in the less turbulent regions, where the channel might be degraded but not completely down due to turbulence. Tables 9–11 and Figures 23–25 summarize and display these results.

Table 9. Experiment 3: 8-Laser Array

Pr_{fade}	Code	Pr(Out)	E_b / i_s^2	Stable Region	$\bar{X}$	SD
0.030532	***RM***(1,3)/***RS***(255,32)	5.51×10^{-5}	2.30×10^{-8}	30-50 dB	0	0
	R_8	5.51×10^{-5}	4.00×10^{-8}	30-50 dB	5.0637×10^{-4}	1.0127×10^{-2}
0.049086	***RM***(1,3)/***RS***(255,32)	3.46×10^{-4}	2.30×10^{-8}	35-50 dB	4.4758×10^{-4}	6.0414×10^{-3}
	R_8	3.46×10^{-4}	4.00×10^{-8}	35-50 dB	0	0
0.074877	***RM***(1,3)/***RS***(255,32)	1.72×10^{-3}	2.30×10^{-8}	30-50 dB	6.4801×10^{-4}	8.7636×10^{-3}
	R_8	1.72×10^{-3}	4.00×10^{-8}	30-50 dB	3.0700×10^{-4}	5.0326×10^{-3}
0.10734	***RM***(1,3)/***RS***(255,32)	6.50×10^{-3}	2.30×10^{-8}	35-50 dB	3.1600×10^{-3}	1.7860×10^{-2}
	R_8	6.50×10^{-3}	4.00×10^{-8}	35-50 dB	4.1576×103	2.2273×10^{-2}

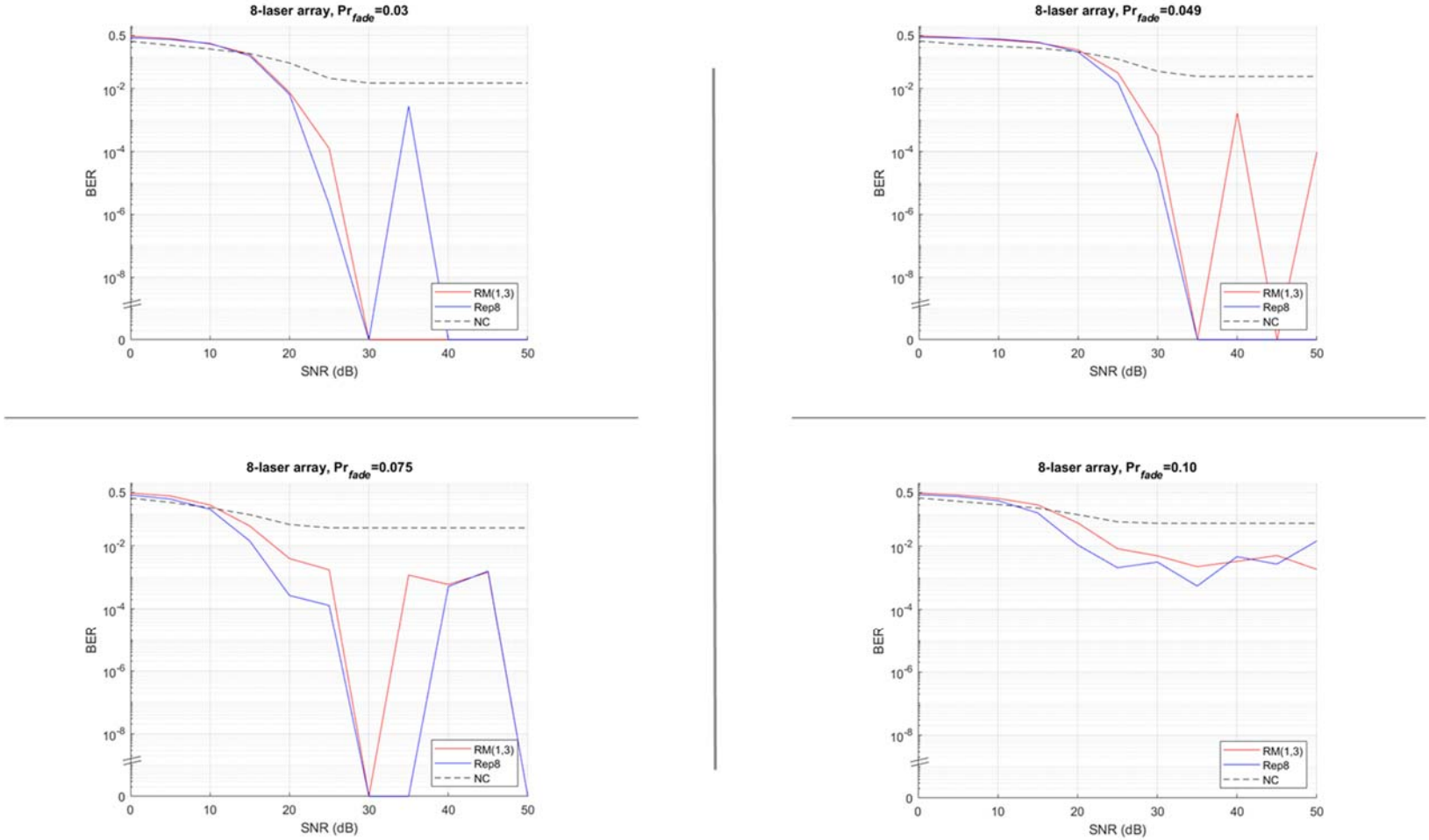

Figure 23. Experiment 3: 8-laser Array, Constant Pr(Outage), Varied E_b

Table 10. Experiment 3: 16-Laser Array

$\mathbf{Pr}_{fade}$	Code	Pr(Out)	E_b / i_s^2	Stable Region	$\bar{X}$	SD
0.030532	$\boldsymbol{RM}(1,4)/\boldsymbol{RS}(255,32)$	7.80×10^{-9}	3.67×10^{-8}	25-50 dB	0	0
	$\boldsymbol{R}_{16}$	7.80×10^{-9}	8.00×10^{-8}	25-50 dB	0	0
0.049086	$\boldsymbol{RM}(1,4)/\boldsymbol{RS}(255,32)$	3.04×10^{-7}	3.67×10^{-8}	30-50 dB	0	0
	$\boldsymbol{R}_{16}$	3.04×10^{-7}	8.00×10^{-8}	35-50 dB	0	0
0.074877	$\boldsymbol{RM}(1,4)/\boldsymbol{RS}(255,32)$	7.34×10^{-6}	3.67×10^{-8}	20-50 dB	0	0
	$\boldsymbol{R}_{16}$	7.34×10^{-6}	8.00×10^{-8}	20-50 dB	0	0
0.10734	$\boldsymbol{RM}(1,4)/\boldsymbol{RS}(255,32)$	1.02×10^{-4}	3.67×10^{-8}	35-50 dB	2.5941×10^{-4}	5.1882×10^{-3}
	$\boldsymbol{R}_{16}$	1.02×10^{-4}	8.00×10^{-8}	35-50 dB	3.1350×10^{-5}	4.4281×10^{-4}

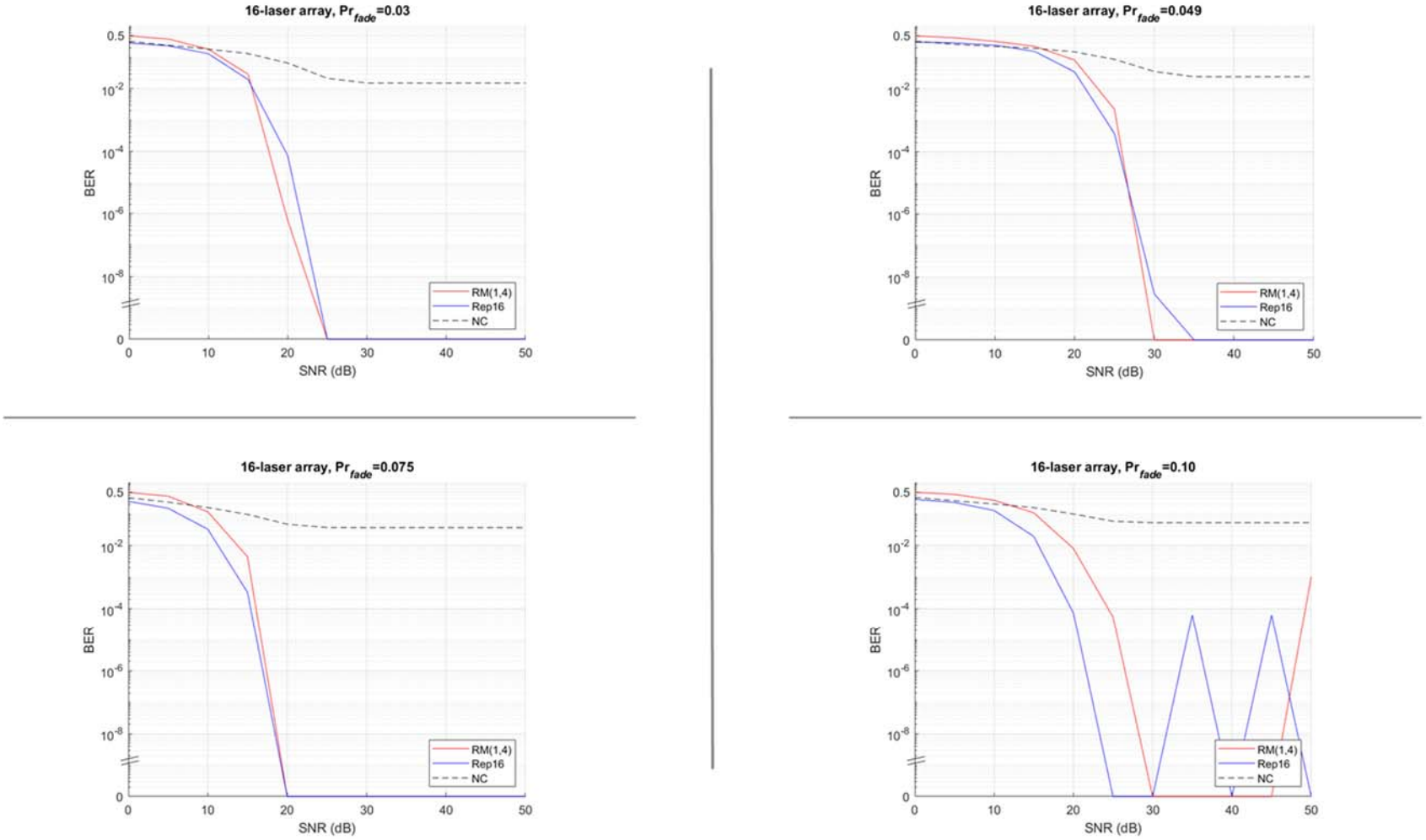

Figure 24. Experiment 3, 16-laser Array, Constant Pr(Outage), Varied E_b

Table 11. Experiment 3: 32-Laser Array

$\mathbf{Pr}_{fade}$	Code	Pr(Out)	E_b / i_s^2	Stable Region	$\bar{X}$	SD
0.030532	$\boldsymbol{RM}(1,5)/\boldsymbol{RS}(255,32)$	2.15×10^{-16}	6.12×10^{-8}	**20-50 dB***	0	0
	$\boldsymbol{R}_{32}$	2.15×10^{-16}	16.00×10^{-8}	25-50 dB	0	0
0.049086	$\boldsymbol{RM}(1,5)/\boldsymbol{RS}(255,32)$	3.21×10^{-13}	6.12×10^{-8}	**25-50 dB***	0	0
	$\boldsymbol{R}_{32}$	3.21×10^{-13}	16.00×10^{-8}	30-50 dB	0	0
0.074877	$\boldsymbol{RM}(1,5)/\boldsymbol{RS}(255,32)$	1.83×10^{-10}	6.12×10^{-8}	20-50 dB	0	0
	$\boldsymbol{R}_{32}$	1.83×10^{-10}	16.00×10^{-8}	20-50 dB	0	0
0.10734	$\boldsymbol{RM}(1,5)/\boldsymbol{RS}(255,32)$	3.42×10^{-8}	6.12×10^{-8}	25-50 dB	0	0
	$\boldsymbol{R}_{32}$	3.42×10^{-8}	16.00×10^{-8}	25-50 dB	0	0

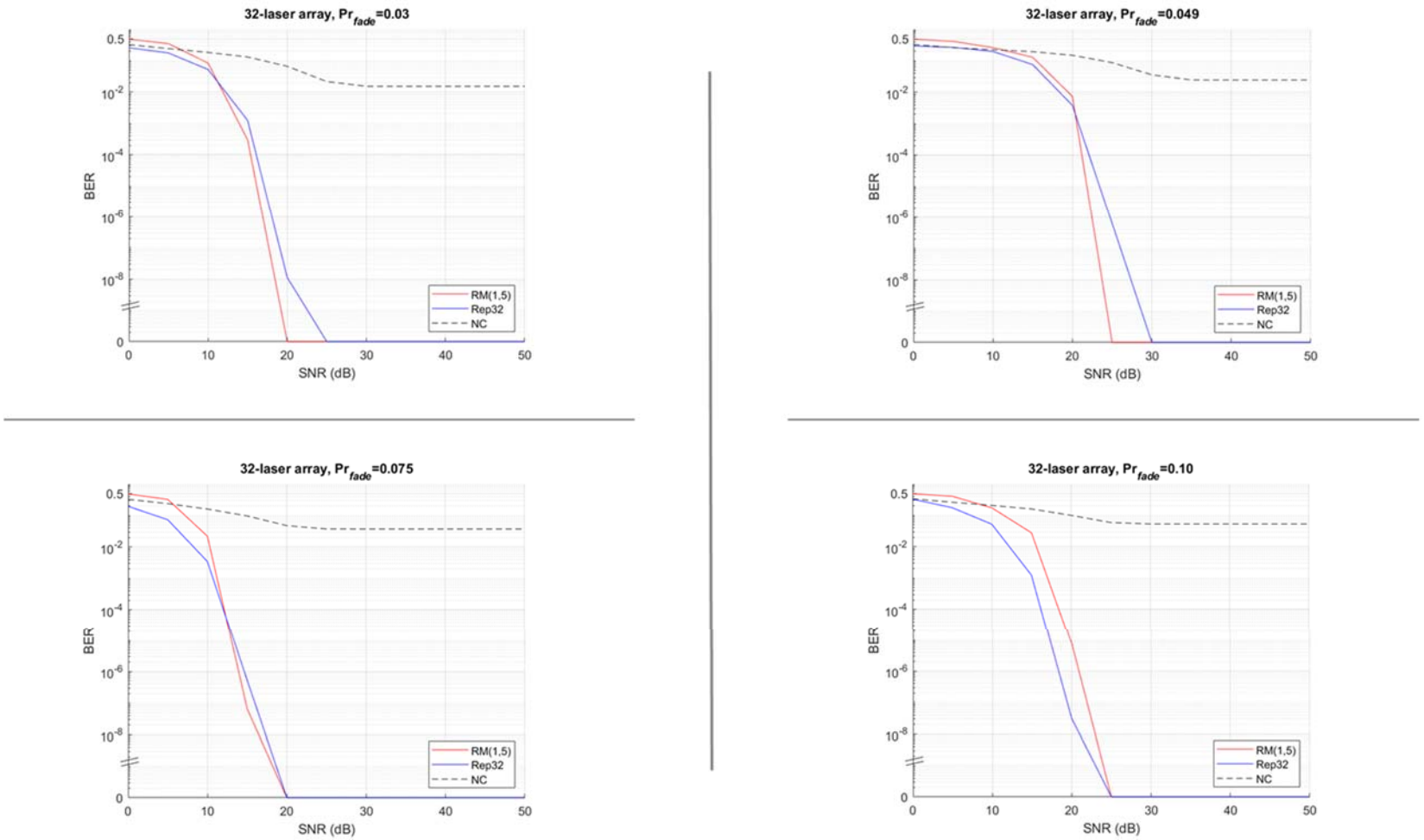

Figure 25. Experiment 3: 32-Laser Array, Constant Pr(Outage), Varied E_b

E. EXPERIMENT 4: EFFECT OF PR(OUTAGE) ON PERFORMANCE

Table 12 records the effect of Pr(Outage) on the performance of three concatenated codes with identical E_b. This is also plotted in Figure 26. These codes are tested at the same Pr_{fade} as in Experiment 3. The results clearly indicate that as Pr_{fade} increases, the performance of all codes observed decreases. However, performance between the three codes at each Pr_{fade} was difficult to distinguish; one-way ANOVA conducted between the three codes across each stable region found no significant differences at the 95% significance level. At Pr_{fade} = 0.049, even if the differences were significant, no useful conclusion can be drawn since the ***NR***-based Pr(Outage) is in between the other two. The null hypothesis failed to be rejected in all cases except the final test; however, the winning code ($\boldsymbol{G}_{24}$) was still unusable.

Table 12. Experiment 4: Constant E_b, Varied Pr(Outage)

Pr_{fade}	Code	Pr(Out)	E_b / i_s^2	Stable Region	$\bar{X}$	SD
0.030532	***RM***(1,3)/***RS***(255,32)	5.51×10^{-5}	2.30×10^{-8}	30-50 dB	0	0
	NR/***RS***(255,32)	4.98×10^{-6}	2.30×10^{-8}	25-50 dB	0	0
	$\boldsymbol{G}_{24}$/***RS***(255,32)	3.58×10-7	2.30×10^{-8}	25-50 dB	0	0
0.049086	***RM***(1,3)/***RS***(255,32)	3.46×10^{-4}	2.30×10^{-8}	35-50 dB	4.4758×10^{-4}	6.0414×10^{-3}
	NR/***RS***(255,32)	7.30×10^{-5}	2.30×10^{-8}	35-50 dB	0	0
	$\boldsymbol{G}_{24}$/***RS***(255,32)	1.22×10^{-5}	2.30×10^{-8}	35-50 dB	2.2569×10^{-4}	4.5136×10^{-3}
0.074877	***RM***(1,3)/***RS***(255,32)	1.72×10^{-3}	2.30×10^{-8}	35-50 dB	8.1001×10^{-4}	9.7938×10^{-3}
	NR/***RS***(255,32)	7.30×10^{-4}	2.30×10^{-8}	35-50 dB	4.5375×10^{-4}	4.7973×10^{-3}
	$\boldsymbol{G}_{24}$/***RS***(255,32)	2.43×10^{-4}	2.30×10^{-8}	35-50 dB	3.7887×10^{-5}	4.6878×10^{-4}
0.10734	***RM***(1,3)/***RS***(255,32)	6.50×10^{-3}	2.30×10^{-8}	35-50 dB	3.1600×10^{-3}	1.7860×10^{-2}
	NR/***RS***(255,32)	4.71×10^{-3}	2.30×10^{-8}	35-50 dB	1.8224×10^{-3}	1.1443×10^{-2}
	$\boldsymbol{G}_{24}$/***RS***(255,32)	2.65×10^{-3}	2.30×10^{-8}	**35-50 dB***	5.7766×10^{-4}	5.8305×10^{-3}

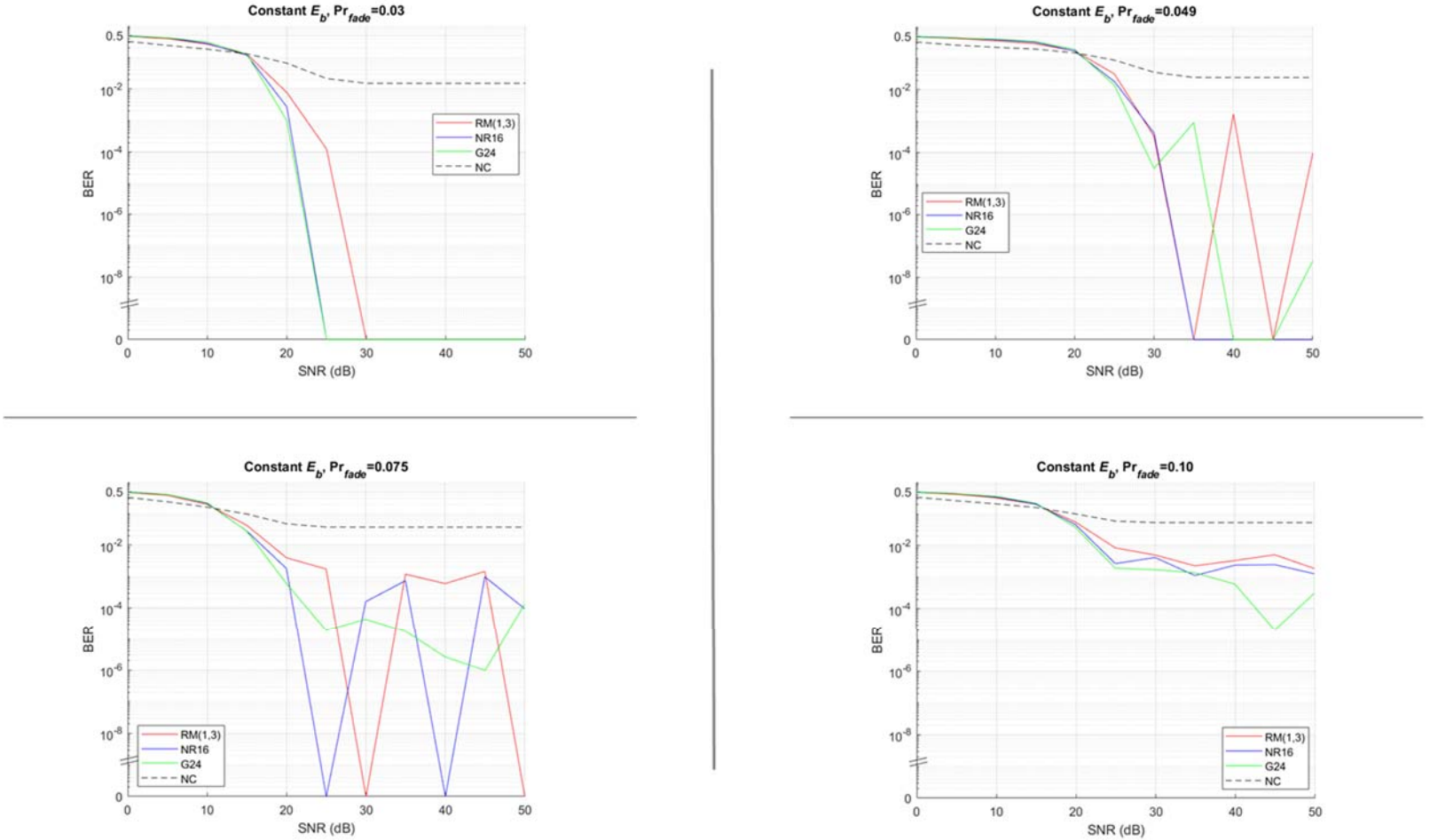

Figure 26. Experiment 4: Effects of Varied Pr(Outage), Constant E_b

F. SUMMARY OF RESULTS FROM EXPERIMENTS 3 AND 4 AND EXTENSION TO QR CODES

Overall observations from Experiments 3 and 4 indicate that a Pr(Outage) > 10–^{4} led to an unusable channel, regardless of E_b in the range observed. Pr(Outage) was a much better predictor of performance than E_b. However, it is worthwhile to note that in all cases E_b ranged from 2.30×10^{-8} to 16.00×10^{-8}. Thus, it may reasonably be concluded that a usable channel results from a combination of normalized E_b on the order of 10–^{8} or higher, and Pr(Outage) on the order of 10–^{4} and lower. This conclusion is borne out by the results of Experiments 1 and 2 regarding the Reed-Solomon codes in the low turbulence regime (Pr_{fade} = 0.000675, 0.003498 and 0.015002), as summarized in Table 13. As before the deciding factor appears to be Pr(Outage).

Table 13. Reed-Solomon Results, Experiments 1 and 2

Pr_{fade}	Code	Pr(Out)	E_b/i_s^2	Stable Region	$\bar{X}$	SD
0.000675	***RS***(64,32)	1.72×10^{-8}	1.00×10^{-8}	20-50 dB	0	0
	RS(128,32)	1.71×10^{-7}	0.67×10^{-8}	20-50 dB	0	0
	RS(120,20)	6.16×10^{-7}	0.60×10^{-8}	20-50 dB	0	0
	RS(128,16)	1.50×10^{-6}	0.29×10^{-8}	20-50 dB	0	0
0.003498	***RS***(64,32)	2.37×10^{-6}	1.00×10^{-8}	25-50 dB	0	0
	RS(128,32)	2.32×10^{-5}	0.67×10^{-8}	25-50 dB	0	0
	RS(120,20)	8.20×10^{-5}	0.60×10^{-8}	25-50 dB	7.2025×10^{-6}	1.7642×10^{-4}
	RS(128,16)	1.97×10^{-4}	0.29×10^{-8}	25-50 dB	1.9514×10^{-5}	3.5321×10^{-4}
0.015002	***RS***(64,32)	1.79×10^{-4}	1.00×10^{-8}	25-50 dB	6.0271×10^{-5}	1.4763×10^{-3}
	RS(128,32)	1.63×10^{-3}	0.67×10^{-8}	25-50 dB	9.3959×10^{-5}	1.1078×10^{-3}
	RS(120,20)	5.40×10^{-3}	0.60×10^{-8}	25-50 dB	2.1300×10^{-4}	1.4143×10^{-3}
	RS(128,16)	1.21×10^{-2}	0.29×10^{-8}	25-50 dB	4.1186×10^{-4}	2.1842×10^{-3}

With this predictive model in hand, an extension of these results is made to QR codes. For ease of comparison, a QR code-like array using the ***RS***(64,32) code is compared with an 8×8 laser array using the same ***RS***(64,32) code, but with the symbol/laser pairing proposed in this thesis. (Since the QR-type array requires 512 lasers, a 64-laser array should be equally feasible.) The QR-based array is equivalent to the Version 4, correction level Q QR code, with a notional error correction capability of 25%, as described by Denso Wave

(2019). Pr(Outage) is calculated using Equations 3.13, 3.1.42 and 3.1.43 and is displayed in Table 14 for each channel state and Pr_{fade} tested. Normalized E_b is the same for both arrays, and is equal to 1.00×10^{-8}.

Table 14. QR Performance Comparison

χ^2	i_T	Pr_{fade}	Pr(Out), QR	Pr(Out), 8×8
0.04	0.5	0.000675	2.94×10^{-24}	1.67×10^{-39}
0.2	0.25	0.003498	1.28×10^{-12}	2.08×10^{-27}
0.2	0.33	0.015002	6.35×10^{-4}	6.97×10^{-17}
1	0.125	0.030532	0.227	6.09×10^{-12}
5	0.0625	0.049086	0.896	8.33×10^{-9}
1	0.2	0.074877	0.998	3.28×10^{-6}
5	0.125	0.10734	0.999	3.18×10^{-4}
25	0.125	0.12579	0.999	1.93×10^{-3}

The table speaks for itself. While QR codes might be usable at weak turbulence levels, once Pr_{fade} reaches 0.01 and higher, Pr(Outage) quickly increases, passing the 10^{-5} threshold at $Pr_{fade} = 0.015$ and asymptotically approaching 1 as the turbulence becomes strong. The QR channel is therefore predicted to be useless at $Pr_{fade} > 0.015$. On the other hand, the 8×8 array transmitting the same code using symbol/laser pairing, given appropriate choice of i_T, delivers a usable channel up through the strong turbulence regime. Such an array remains usable up to $Pr_{fade} = 0.075$.

In summary, Figure 27 shows the calculated Pr(Outage) curve for each coding scheme tested plotted against Pr_{fade}. The curve for the QR array just described is also plotted in green. For each code, a red asterisk marks where the simulation resulted in an unusable channel, which occurred at values of Pr(Outage) at or just above 10^{-4}. Normalized E_b is plotted on the right-hand side.

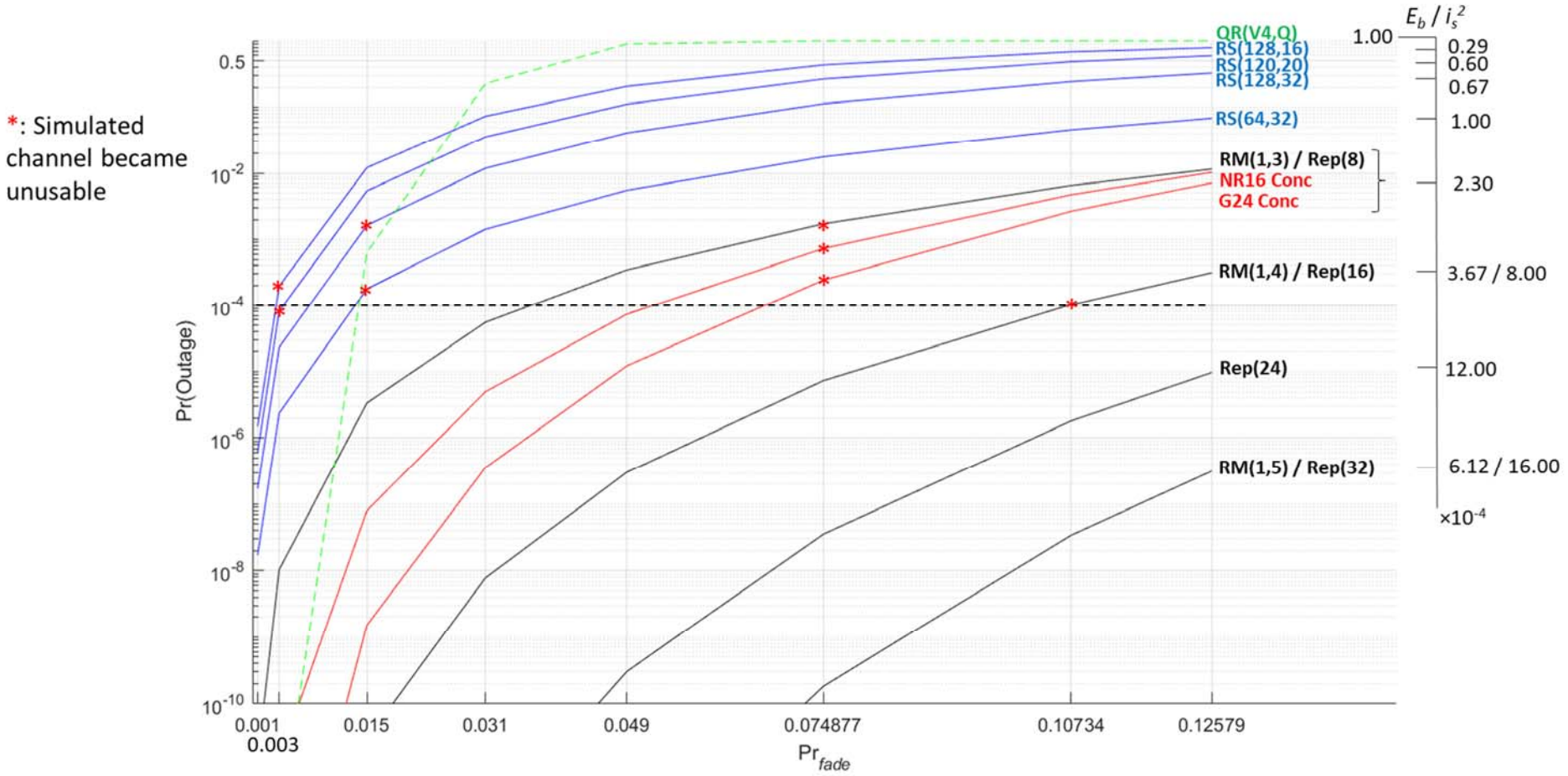

Figure 27. Channel Performance Thresholds

G. EXPERIMENT 5: EFFECT OF THE INTERLEAVER ON THE CONCATENATED (MEDIUM-RATE) CODES

Table 15, along with Figures 28 and 29, compare the results of the mid-rate codes with four different Pr_{fade} with simulations using the same parameters, but in which the interleaving step was omitted between the inner and outer codes. Very little difference was observed in the trials beyond a few shifts left or right in the stable region among the smaller size; these shifts did not register as significant at the 95% confidence level when a two-sample *t*-test was conducted between the code variants across the given stable region. Likewise, no significant differences in $\langle \text{BER} \rangle$ or variability were observed. Overall, the null hypothesis failed to be rejected. The 1 MB interleaver may be concluded to have little to no impact on code performance at the levels of turbulence tested.

Table 15. Experiment 5: Interleaver Test

Pr_{fade} = 0.030532	*With interleaver*			*Without interleaver*		
	SR_0	$\bar{X}_0$	SD_0	SR_1	$\bar{X}_1$	SD_1
RM(1,3)/***RS***(255,32)	30-50 dB	0	0	25-50 dB	0	0
RM(1,4)/***RS***(255,32)	25-50 dB	0	0	25-50 dB	0	0
RM(1,5)/***RS***(255,32)	20-50 dB	0	0	20-50 dB	0	0
NR_{16}/***RS***(255,32)	25-50 dB	0	0	25-50 dB	0	0
G_{24}/***RS***(255,32)	25-50 dB	0	0	25-50 dB	0	0
Pr_{fade} = 0.049086	*With interleaver*			*Without interleaver*		
	SR_0	$\bar{X}_0$	SD_0	SR_1	$\bar{X}_1$	SD_1
RM(1,3)/***RS***(255,32)	35-50 dB	4.4758×10^{-4}	6.0414×10^{-3}	35-50 dB	3.2892×10^{-3}	1.7215×10^{-2}
RM(1,4)/***RS***(255,32)	30-50 dB	0	0	30-50 dB	0	0
RM(1,5)/***RS***(255,32)	25-50 dB	0	0	25-50 dB	0	0
NR_{16}/***RS***(255,32)	35-50 dB	0	0	35-50 dB	0	0
G_{24}/***RS***(255,32)	35-50 dB	2.2569×10^{-4}	4.5136×10^{-3}	35-50 dB	3.2107×10^{-8}	6.4214×10^{-7}
Pr_{fade} = 0.074877	*With interleaver*			*Without interleaver*		
	SR_0	$\bar{X}_0$	SD_0	SR_1	$\bar{X}_1$	SD_1
RM(1,3)/***RS***(255,32)	30-50 dB	6.4801×10^{-4}	8.7636×10^{-3}	30-50 dB	4.1370×10^{-4}	7.2033×10^{-3}
RM(1,4)/***RS***(255,32)	20-50 dB	0	0	25-50 dB	0	0
RM(1,5)/***RS***(255,32)	20-50 dB	0	0	20-50 dB	0	0
NR_{16}/***RS***(255,32)	30-50 dB	3.9480×10^{-4}	4.3458×10^{-3}	30-50 dB	7.5301×10^{-4}	7.9670×10^{-3}
G_{24}/***RS***(255,32)	35-50 dB	3.7887×10^{-5}	4.6878×10^{-4}	35-50 dB	5.5617×10^{-5}	7.7904×10^{-4}
Pr_{fade} = 0.10734	*With interleaver*			*Without interleaver*		
	SR_0	$\bar{X}_0$	SD_0	SR_1	$\bar{X}_1$	SD_1
RM(1,3)/***RS***(255,32)	35-50 dB	3.1600×10^{-3}	1.7860×10^{-2}	35-50 dB	3.2892×10^{-3}	1.7215×10^{-2}
RM(1,4)/***RS***(255,32)	30-50 dB	2.0753×10^{-4}	4.6405×10^{-3}	30-50 dB	8.2872×10^{-6}	1.8531×10^{-4}
RM(1,5)/***RS***(255,32)	25-50 dB	0	0	25-50 dB	0	0
NR_{16}/***RS***(255,32)	35-50 dB	1.8224×10^{-3}	1.1443×10^{-2}	35-50 dB	1.8412×10^{-3}	1.2458×10^{-2}
G_{24}/***RS***(255,32)	35-50 dB	5.7766×10^{-4}	5.8305×10^{-3}	35-50 dB	1.4568×10^{-3}	1.0598×10^{-2}

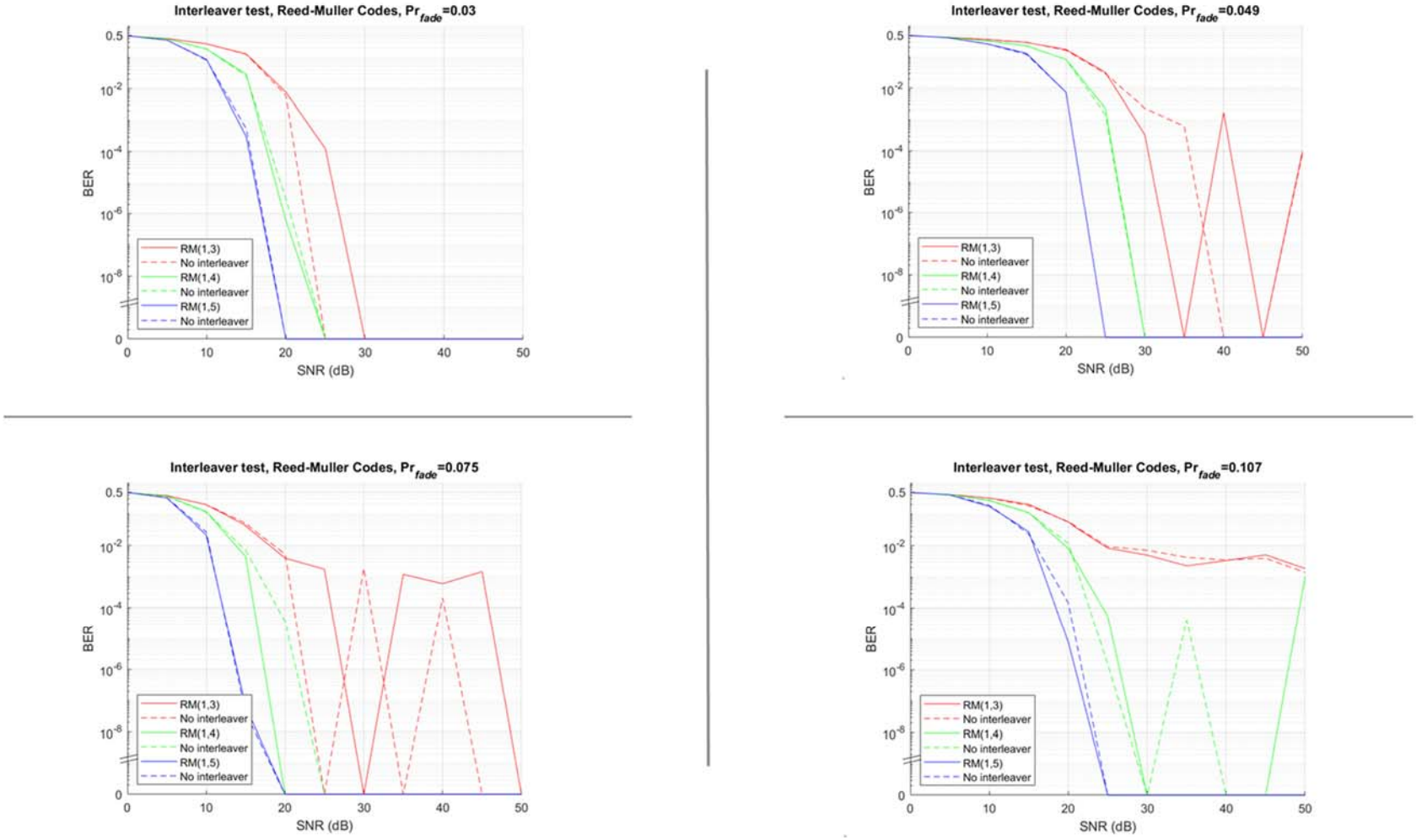

Figure 28. Effect of the Interleaver on the Reed-Muller Concatenated Codes

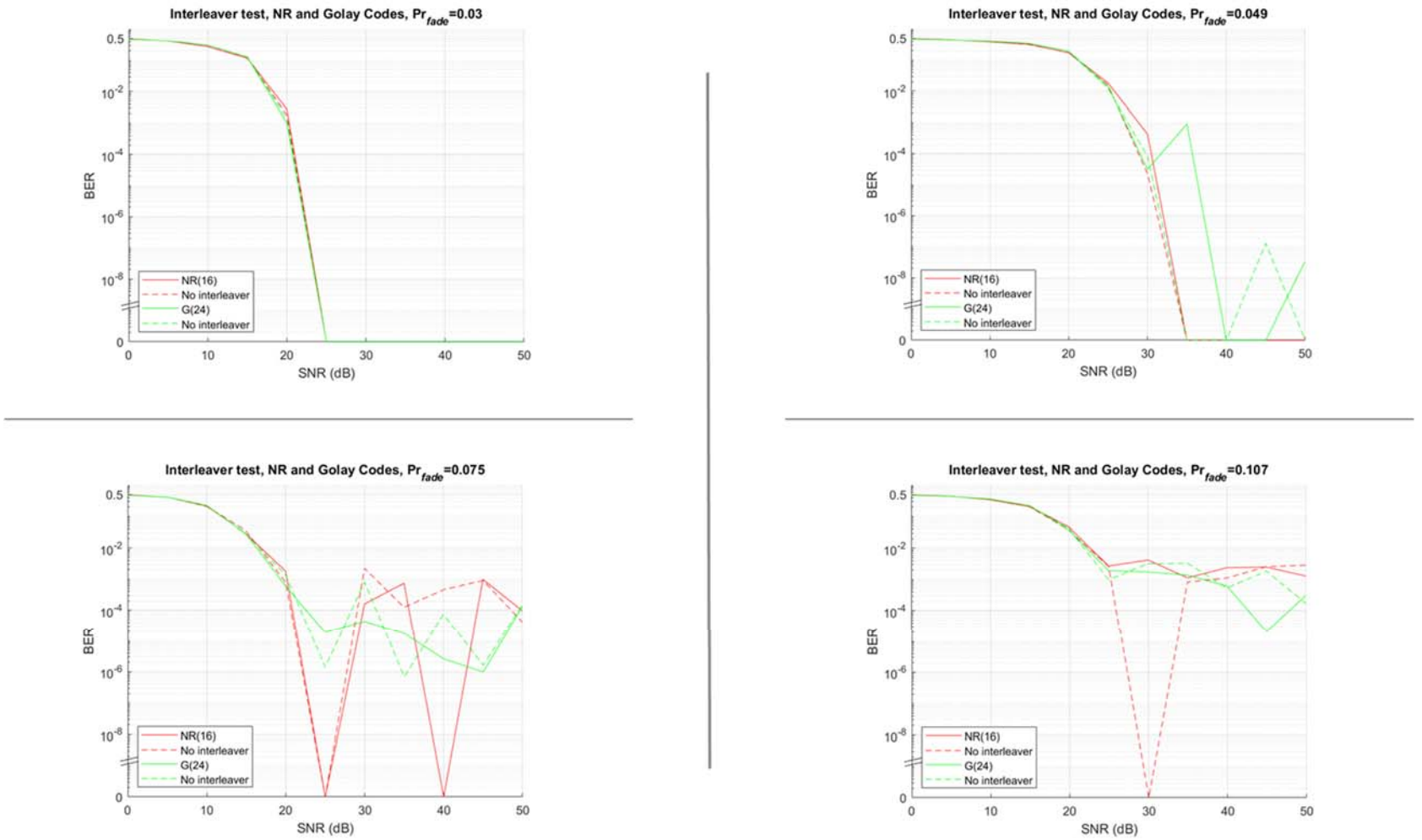

Figure 29. Effect of the Interleaver on the Nordstrom-Robinson and Golay Concatenated Codes

H. EXPERIMENT 6: EFFECT OF THE OUTER CODE ON THE CONCATENATED CODES

This section quantifies the effect of the outer code on the performance of the five selected concatenated codes. Results from the initial simulation were compared with results obtained using identical parameters, but with the outer coding and interleaving step omitted. Thus, for example a pure ***RM***(1,3) code was compared to a ***RS***(255,32) outer/***RM***(1,3) inner concatenated code with 1MB interleaver.

Removing the outer code measurably impacted performance for nearly every coding scheme at one or more of the levels of $\Pr_{fade}$ tested. In general, if the concatenated code achieved a $\langle \text{BER} \rangle$ of 0, removing the outer code pushed the stable region to the right by 5 or more dB. If the concatenated code did not achieve a usable (i.e., 0) $\langle \text{BER} \rangle$, performance without the outer code was typically worse in one or more of the parameters observed: e.g., a shifted stable region, increased variability, or increased $\langle \text{BER} \rangle$. As with previous observations, codes with higher Pr(Outage) and lower normalized E_b tended to display worse performance as $\Pr_{fade}$ increased.

The significance of the results was more pronounced at lower $\Pr_{fade}$, as determined by two-sample *t*-tests conducted at the 95% level between each pair of code variations across the stable regions. Outcomes became much more statistically similar, especially for the smaller sizes, as $\Pr_{fade}$ increased. The null hypothesis was rejected in the majority of cases at lower $\Pr_{fade}$, and here the outer code may be concluded to have a significant effect on performance—i.e., in the cases where coding gain is used to overcome the noise curve. Table 16 along with Figures 30 and 31 summarize and display these results.

Table 16. Experiment 6: Outer Code Test

Pr_{fade} = 0.030532	*With outer code*			*Without outer code*		
	SR_0	$\bar{X}_0$	SD_0	SR_1	$\bar{X}_1$	SD_1
RM(1,3)/***RS***(255,32)	30-50 dB	0	0	30-50 dB	0	0
RM(1,4)/***RS***(255,32)	25-50 dB	0	0	30-50 dB	0	0
RM(1,5)/***RS***(255,32)	20-50 dB	0	0	**25-50 dB***	0	0
NR_{16}/***RS***(255,32)	25-50 dB	0	0	**30-50 dB***	0	0
G_{24}/***RS***(255,32)	25-50 dB	0	0	**30-50 dB***	0	0
Pr_{fade} = 0.049086	*With outer code*			*Without outer code*		
	SR_0	$\bar{X}_0$	SD_0	SR_1	$\bar{X}_1$	SD_1
RM(1,3)/***RS***(255,32)	35-50 dB	4.4758×10^{-4}	6.0414×10^{-3}	40-50 dB	2.2800×10^{-3}	1.4231×10^{-2}
RM(1,4)/***RS***(255,32)	30-50 dB	0	0	**35-50 dB***	0	0
RM(1,5)/***RS***(255,32)	25-50 dB	0	0	**30-50 dB***	0	0
NR_{16}/***RS***(255,32)	35-50 dB	0	0	40-50 dB	0	0
G_{24}/***RS***(255,32)	35-50 dB	2.2569×10^{-4}	4.5136×10^{-3}	40-50 dB	1.2636×10^{-5}	1.2579×10^{-4}
Pr_{fade} = 0.074877	*With outer code*			*Without outer code*		
	SR_0	$\bar{X}_0$	SD_0	SR_1	$\bar{X}_1$	SD_1
RM(1,3)/***RS***(255,32)	30-50 dB	6.4801×10^{-4}	8.7636×10^{-3}	30-50 dB	1.1400×10^{-3}	1.4881×10^{-2}
RM(1,4)/***RS***(255,32)	20-50 dB	0	0	25-50 dB	0	0
RM(1,5)/***RS***(255,32)	20-50 dB	0	0	20-50 dB	0	0
NR_{16}/***RS***(255,32)	30-50 dB	3.9480×10^{-4}	4.3458×10^{-3}	30-50 dB	3.7050×10^{-4}	6.4003×10^{-3}
G_{24}/***RS***(255,32)	35-50 dB	3.7887×10^{-5}	4.6878×10^{-4}	35-50 dB	8.8009×10^{-5}	5.8153×10^{-4}
Pr_{fade} = 0.10734	*With outer code*			*Without outer code*		
	SR_0	$\bar{X}_0$	SD_0	SR_1	$\bar{X}_1$	SD_1
RM(1,3)/***RS***(255,32)	35-50 dB	3.1600×10^{-3}	1.7860×10^{-2}	35-50 dB	1.7100×10^{-3}	1.2359×10^{-2}
RM(1,4)/***RS***(255,32)	30-50 dB	2.0753×10^{-4}	4.6405×10^{-3}	30-50 dB	1.4272×10^{-4}	3.1913×10^{-3}
RM(1,5)/***RS***(255,32)	25-50 dB	0	0	30-50 dB	0	0
NR_{16}/***RS***(255,32)	35-50 dB	1.8224×10^{-3}	1.1443×10^{-2}	35-50 dB	1.3537×10^{-3}	1.0515×10^{-2}
G_{24}/***RS***(255,32)	35-50 dB	5.7766×10^{-4}	5.8305×10^{-3}	35-50 dB	1.5493×10^{-3}	9.1053×10^{-3}

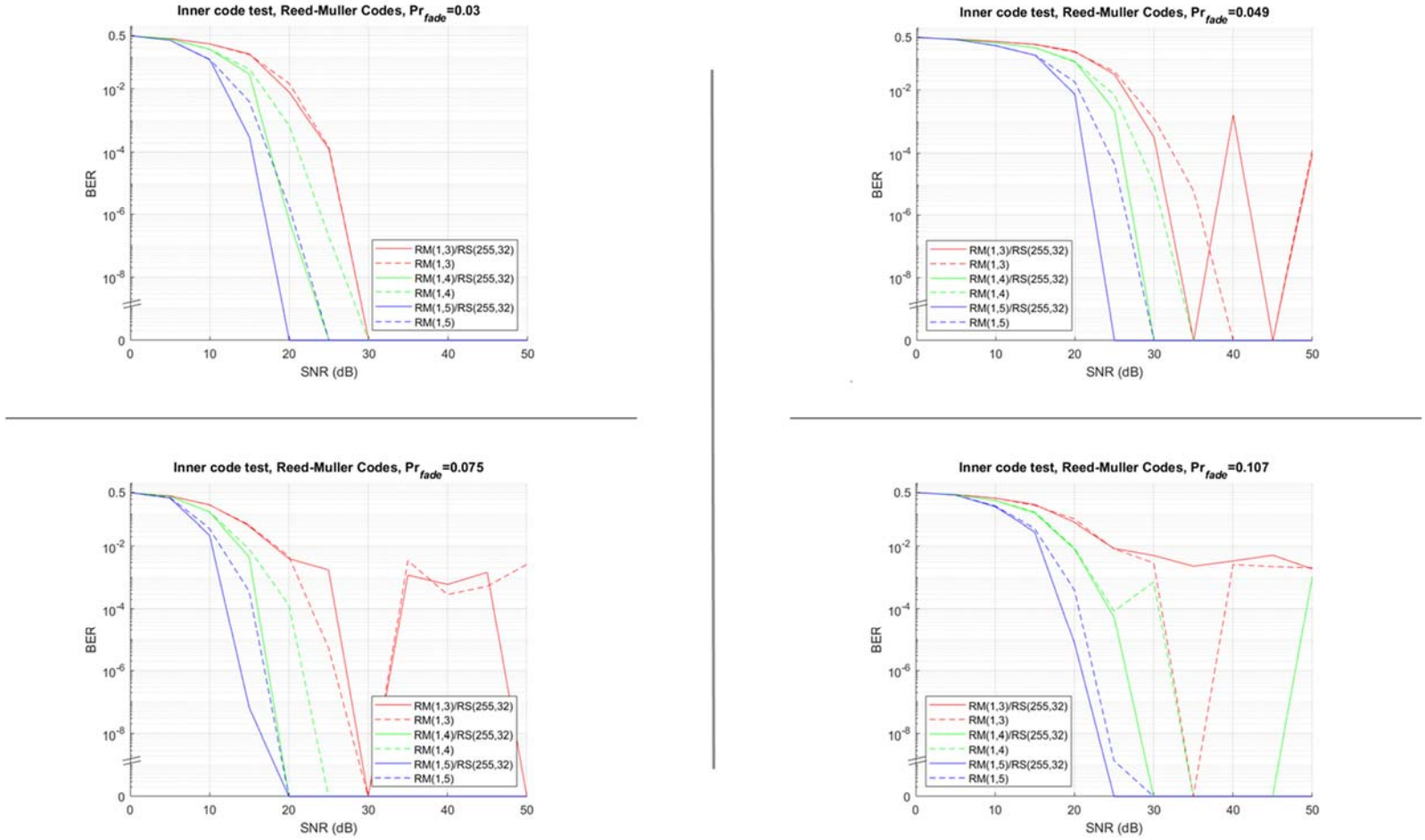

Figure 30. Effect of the Outer Code on the Reed-Muller Concatenated Codes

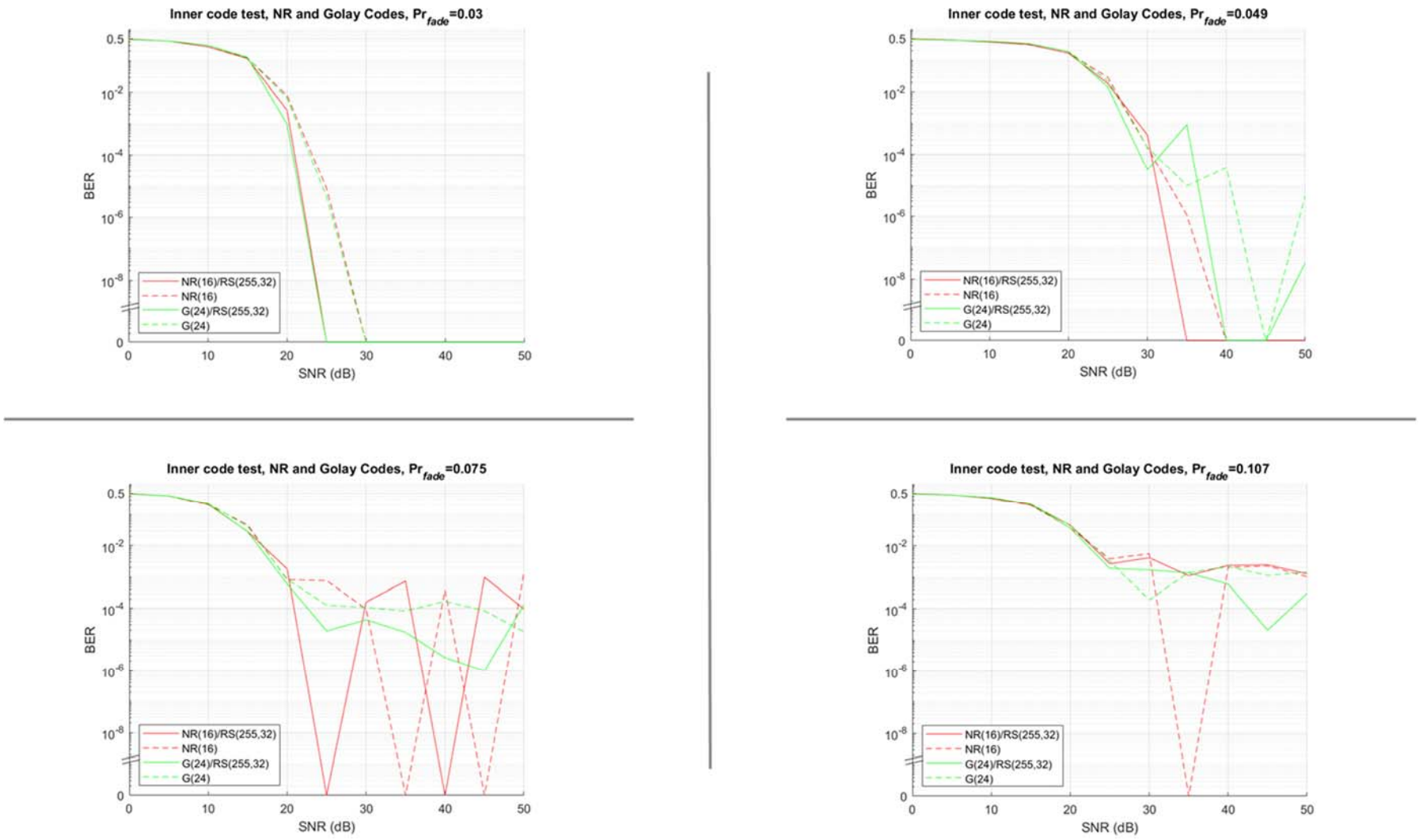

Figure 31. Effect of the Outer Code on the Nordstrom-Robinson and Golay codes

V. CONCLUSIONS AND RECOMMENDATIONS

Results are summarized in terms of the original research questions. Several recommended encoding schemes are presented, as well as refinements and extensions to the overall configuration. Finally, areas for future exploration and work are identified.

A. SUMMARY OF RESULTS

The principal research question was to determine how FEC encoding techniques might be applied to improve the reliability and efficiency of the MIMO FSO communications channel. Three basic categories of codes were identified and implemented in software, along with a simulator based on a statistical channel model. Two categories (repetition and Reed-Solomon codes, using OOK) are found in the literature. A third category, which combined a temporal channel code with various spatial line codes, was devised for this research. Overall, 13 different coding schemes were tested during the simulation phase. Previous work using QR codes was evaluated probabilistically.

Coding gains were identified for every scheme tested. At extremely low turbulence levels, where the channel resembled an AWGN channel, the high-rate codes performed satisfactorily. As turbulence (and thus Pr_{fade}) increased, the mid-rate codes continued to provide satisfactory performance. At high levels of turbulence ($\chi^2 > 1$) only codes with low Pr(Outage) performed satisfactorily.

An improved method for transmitting Reed-Solomon codewords over MIMO arrays was tested during the experimentation phase, in which each symbol was assigned and transmitted sequentially by a single laser using OOK. This significantly reduces the exposure of individual symbols, since they are only vulnerable to fading on one laser as opposed to eight. These coding schemes provided the highest coding efficiencies out of all the schemes tested, but also provided the least amount of protection against data loss.

Concatenating Reed-Solomon codes with Reed-Muller or other algebraic codes, and transmitting via BPPM for erasure correction greatly increased the level of protection on the channel, although this technique resulted in decreased coding efficiency. Interleaving the symbols prior to the inner coding step at a depth of 1 MB did not produce

an appreciable increase in performance, although the combination of outer and inner codes provided a significant increase over the inner code alone.

Transmission using spatial diversity and repetition alone (OOK) provided similar levels of protection as did the ***RM***-based concatenated codes. However, the efficiency of this combination was significantly reduced. Thus, if a Reed-Muller code is available, overall performance is maximized by using a concatenated ***RM***-based code and BPPM. Of note, this result is predicted by the recent theoretical work of Kudekar et al. (2017).

Pr(Outage) was the most significant parameter affecting performance among all the codes tested. Pr(Outage) could be changed by varying the threshold level i_T. This reduced the $\Pr_{fade}$ while at the same time increasing the $\Pr_{FA}$. If a particular system has SNR to spare, it may thus be traded for protection against deep fades. E_b did not vary enough between the coding schemes tested to emerge as a significant parameter, although a possible lower bound was identified using the testing parameters. The overall results indicated that Pr(Outage) > 10^{-4} resulted in an unusable channel.

The original, unmodified QR scheme was determined to be unsatisfactory given the channel model used throughout this thesis. This is because the QR scheme exposes all bits equally to the effects of fading. Since QR uses Reed-Solomon encoding over $\mathbb{F}_{2^8}$, which operates on 8-bit symbols, this transmission method creates maximum symbol exposure to fading effects. Should arrays large enough to support a QR pattern be feasible, much better results will be obtained using a symbol/laser pairing as with the high-rate codes tested.

B. RECOMMENDED ENCODING SCHEME

Based on the above results, an adaptive encoding scheme is recommended using the appropriate high-, mid- and low-rate codes tested for a given array size. To take advantage of the ***RM*** codes, array sizes that are powers of 2 are recommended.

For these experiments, the high-rate codes were designed to have a threshold of three, which can only correct for two or fewer lasers in a simultaneous fade. This threshold may be changed by choosing a higher level of error correction for the underlying Reed-Solomon code at a given size. The depth of consecutive symbols can thus be decreased to

allow for more than two lasers in a simultaneous fade. For example, at the 32-laser array size, choosing ***RS***(64, 32) instead of ***RS***(128, 16) would allow for up to eight lasers to be faded, setting the threshold $t = 9$ rather than $t = 3$. At $Pr_{fade} = 0.015$, this yields a Pr(Outage) $= 7.90\times10^{-10}$ as opposed to Pr(Outage) $= 1.21\times10^{-2}$. As detailed in the summary following Experiments 3 and 4, this will be a usable channel—although the efficiency would be reduced from 0.875 to 0.5.

For the medium-rate codes, the success of the ***NR*** and $\boldsymbol{G}_{24}$ codes at low to moderate turbulence indicate that the use of a second-order ***RM*** code is likely worthwhile as an inner code for an array size of 32 or larger at low to moderate turbulence levels. Otherwise, for an array size of 16, the ***NR*** code is recommended; at the 8-laser size, the 1/2-rate ***RM***(1,3) code is recommended. Since the 1 MB interleaver had no significant effect on performance, it may be removed.

Given sufficiently high SNR, the use of concatenated ***RM***-based codes incorporating BPPM is recommended over a repetition scheme. As detailed in Experiment 3, error correction was equivalent, and the efficiency of the concatenated codes was greater by a factor of two or more, depending on the array size. However, this conclusion only holds true in cases limited by fading, not by noise. The repetition code should not be abandoned if the engineering design allows the technique of aperture averaging to be used at the outer limits of workable range. This technique averages the overall current induced on all apertures (i.e., receivers) during each bit-window. Thus, it allows for system SNR to be increased if the SNR of the individual paired transmitters/receivers is not sufficient to allow for the more advanced encoding schemes discussed above. Also, repetition schemes may be useful during the initial acquisition phase, before the receiver and transmitter have successfully locked on to each other.

A basic LFSR was used to stand in for the encryption step in Layer 1, essentially serving as link encryption. While it may be tempting to take advantage of the LPD/LPI nature of FSO communications and therefore push the encryption step farther up the stack (e.g., end-to-end encryption), care must be taken to ensure that a FSO link is compatible with other tactical wireless links. Since tactical RF transmissions typically use link

encryption, use of link encryption protocols is recommended for any proposed tactical FSO communications system to maintain interoperability.

C. RECOMMENDATIONS FOR FUTURE RESEARCH

Further study should be conducted using prototype models for live atmospheric testing. The results obtained should be used to inform a number of design decisions, including optimal size of laser array, modulation scheme, coding scheme, and threshold values. Field programmable gate arrays (FPGAs) are recommended for this level of prototyping since they offer much of the flexibility of software implementation along with the speed and optimization of hardware implementation. Numerous optimizations can be made while incorporating the algorithms tested in this thesis; for previous work done with FPGAs and Golay codes see Sari (1997). Holmes, Reed, Truong, and Yin (1988) provide another algorithm for simplified error correction decoding of the $\boldsymbol{G}_{24}$ codes which may be extended to erasure correction using the methods described in this thesis.

Other improvements can be made by relaxing the hard-decision requirement and implementing various forms of soft-decision decoding. A number of fast soft-decoding algorithms for the Reed-Muller codes are described in Ashikhmin and Litsyn (1995). Convolutional codes were not considered by this research but may prove to be an attractive variable-rate option for the outer code instead of the ***RS***(255,32) code. LDPC codes may also be considered for the outer code.

Algorithmic complexity was not specifically addressed in this thesis, although simpler approaches were favored over more complex ones for practical reasons. Future prototyping should take advantage of existing optimizations for several of the codes used. Adoul (1987) provides optimizations for decoding the ***NR*** code. Use of the Fast Hadamard Transform—specifically using hardware implementation such as the Green Machine algorithm—may improve the decoding runtime of the codes which rely on the Hadamard Transform, which include the ***NR*** and all ***RM*** codes. MacWilliams and Sloane (2006) provide descriptions and logical diagrams for the Green Machine, and Blahut (2003) provides numerous diagrams for other implementations of decoding algorithms.

Regarding the optimal size, since the Rytov variance is proportional to nearly the square of the distance (specifically, $d^{11/6}$), shorter distances under the same atmospheric conditions will yield a reduced χ^2. Thus, the smaller array sizes may be more suitable to shorter anticipated link lengths. For example, while the 8-laser array size did not exhibit acceptable performance levels at high turbulence levels, for a link less than 1000 m such turbulence levels may be so unlikely as to be negligible in the design phase. Moreover, SNR may be high enough on such a short link as to allow an extremely low i_T, driving down the Pr_{fade} even further. Such theoretical tradeoffs are areas which need to be tested by prototype systems under actual atmospheric channel conditions.

While the 1 MB interleaver was found to have no significant impact on performance, interleaving at a greater depth (10-100 MB) may be useful in low to moderate turbulence cases where the channel is degraded but not in an outage. Interleaving may then help in overcoming the effects of noise (i.e., pushing the stable region to the left in terms of SNR). This will come at the price of latency, memory and possibly channel overhead if a padding scheme is used to fill the interleaver when data demands are low.

The determination of channel state information was not addressed specifically in this thesis, although it will clearly be an important design factor in the recommended adaptive scheme. Since the mid- and high-rate codes use ***RS*** codes in the final decoding step, statistics from these decoders may be used in place of dedicated pilot tones. Repeated failures of ***RS*** blocks could be used to determine a switch to a lower rate code. For the low-rate repetition codes, statistics may similarly be gathered by evaluating the percentage of modules deemed to be in an outage during a transmission window. If this percentage is low enough, the code rate may then be stepped up to a mid- or high-rate code.

Alternatively, channel state information could be gathered by tracking fades on individual laser modules, determined by the reception of a large number of consecutive detections below i_T. Coding rate decisions could then be made when the average number of modules in a fade reaches some threshold value chosen below the error/erasure capacity of a given code.

Layer 2 protocols could be developed to take advantage of the ***RS*** statistics and coordinate retransmission of ***RS*** blocks prior to higher layer (eg, TCP) detection of packet failures. This may help obviate the concerns identified by Chan (2006) in which TCP requests significantly affected throughput.

While the use cases that have driven this research primarily envision communications entirely within the atmosphere, the fading mitigation techniques may be adapted for surface to space communications. Here, highly sensitive (photon-counting) receivers may be assumed, and geometric losses due to beam spreading will be extreme. Given sufficiently powerful individual lasers (i.e., SNR great enough that repetition is not needed), use of a *N*-ary PPM or time-gated scheme may be considered in conjunction with any of the medium-rate codes tested (see Djordjevic et al. (2006) for a discussion of a similar modulation scheme, although one which does not use the spatial dimension as proposed here). Such a scheme would extend the symbol window by a factor twice the size of the array used—i.e., if the optical switching frequency were 100 MHz, an array size of 8 lasers would yield a symbol-window T_s = 160 ns. Each laser would be given its own time-slot of 20 ns in which to transmit an on/off pair indicating a binary 1 or 0, coding for erasure much as the BPPM used throughout this thesis. A single receiver aperture could be used since laser modules would be distinguished by timing. Such an arrangement would take advantage of the relatively independent paths taken by the various laser beams through the atmosphere (mitigating turbulence) while reducing the power requirements of a repetition scheme.

D. CONCLUSION

FSO communications over the MIMO atmospheric channel may be significantly improved by incorporating FEC techniques. This thesis identified and tested a number of different techniques appropriate for different levels of fading and noise. By combining spatial and temporal coding techniques, an increased level of efficiency and effectiveness was demonstrated over previous coding schemes. Continued work in this area is indicated to develop the high-capacity LPI/LPD communications required by Joint Force future employment concepts.

APPENDIX A. CHANNEL PARAMETERS USED IN SIMULATION

Irradiance distributions (PDF and CDF) are displayed in Figures 32–34 for the five Rytov variances used in testing (0.04, 0.2, 1, 5 and 25).

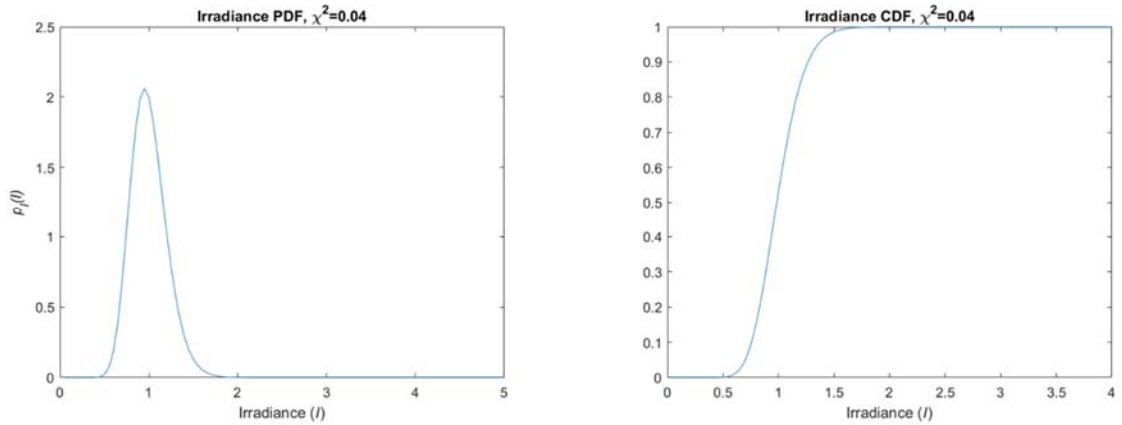

Figure 32. Probability and Cumulative Density Functions, Rytov Variance $\chi^2 = 0.04$

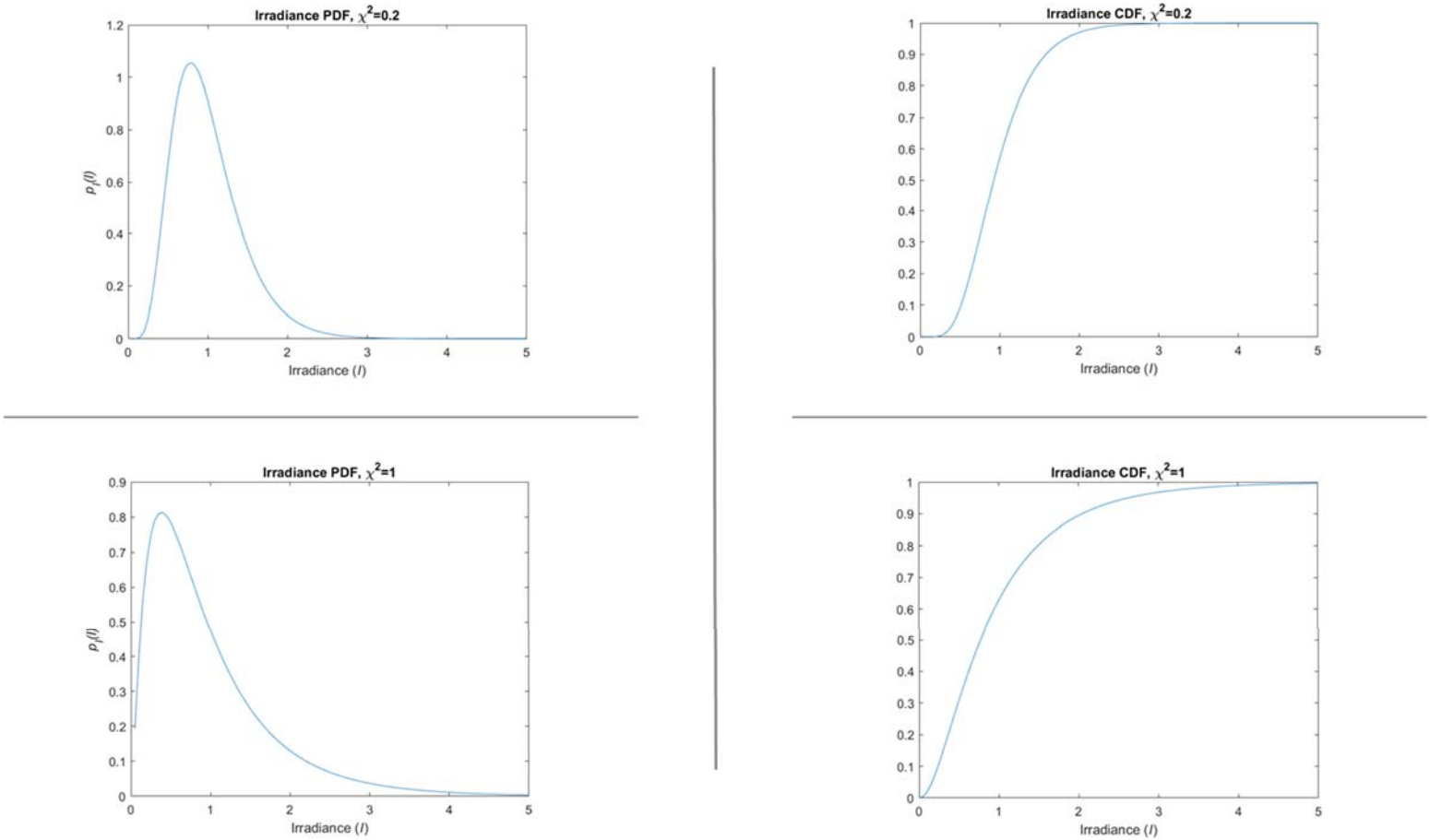

Figure 33. Probability and Cumulative Density Functions, Rytov Variance χ^2 = 0.2 and 1

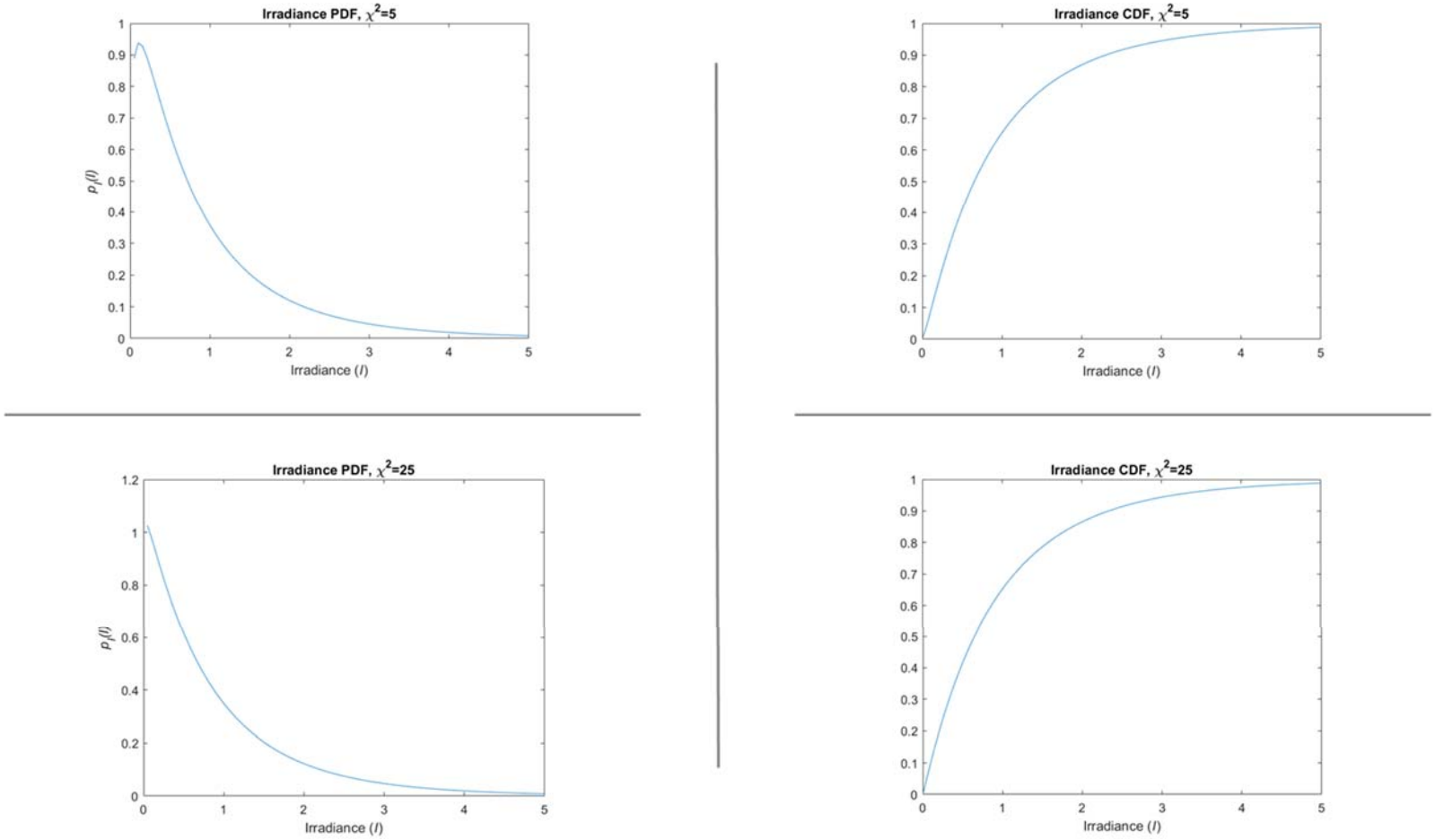

Figure 34. Probability and Cumulative Density Functions, Rytov Variance χ^2 = 5 and 25

Channel probabilities describing the eight channel states used in testing are summarized in Tables 17–24 and graphed in Figures 35–42.

Table 17. Channel Probabilities, $\chi^2 = 0.04$, $i_T = 0.5$

SNR (dB)	Pr_{fade}	Pr_{FA}	$Pr_{D\|fade}$	Pr_{miss}
0	0.00067468	0.30854	0.30854	0.30854
5	0.00067468	0.18696	0.18696	0.18696
10	0.00067468	0.056923	0.056923	0.056923
15	0.00067468	0.002464	0.002464	0.002464
20	0.00067468	2.87 E-7	2.87 E-7	2.87 E-7
25	0.00067468	3.02E-19	3.02E-19	0
30	0.00067468	1.30E-56	1.30E-56	0
35	0.00067468	3.03E-174	3.03E-174	0
40	0.00067468	0	0	0
45	0.00067468	0	0	0
50	0.00067468	0	0	0

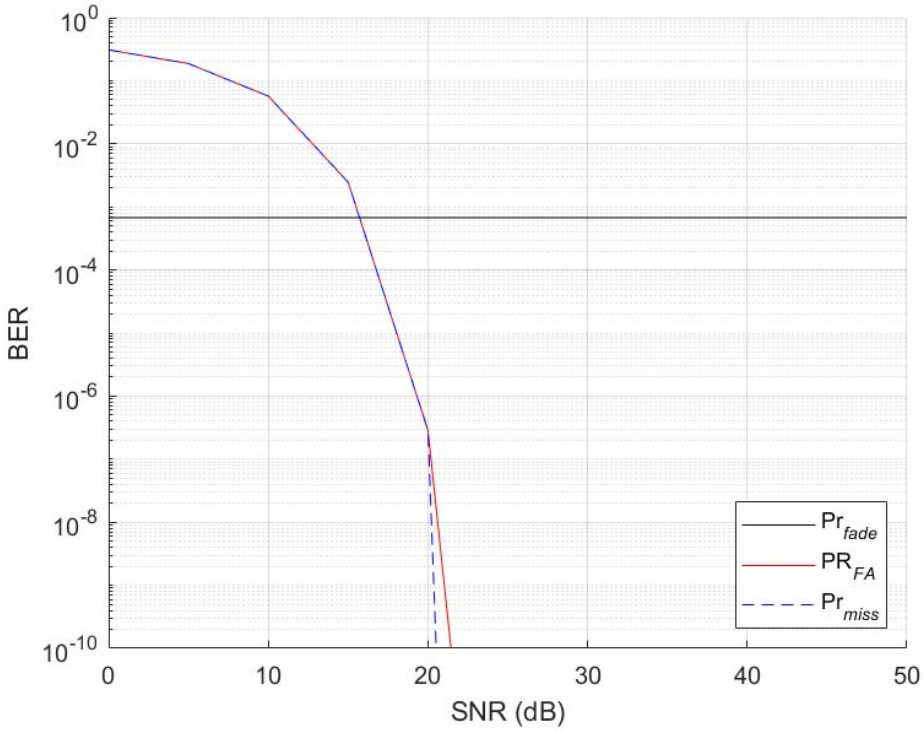

Figure 35. Channel Probabilities, $\chi^2 = 0.04$, $i_T = 0.5$

Table 18. Channel Probabilities, $\chi^2 = 0.2$, $i_T = 0.25$

SNR (dB)	Pr_{fade}	Pr_{FA}	$Pr_{D\|fade}$	Pr_{miss}
0	0.0034977	0.40129	0.40129	0.22663
5	0.0034977	0.32832	0.32832	0.09115
10	0.0034977	0.2146	0.2146	0.008853
15	0.0034977	0.079884	0.079884	1.23 E-5
20	0.0034977	0.0062097	0.0062097	3.19E-14
25	0.0034977	4.38E-6	4.38 E-6	0
30	0.0034977	1.33E-15	1.33E-15	0
35	0.0034977	3.41E-45	3.41E-45	0
40	0.0034977	3.06E-138	3.06E-138	0
45	0.0034977	0	0	0
50	0.0034977	0	0	0

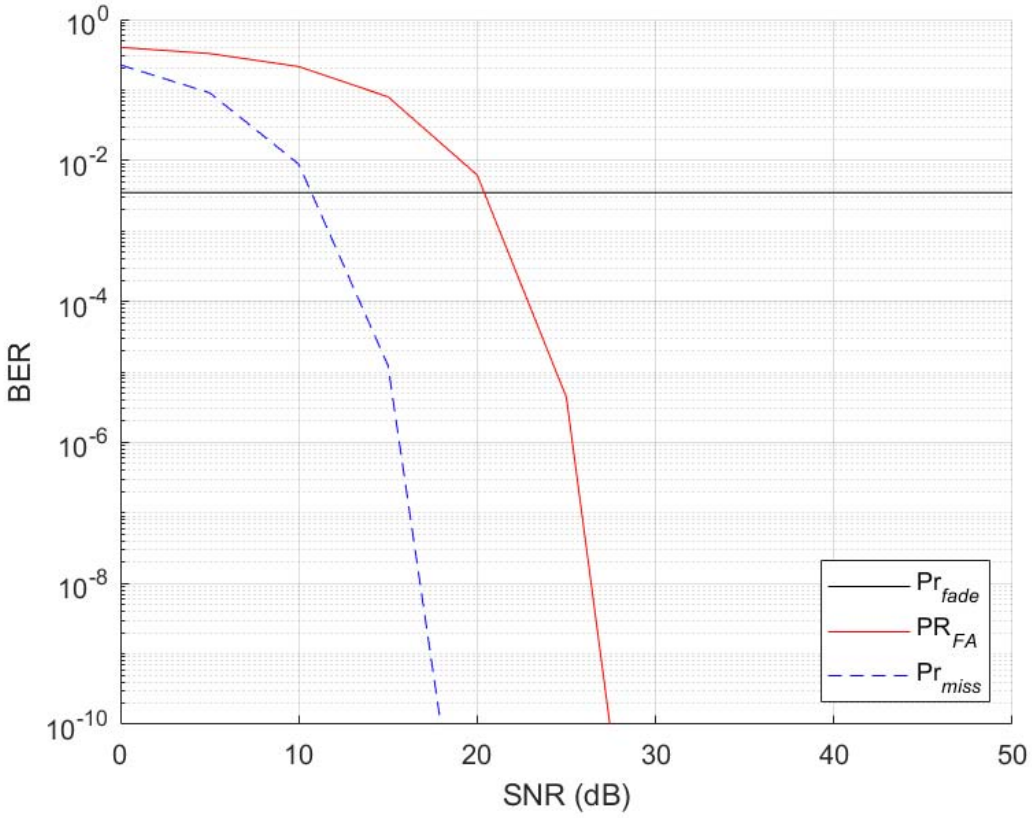

Figure 36. Channel Probabilities, $\chi^2 = 0.2$, $i_T = 0.25$

Table 19. Channel Probabilities, $\chi^2 = 0.2$, $i_T = 0.33$

SNR (dB)	Pr_{fade}	Pr_{FA}	$Pr_{D\|fade}$	Pr_{miss}
0	0.015002	0.3707	0.3707	0.25143
5	0.015002	0.27866	0.27866	0.11674
10	0.015002	0.14835	0.14835	0.017057
15	0.015002	0.031746	0.031746	8.24×105
20	0.015002	0.00048342	0.00048342	1.04E-11
25	0.015002	2.20 E-9	2.20 E-9	0
30	0.015002	8.53E-26	8.53E-26	0
35	0.015002	3.56E-77	3.56E-77	0
40	0.015002	4.06E-239	4.06E-239	0
45	0.015002	0	0	0
50	0.015002	0	0	0

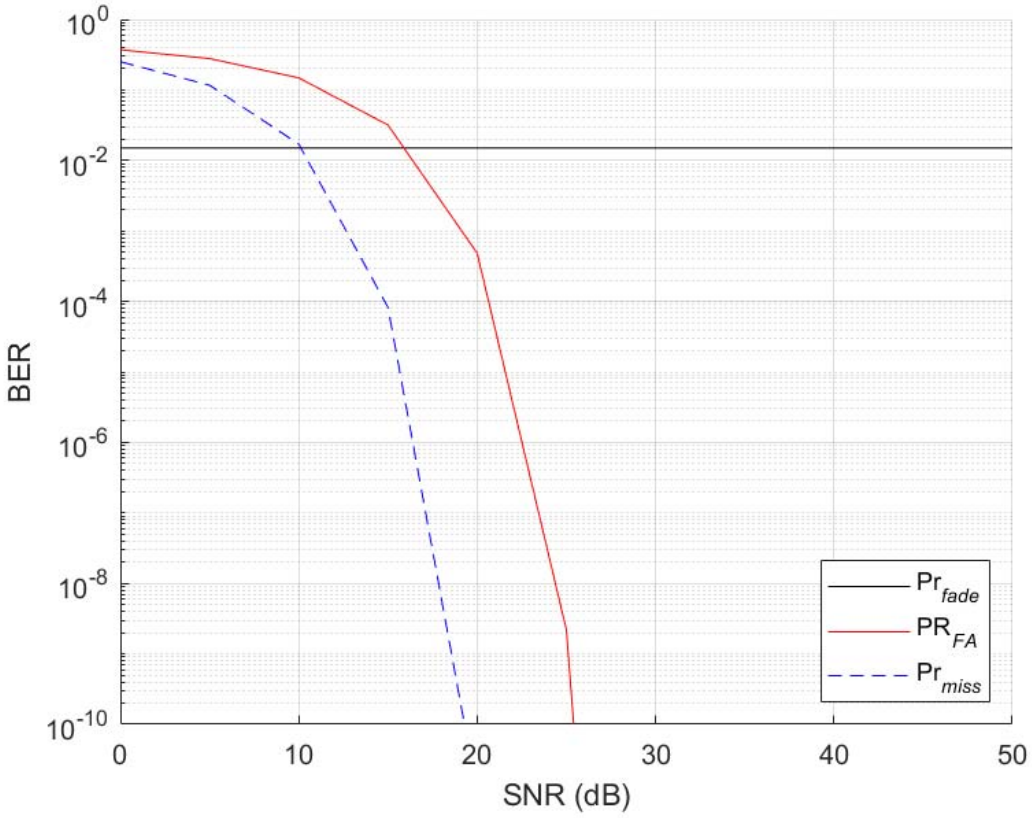

Figure 37. Channel Probabilities, $\chi^2 = 0.2$, $i_T = 0.33$

Table 20. Channel Probabilities, $\chi^2 = 1$, $i_T = 0.125$

SNR (dB)	Pr_{fade}	Pr_{FA}	$Pr_{D\backslash fade}$	Pr_{miss}
0	0.030532	0.45026	0.45026	0.19079
5	0.030532	0.41205	0.41205	0.059855
10	0.030532	0.34632	0.34632	0.0028288
15	0.030532	0.24105	0.24105	4.32 E-07
20	0.030532	0.10565	0.10565	0
25	0.030532	0.013113	0.013113	0
30	0.030532	3.86 E-5	3.86 E-05	0
35	0.030532	1.04E-12	1.04E-12	0
40	0.030532	3.73E-36	3.73E-36	0
45	0.030532	9.11E-110	9.11E-110	0
50	0.030532	0	0	0

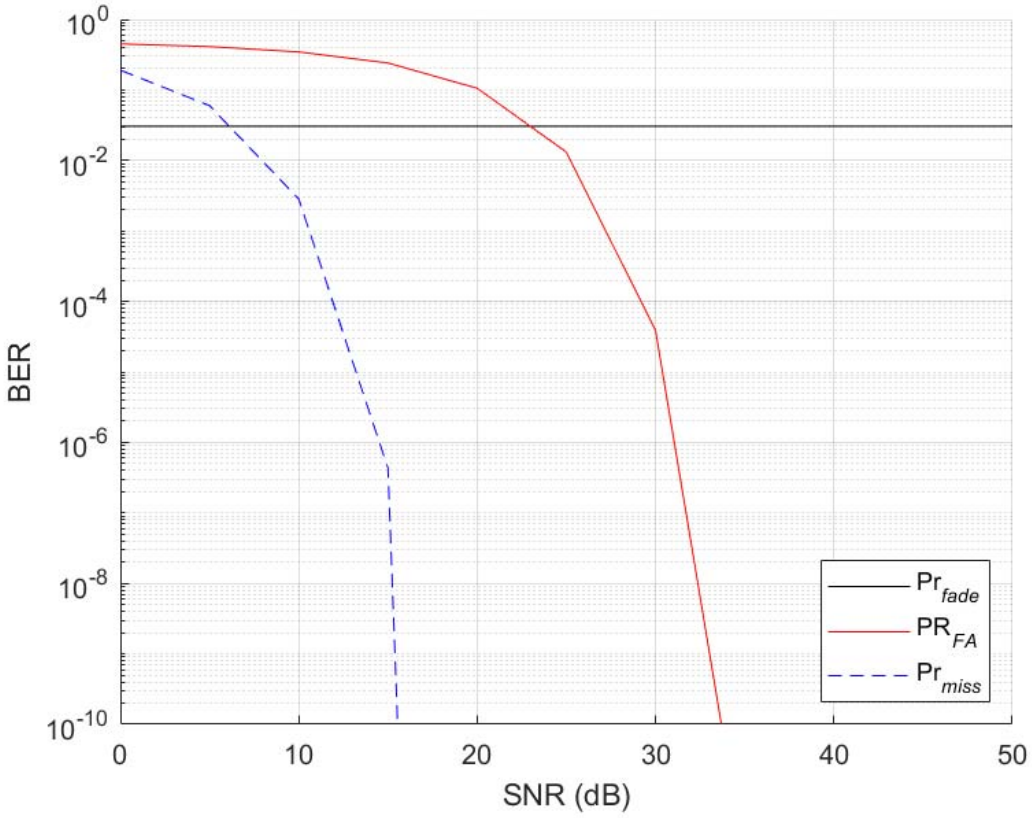

Figure 38. Channel Probabilities, $\chi^2 = 1$, $i_T = 0.125$

Table 21. Channel Probabilities, $\chi^2 = 1$, $i_T = 0.2$

SNR (dB)	Pr_{fade}	Pr_{FA}	$Pr_{D\|fade}$	Pr_{miss}
0	0.074877	0.42074	0.42074	0.21186
5	0.074877	0.36105	0.36105	0.077423
10	0.074877	0.26354	0.26354	0.005706
15	0.074877	0.13036	0.13036	3.42 E-06
20	0.074877	0.02275	0.02275	6.66E-16
25	0.074877	0.00018787	0.00018787	0
30	0.074877	1.27E-10	1.27E-10	0
35	0.074877	1.20E-29	1.20E-29	0
40	0.074877	2.75E-89	2.75E-89	0
45	0.074877	2.39E-277	2.39E-277	0
50	0.074877	0	0	0

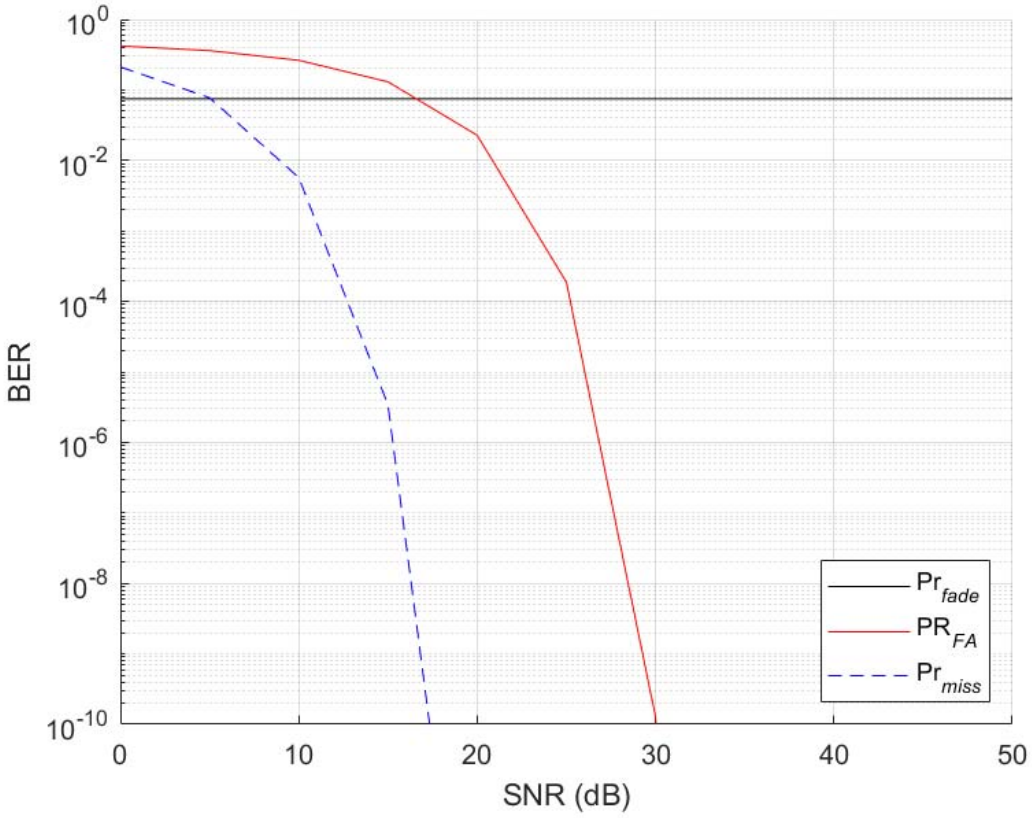

Figure 39. Channel Probabilities, $\chi^2 = 1$, $i_T = 0.2$

Table 22. Channel Probabilities, $\chi^2 = 5$, $i_T = 0.0625$

SNR (dB)	Pr_{fade}	Pr_{FA}	$Pr_{D\backslash fade}$	Pr_{miss}
0	0.049086	0.47508	0.47508	0.17425
5	0.049086	0.45575	0.45575	0.047744
10	0.049086	0.42166	0.42166	0.0015152
15	0.049086	0.36262	0.36262	6.75 E-08
20	0.049086	0.26599	0.26599	0
25	0.049086	0.13319	0.13319	0
30	0.049086	0.024053	0.024053	0
35	0.049086	0.00022018	0.00022018	0
40	0.049086	2.05E-10	2.05E-10	0
45	0.049086	5.35E-29	5.35E-29	0
50	0.049086	3.03E-87	3.03E-87	0

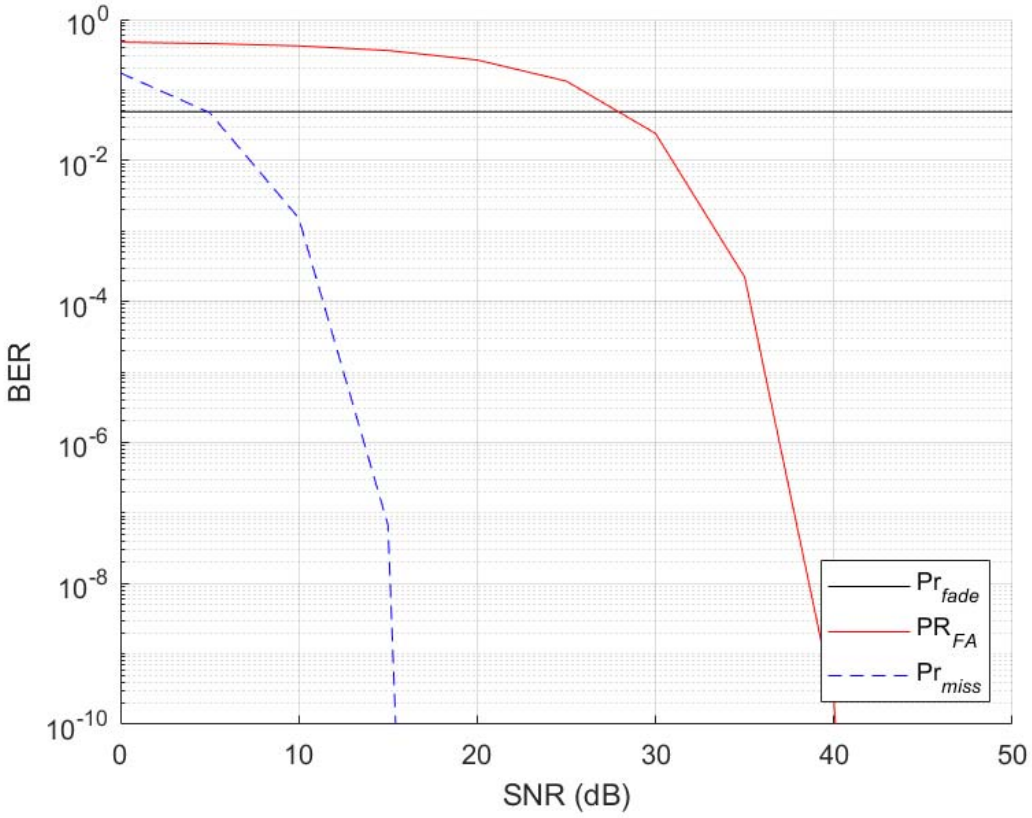

Figure 40. Channel Probabilities, $\chi^2 = 5$, $i_T = 0.0625$

Table 23. Channel Probabilities, $\chi^2 = 5$, $i_T = 0.125$

SNR (dB)	Pr_{fade}	Pr_{FA}	$Pr_{D\backslash fade}$	Pr_{miss}
0	0.10734	0.45026	0.45026	0.19079
5	0.10734	0.41205	0.41205	0.059855
10	0.10734	0.34632	0.34632	0.0028288
15	0.10734	0.24105	0.24105	4.32 E-07
20	0.10734	0.10565	0.10565	0
25	0.10734	0.013113	0.013113	0
30	0.10734	3.86 E-05	3.86 E-05	0
35	0.10734	1.04E-12	1.04E-12	0
40	0.10734	3.73E-36	3.73E-36	0
45	0.10734	9.11E-110	9.11E-110	0
50	0.10734	0	0	0

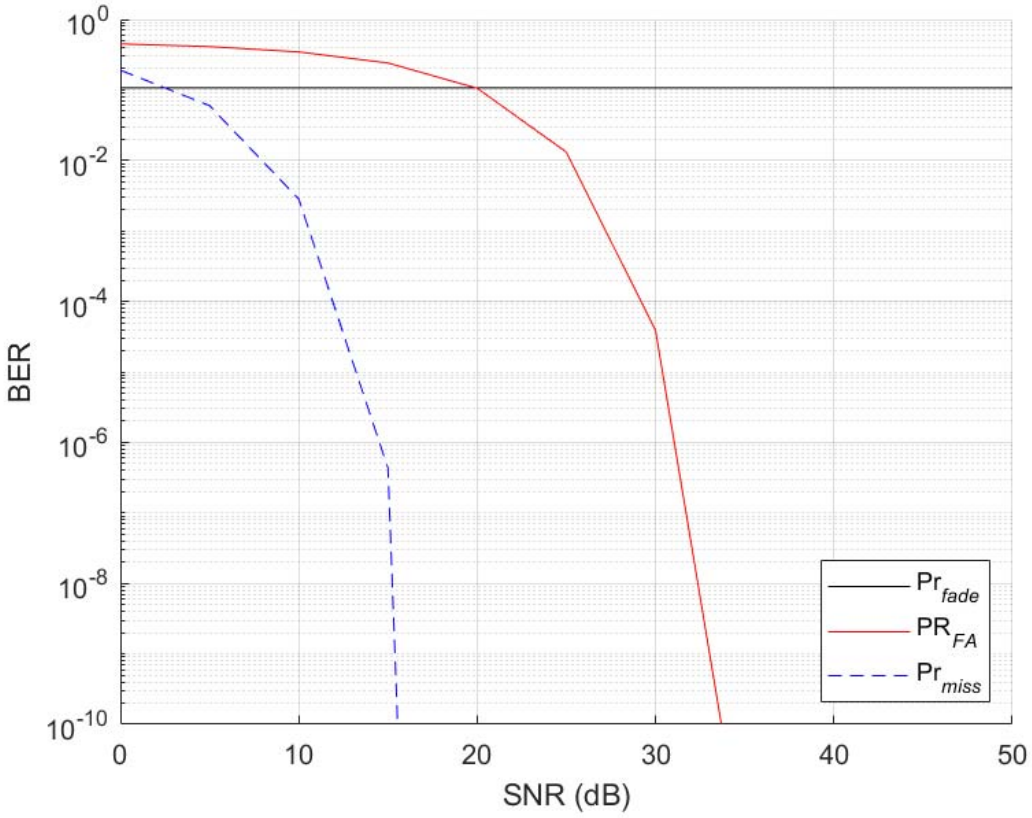

Figure 41. Channel Probabilities, $\chi^2 = 5$, $i_T = 0.125$

Table 24. Channel Probabilities, $\chi^2 = 25$, $i_T = 0.125$

SNR (dB)	Pr_{fade}	Pr_{FA}	$Pr_{D\backslash fade}$	Pr_{miss}
0	0.12579	0.45026	0.45026	0.19079
5	0.12579	0.41205	0.41205	0.059855
10	0.12579	0.34632	0.34632	0.0028288
15	0.12579	0.24105	0.24105	4.32 E-07
20	0.12579	0.10565	0.10565	0
25	0.12579	0.013113	0.013113	0
30	0.12579	3.86 E-05	3.86 E-05	0
35	0.12579	1.04E-12	1.04E-12	0
40	0.12579	3.73E-36	3.73E-36	0
45	0.12579	9.11E-110	9.11E-110	0
50	0.12579	0	0	0

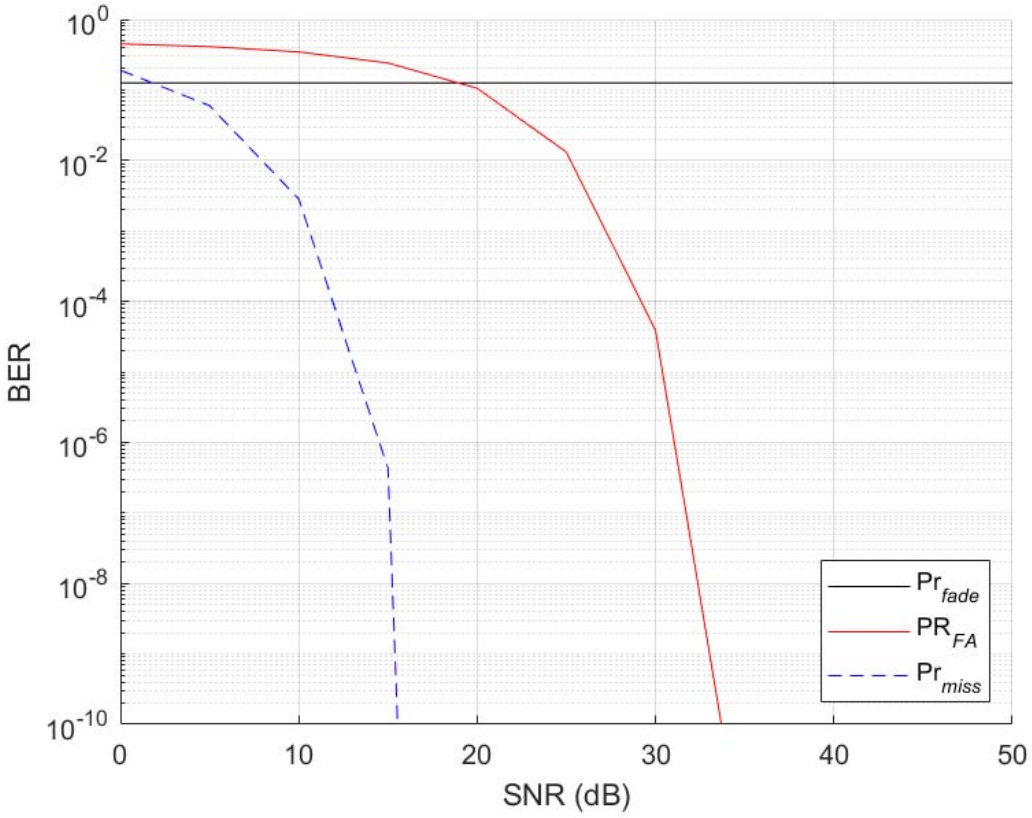

Figure 42. Channel Probabilities, $\chi^2 = 25$, $i_T = 0.125$

THIS PAGE INTENTIONALLY LEFT BLANK

APPENDIX B. SIMULATION RESULTS

Figures 43–78 display the results of each simulation. Results are organized by code, with the ***RS*** codes first, followed by the concatenated codes, and concluding with the repetition codes. Additional simulations performed with the concatenated codes (interleaver test, inner code only) are included following each concatenated code.

A. *RS*(64,32)

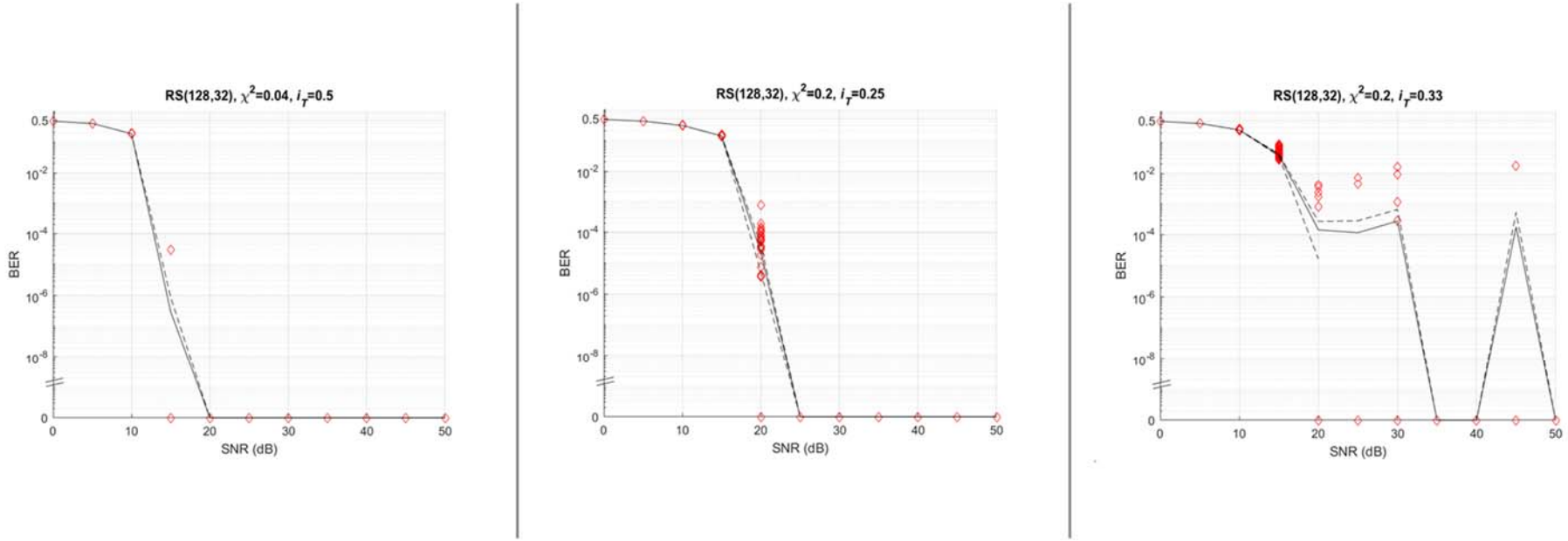

Figure 43. ***RS***(64,32) Simulation Results

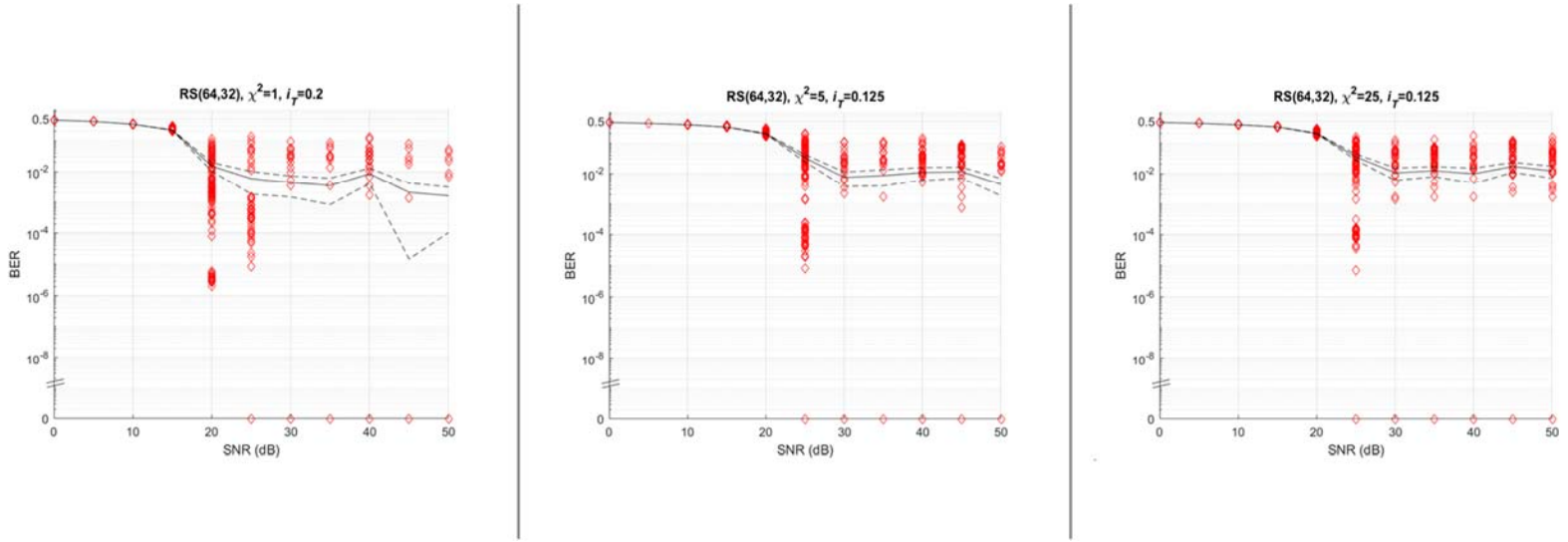

Figure 44. ***RS***(64,32) Simulation Results (Continued)

B. *RS*(128,32)

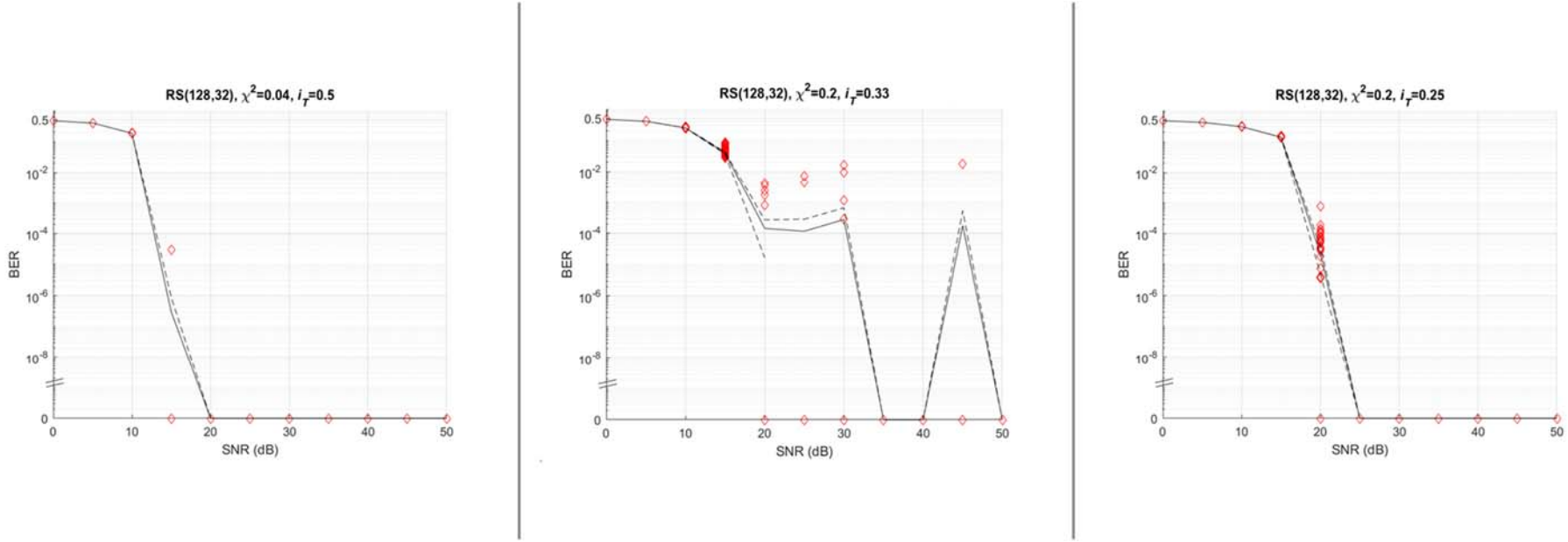

Figure 45. ***RS***(128,32) Simulation Results

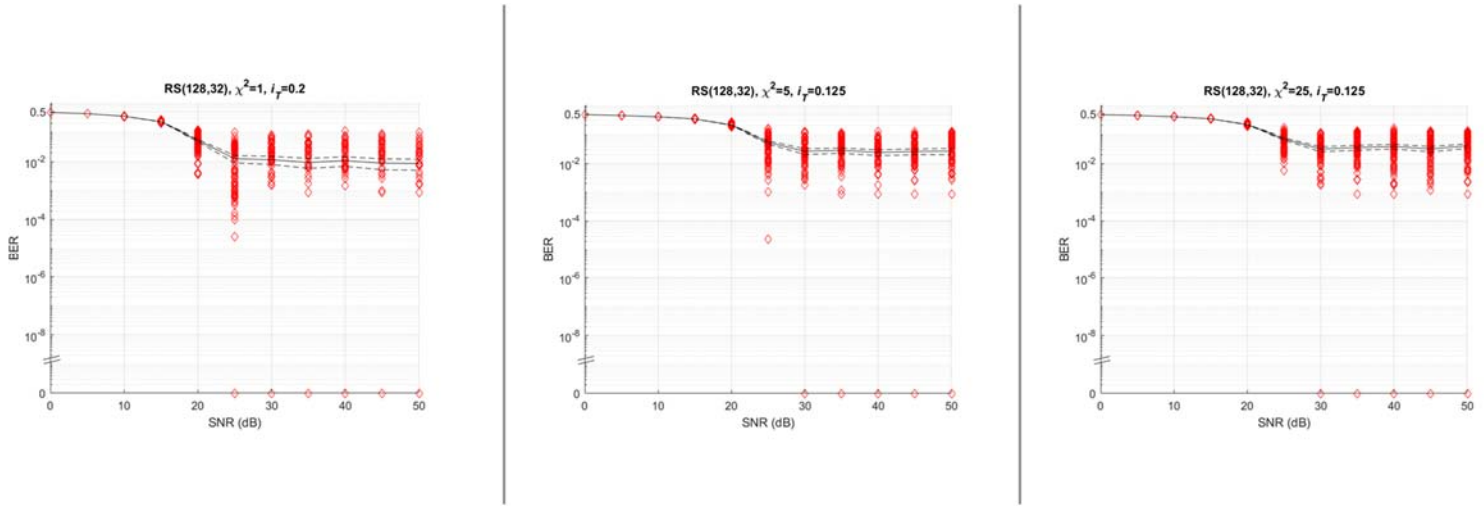

Figure 46. ***RS***(128,32) Simulation Results (Continued)

C. *RS*(120,20)

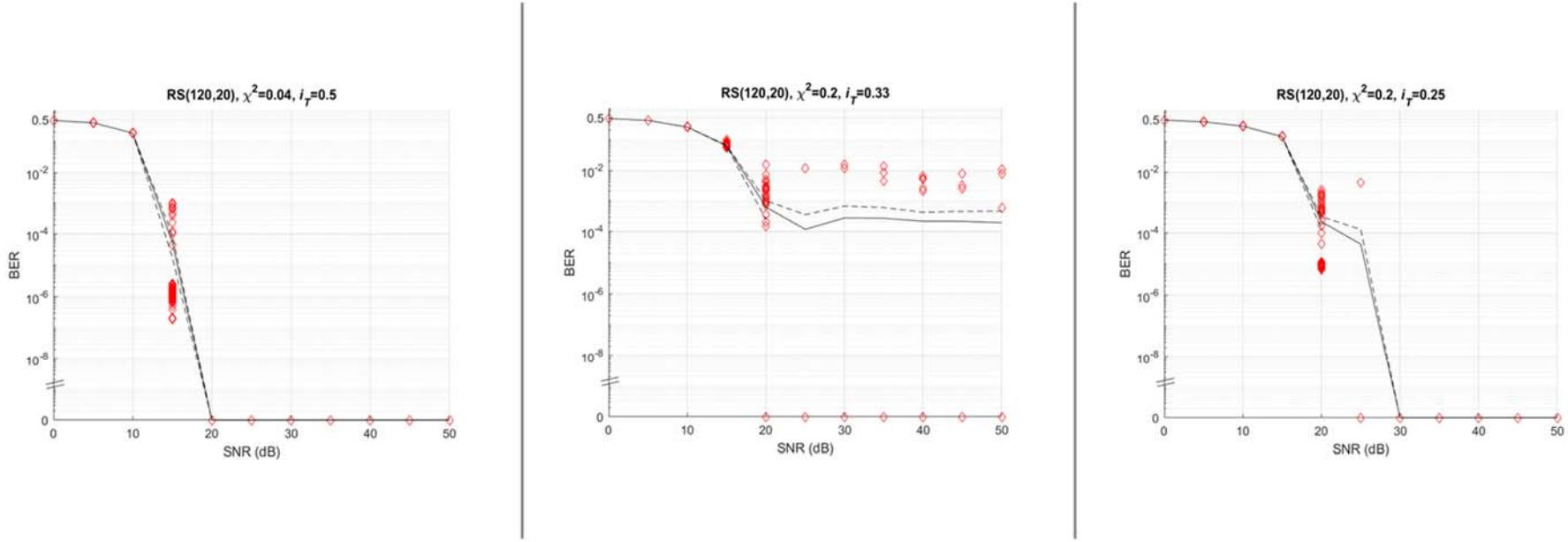

Figure 47. ***RS***(128,32) Simulation Results

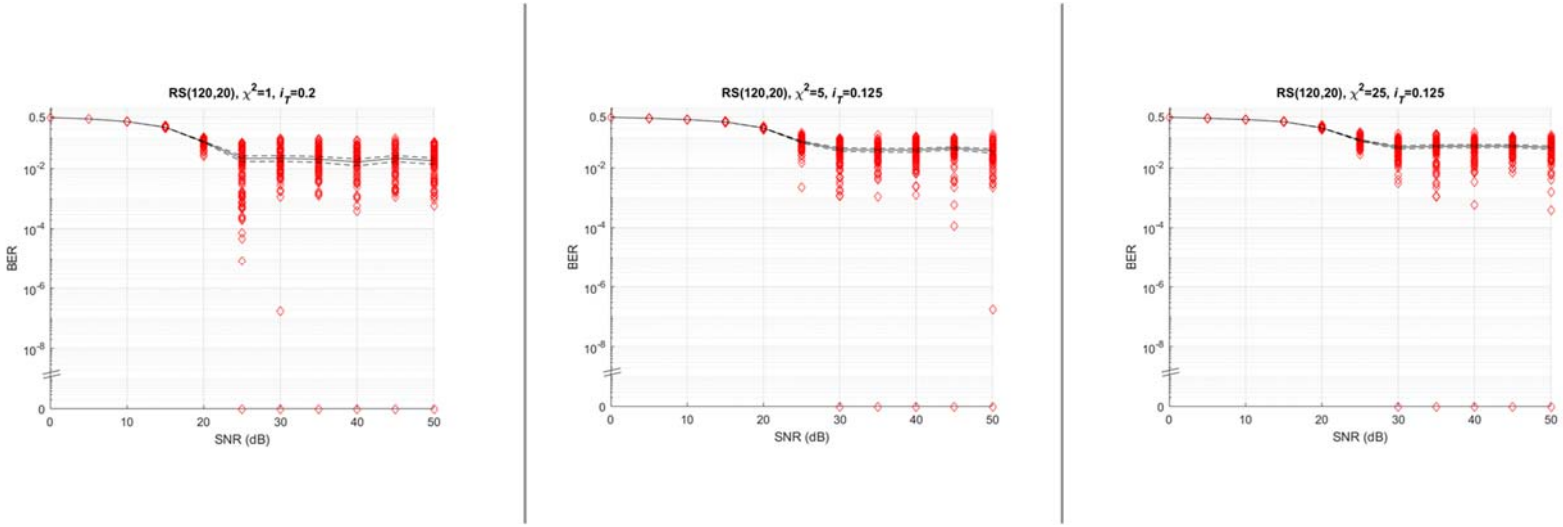

Figure 48. ***RS***(128,32) Simulation Results (Continued)

D. *RS*(128,16)

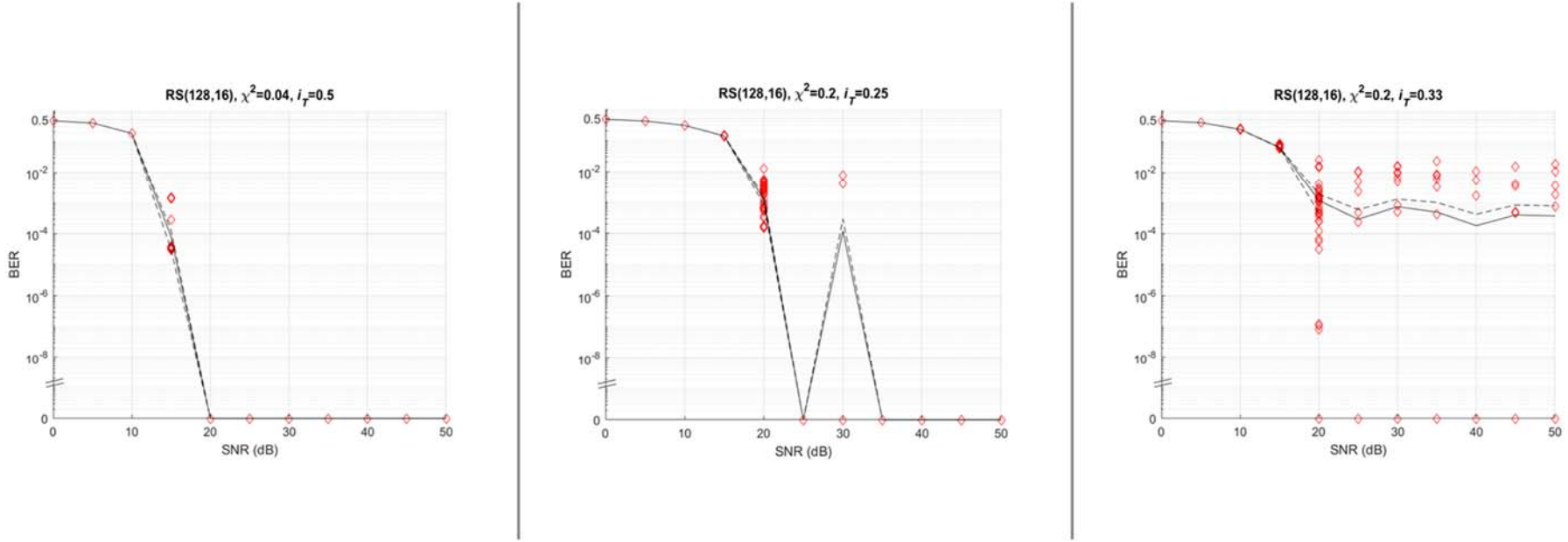

Figure 49. ***RS***(128,16) Simulation Results

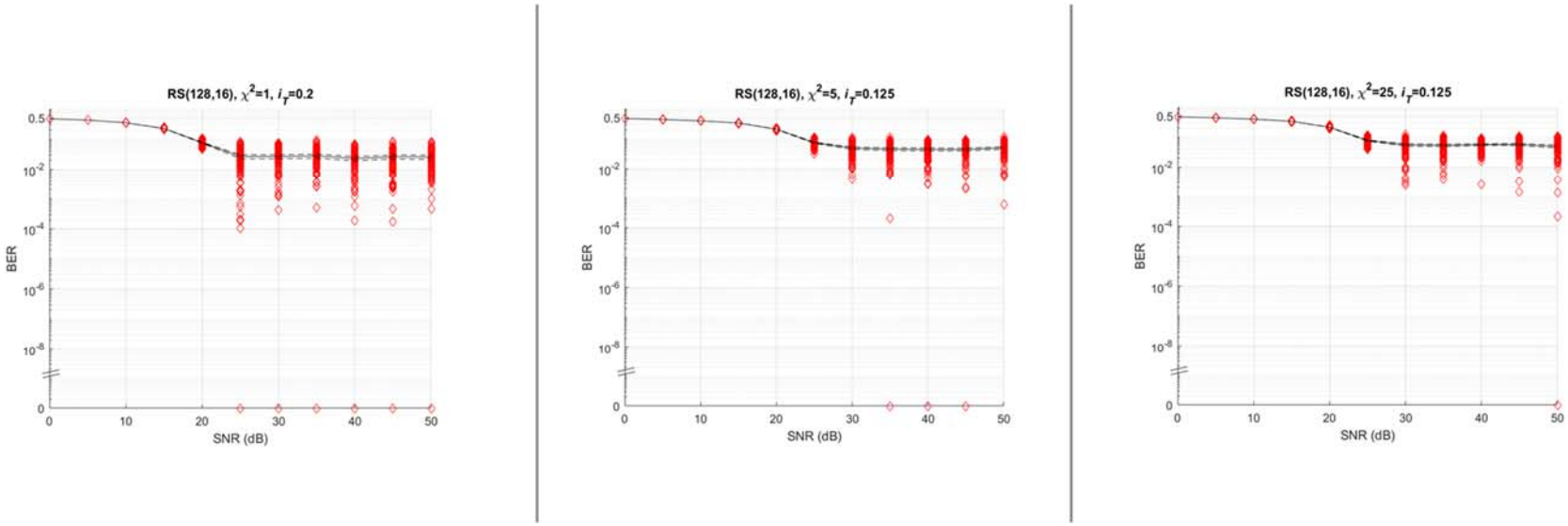

Figure 50. ***RS***(128,16) Simulation Results (Continued)

E. *RM*(1,3)/*RS*(255,32)

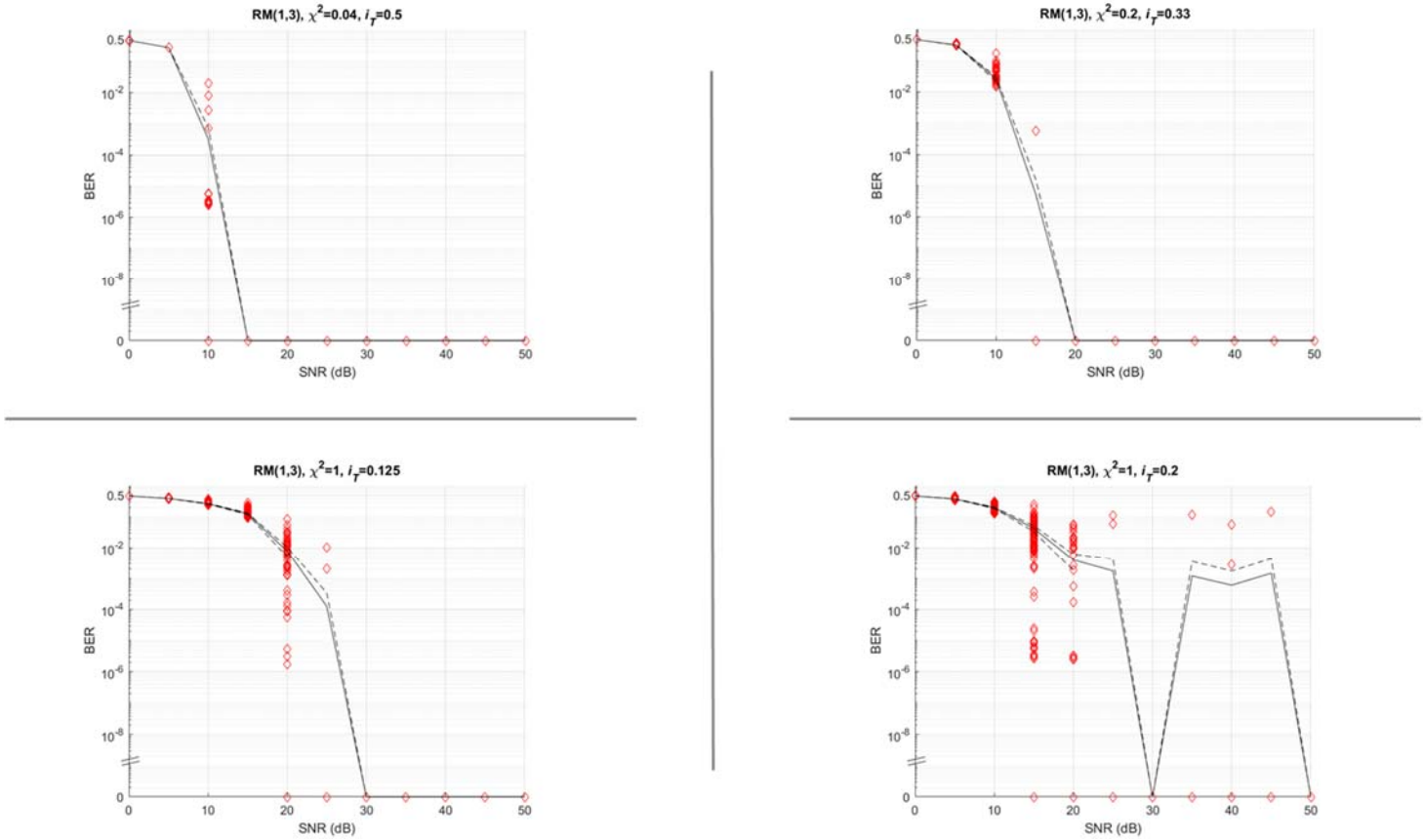

Figure 51. ***RM***(1,3)/***RS***(255,32) Simulation Results

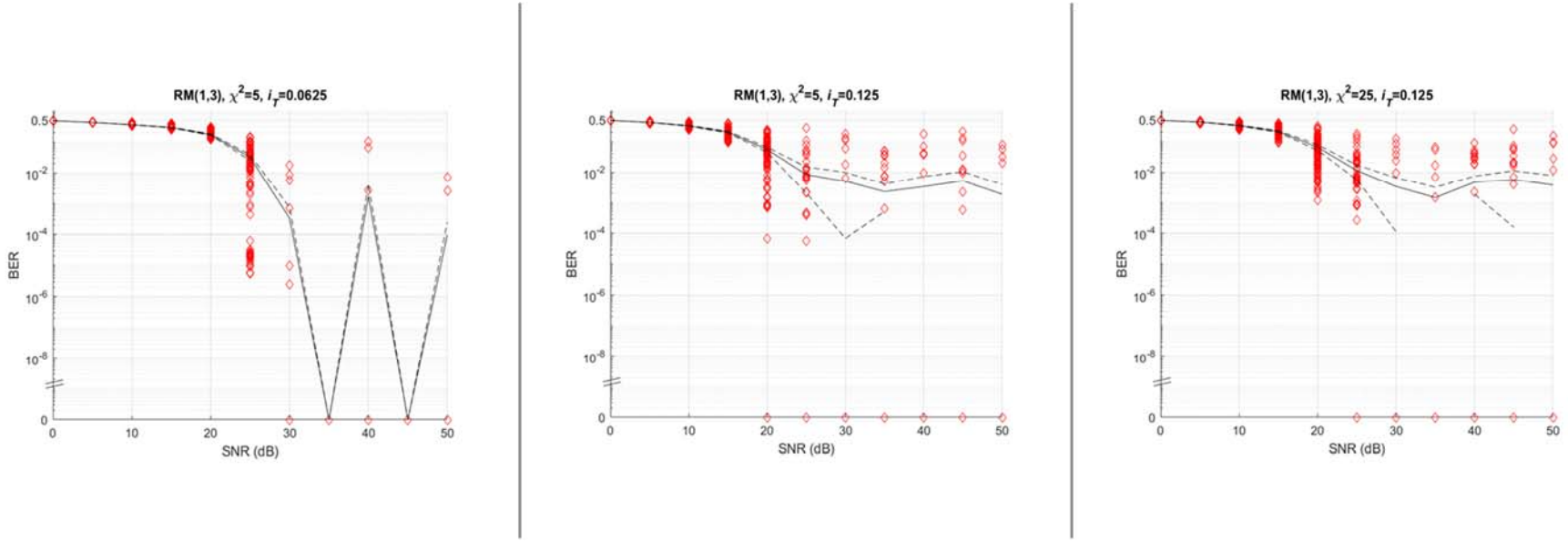

Figure 52. ***RM***(1,3)/***RS***(255,32) Simulation Results (Continued)

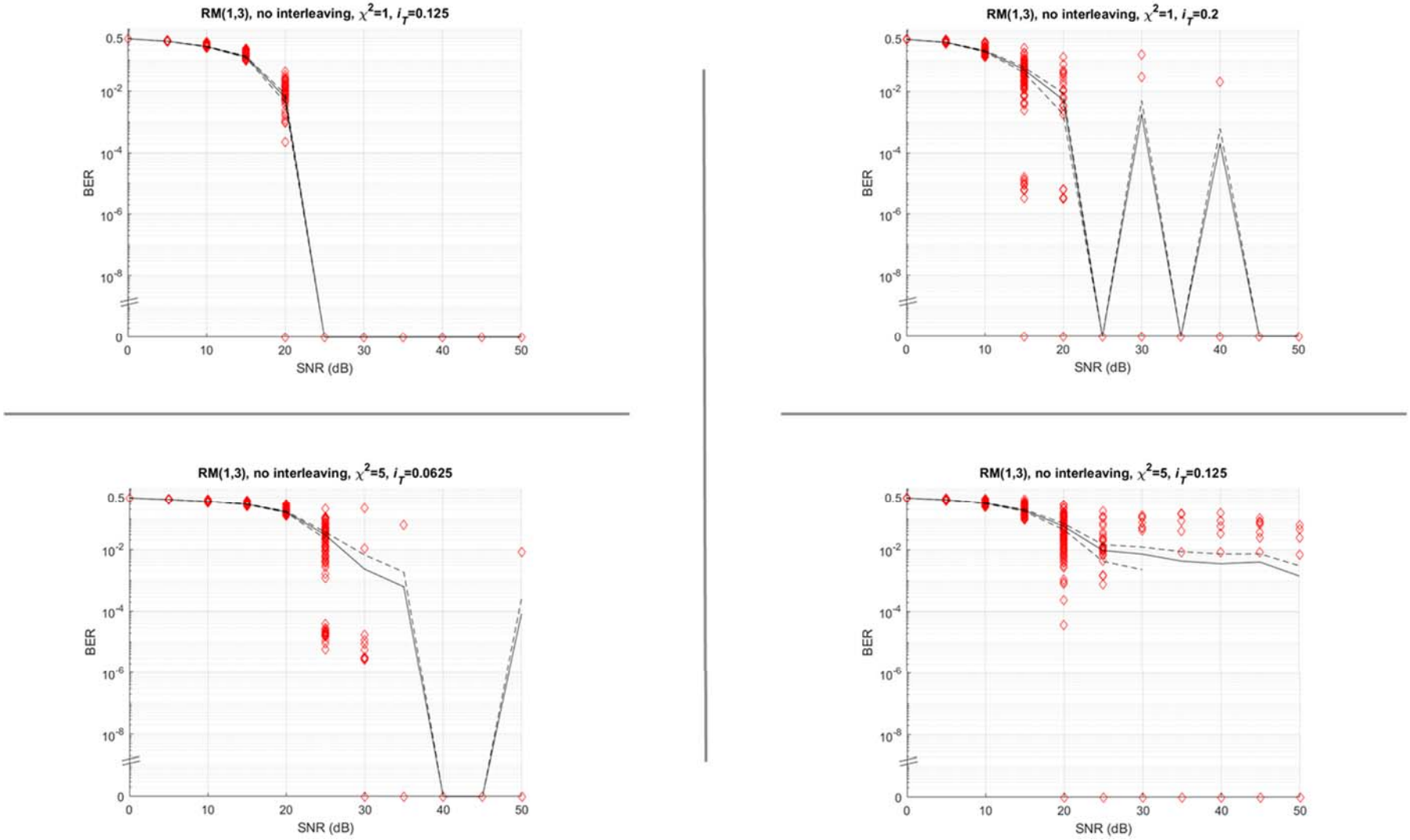

Figure 53. ***RM***(1,3)/***RS***(255,32) Simulation Results (No Interleaver)

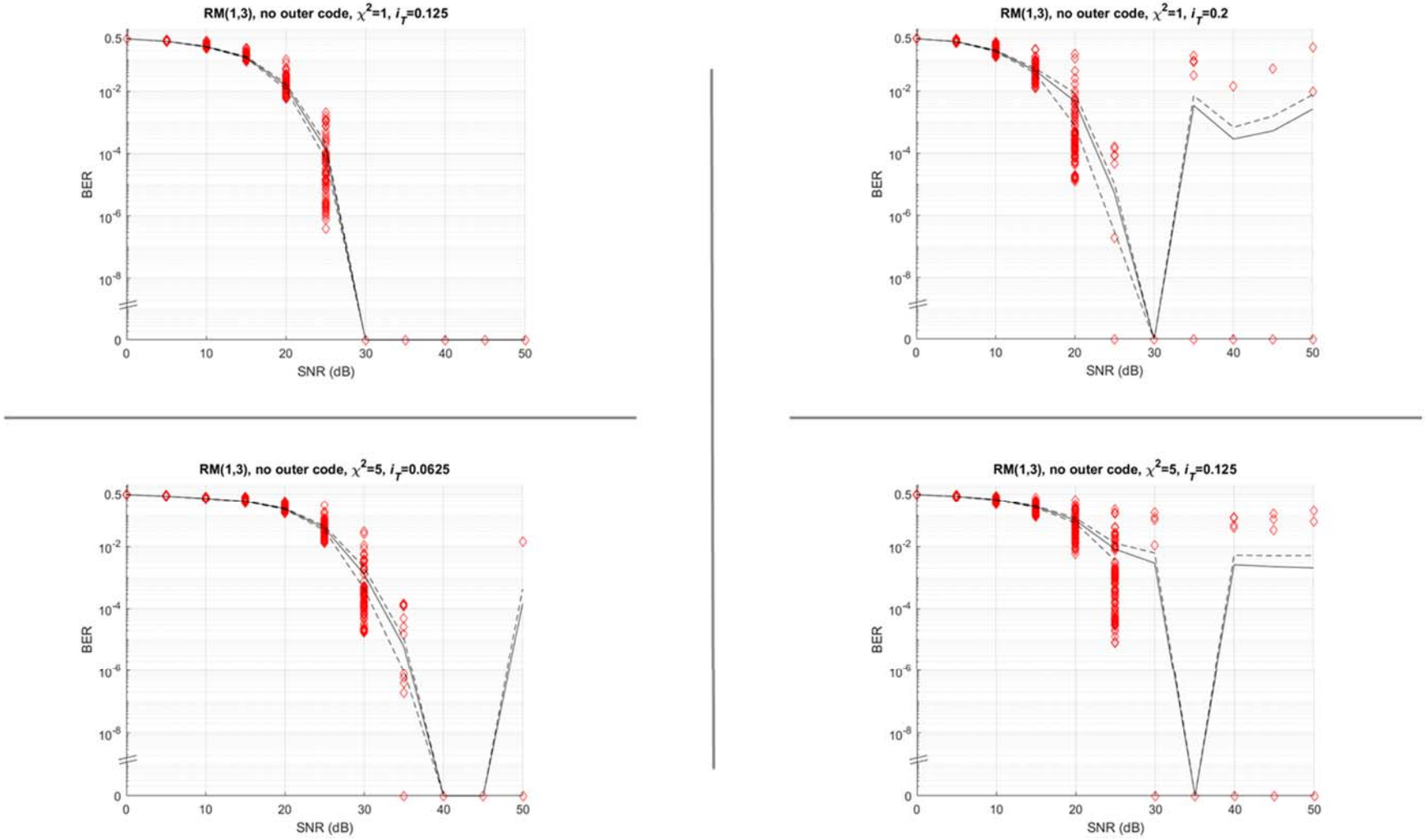

Figure 54. ***RM***(1,3) Simulation Results (No Outer Code)

F. *RM*(1,4)/*RS*(255,32)

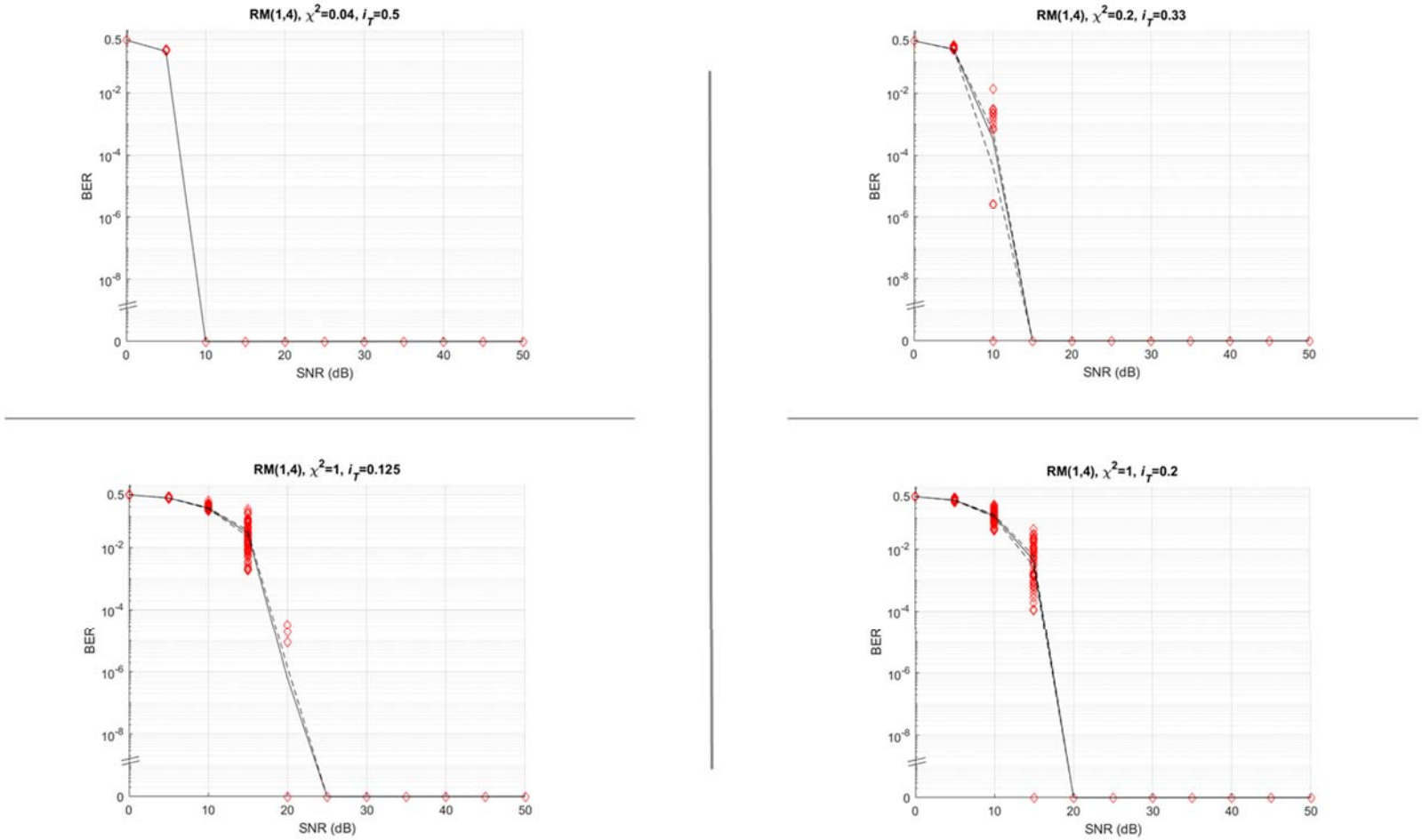

Figure 55. ***RM***(1,4)/***RS***(255,32) Simulation Results

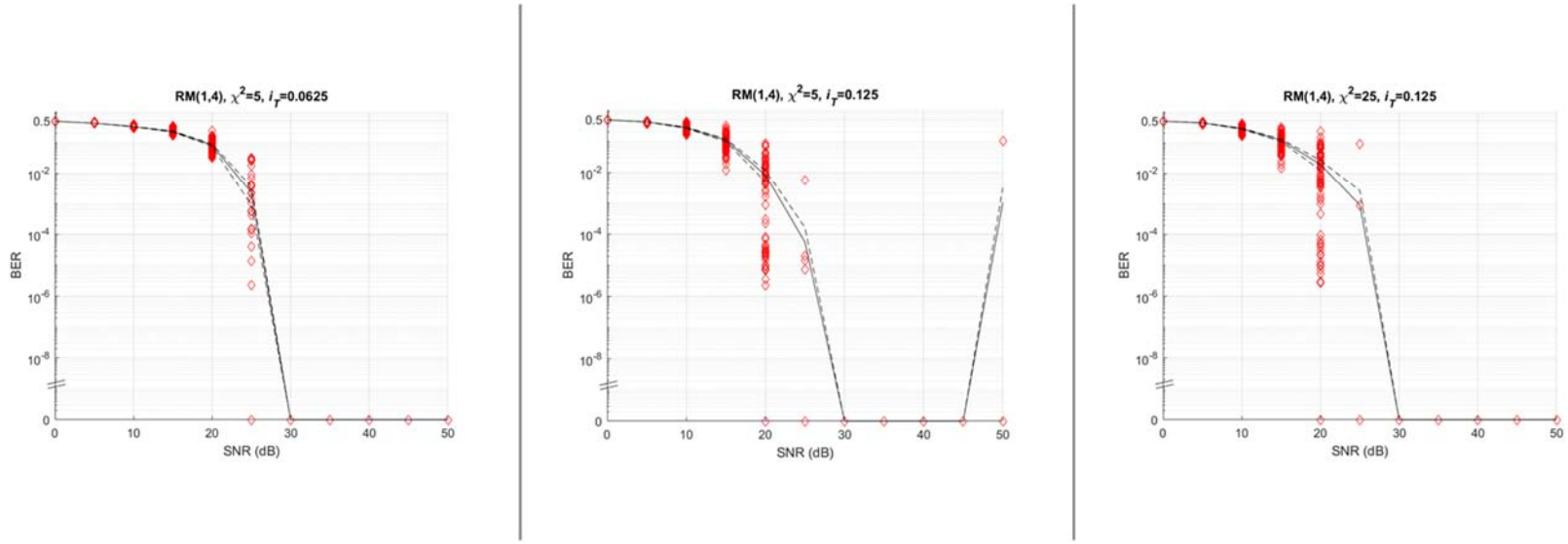

Figure 56. ***RM***(1,4)/***RS***(255,32) Simulation Results (Continued)

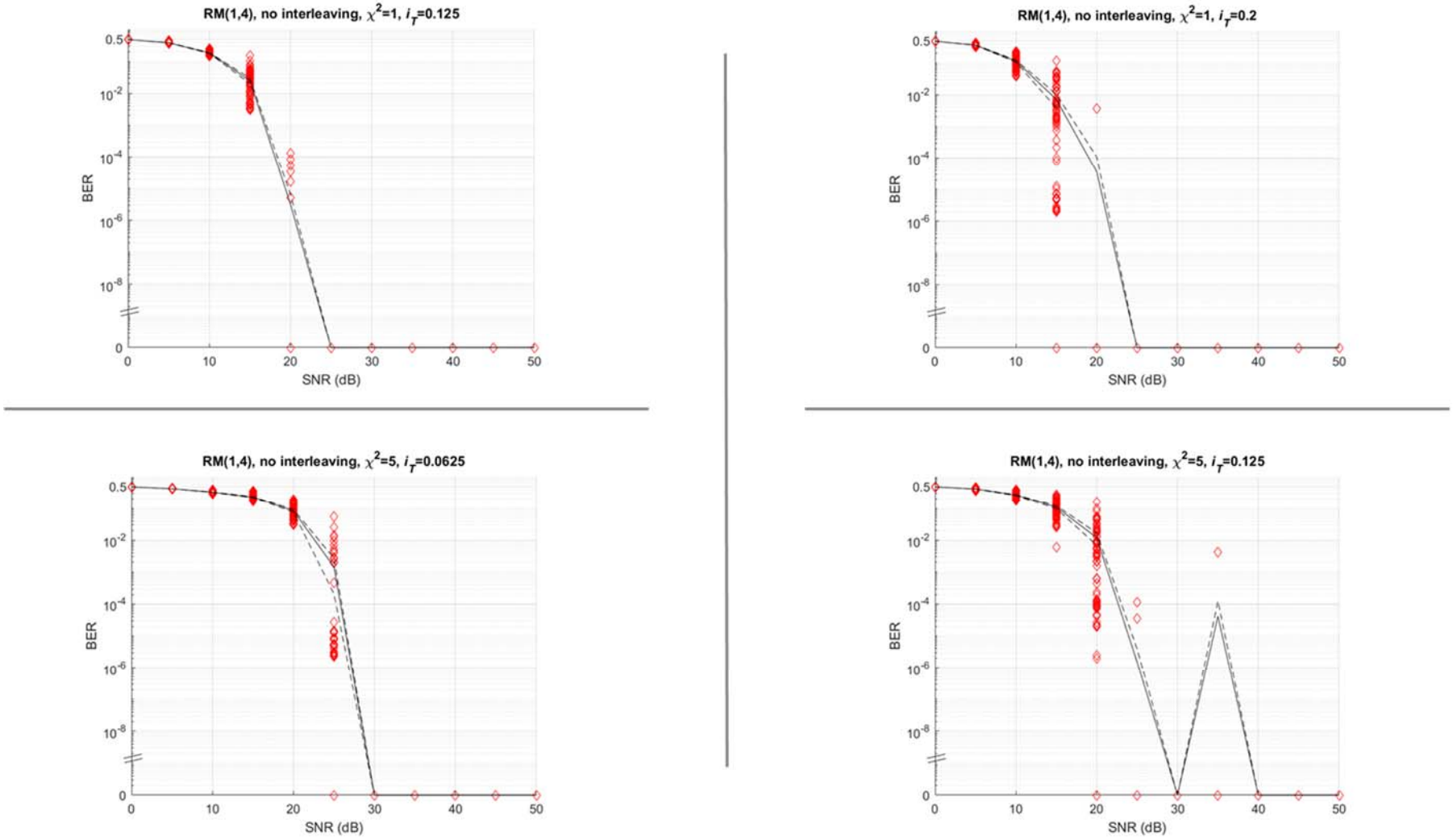

Figure 57. ***RM***(1,4)/***RS***(255,32) Simulation Results (No Interleaver)

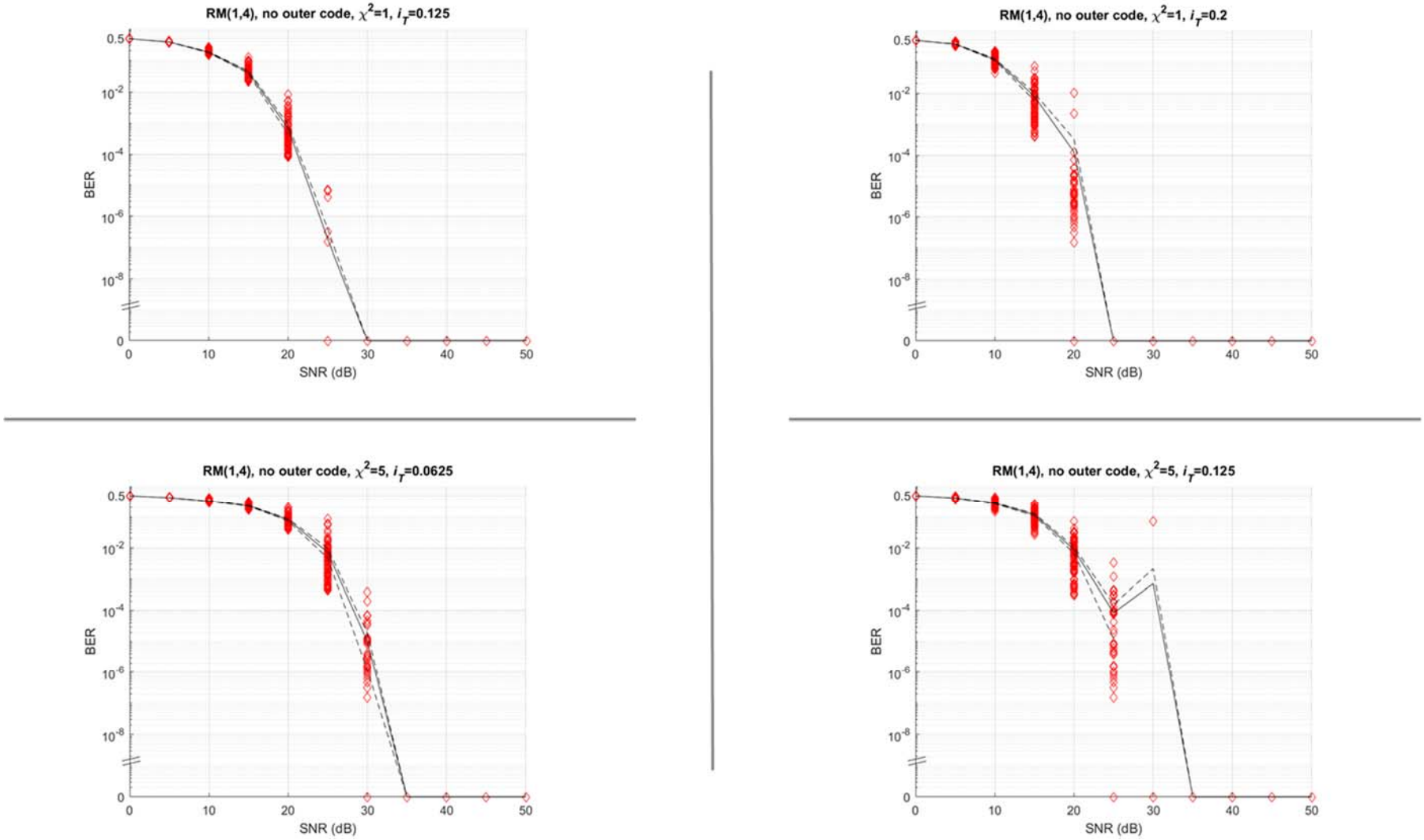

Figure 58. ***RM***(1,4) Simulation Results (No Outer Code)

G. *RM*(1,5)/*RS*(255,32)

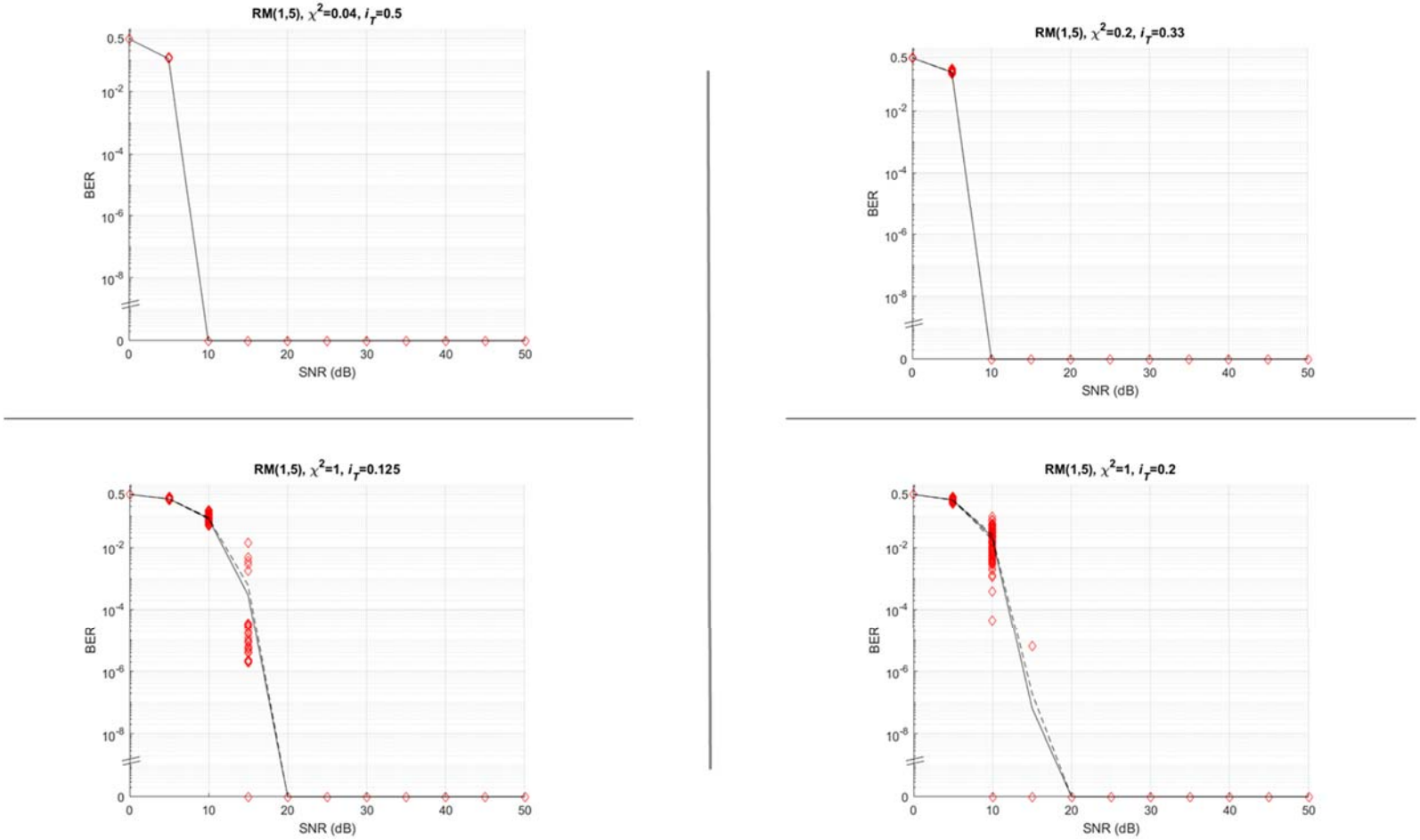

Figure 59. ***RM***(1,5)/***RS***(255,32) Simulation Results

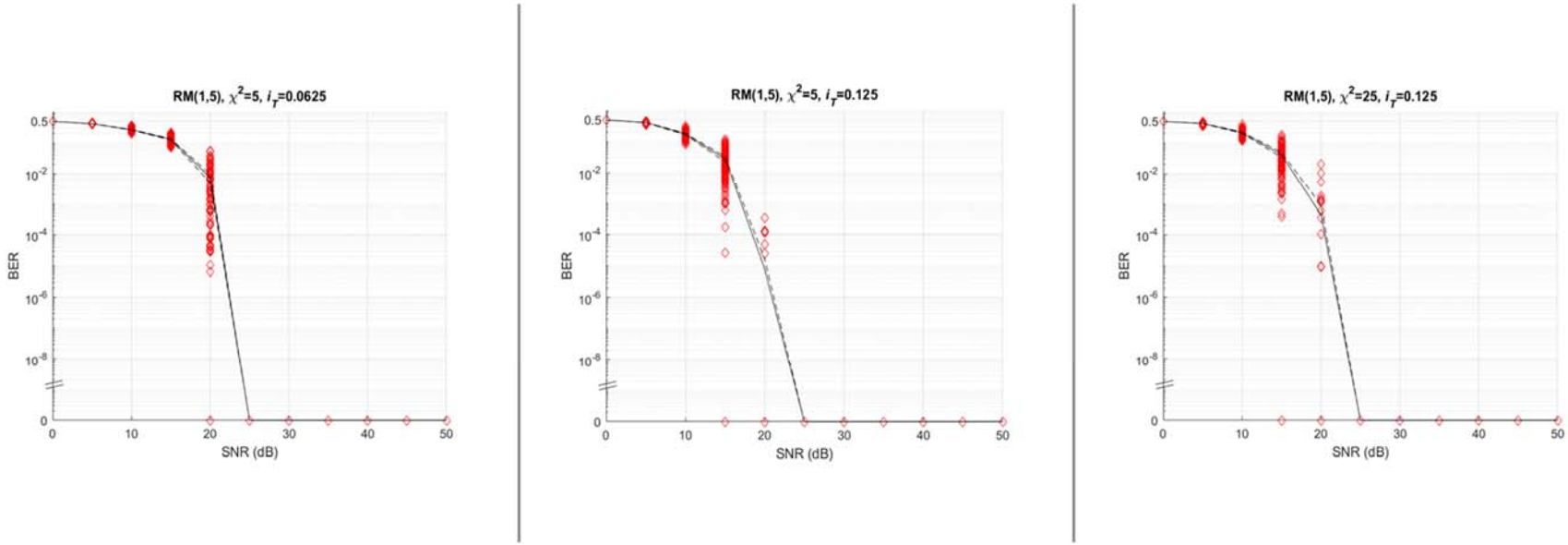

Figure 60. ***RM***(1,5)/***RS***(255,32) Simulation Results (Continued)

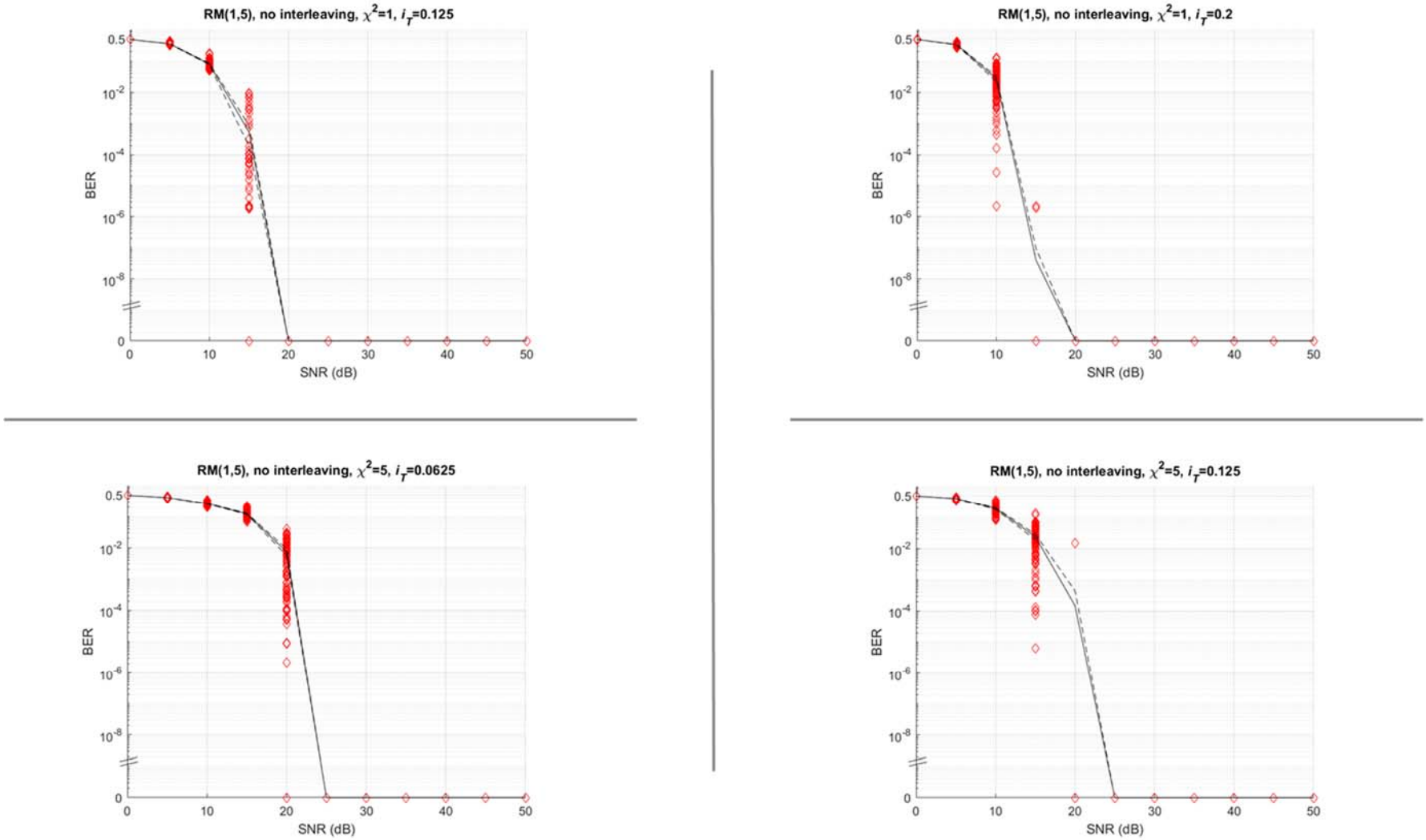

Figure 61. ***RM***(1,5)/***RS***(255,32) Simulation Results (No Interleaver)

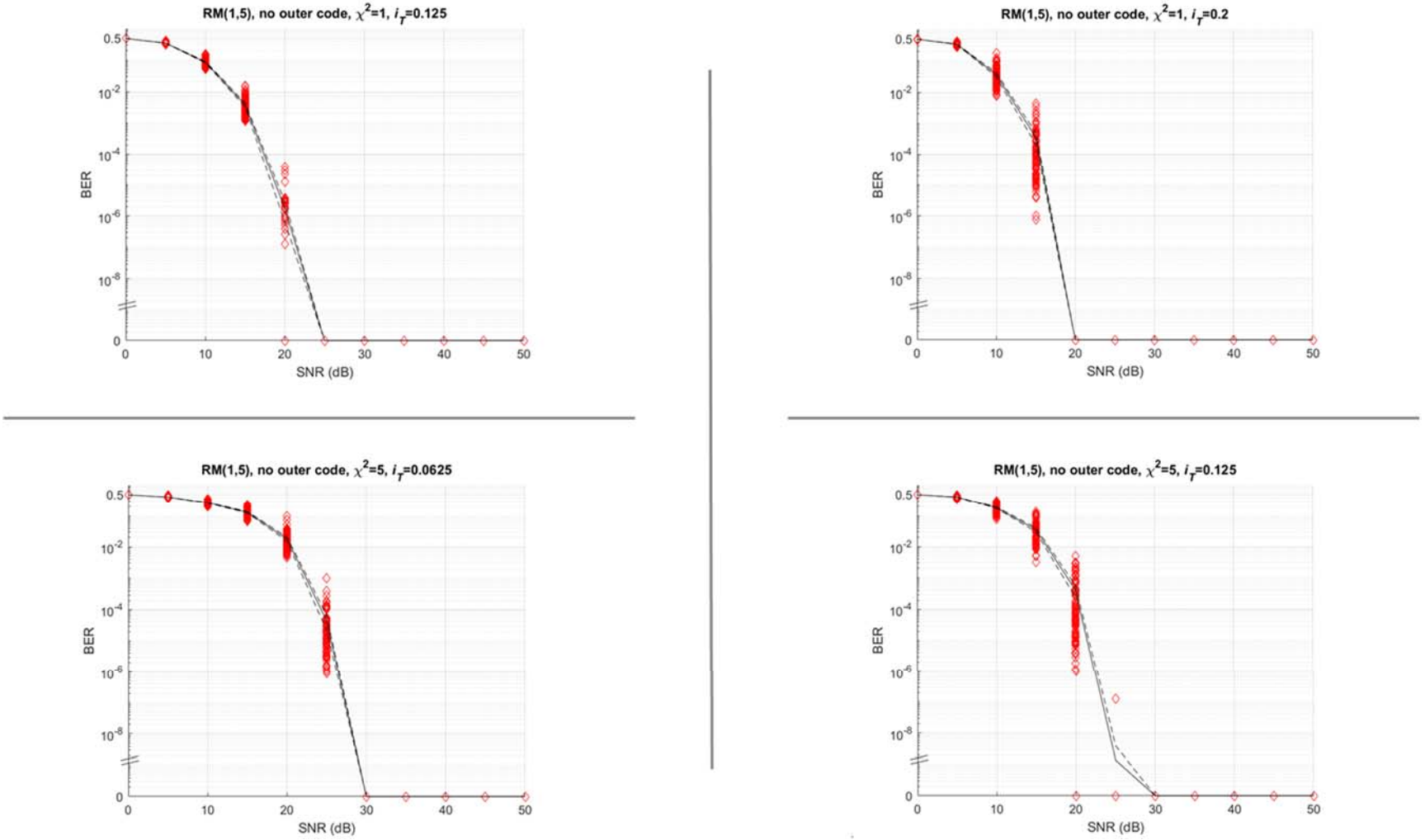

Figure 62. ***RM***(1,5) Simulation Results (No Outer Code)

H. *NR*/*RS*(255,32)

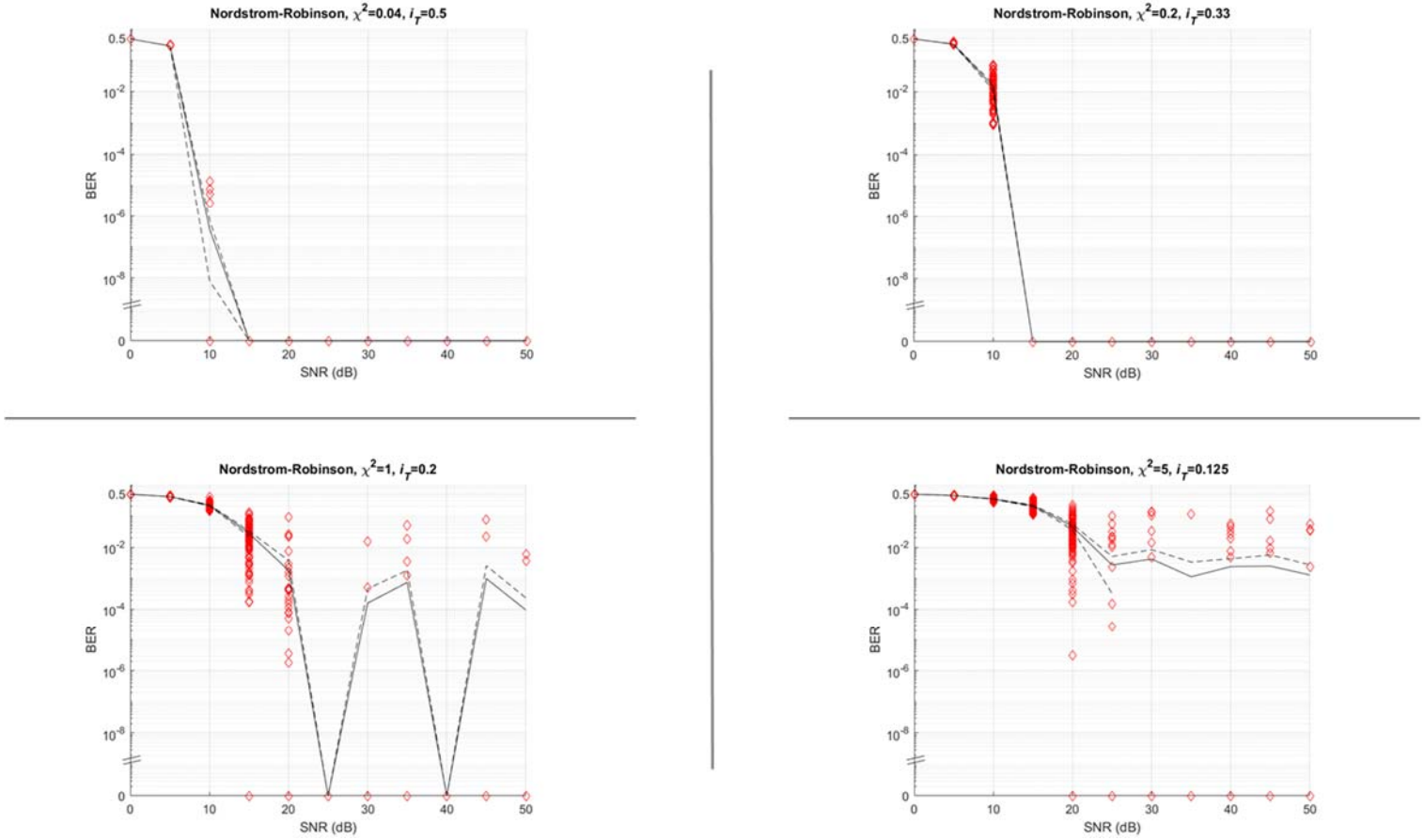

Figure 63. ***NR***/***RS***(255,32) Simulation Results

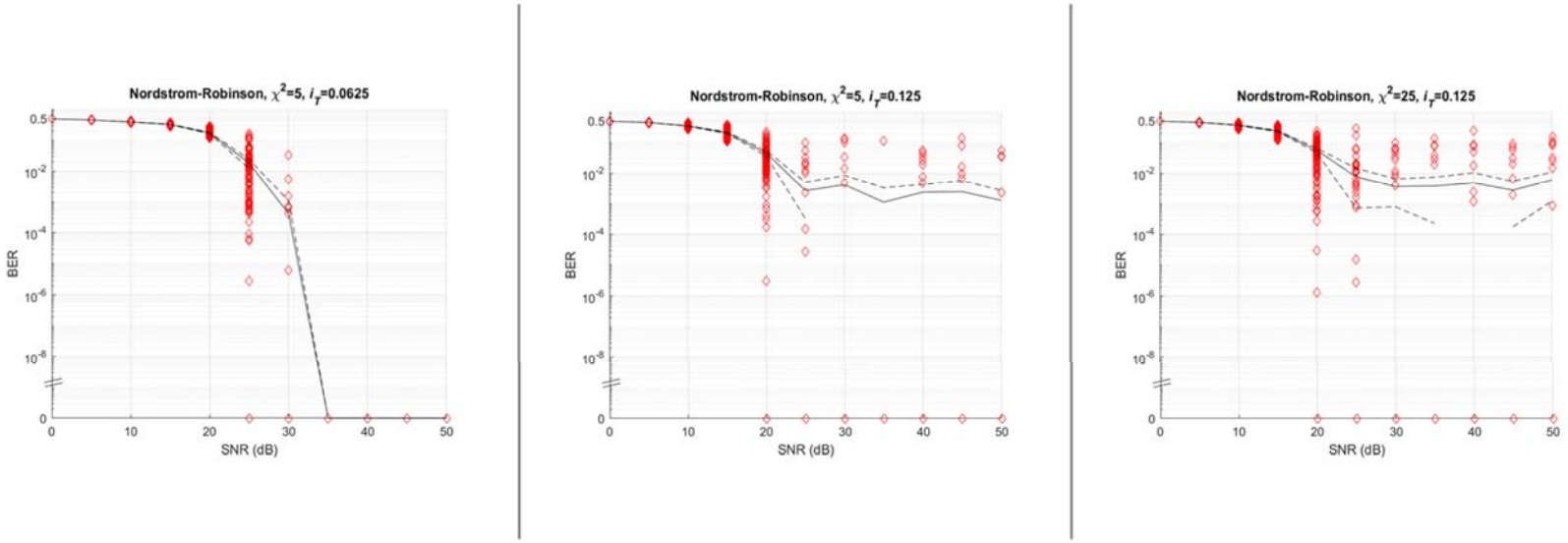

Figure 64. ***NR***/***RS***(255,32) Simulation Results (Continued)

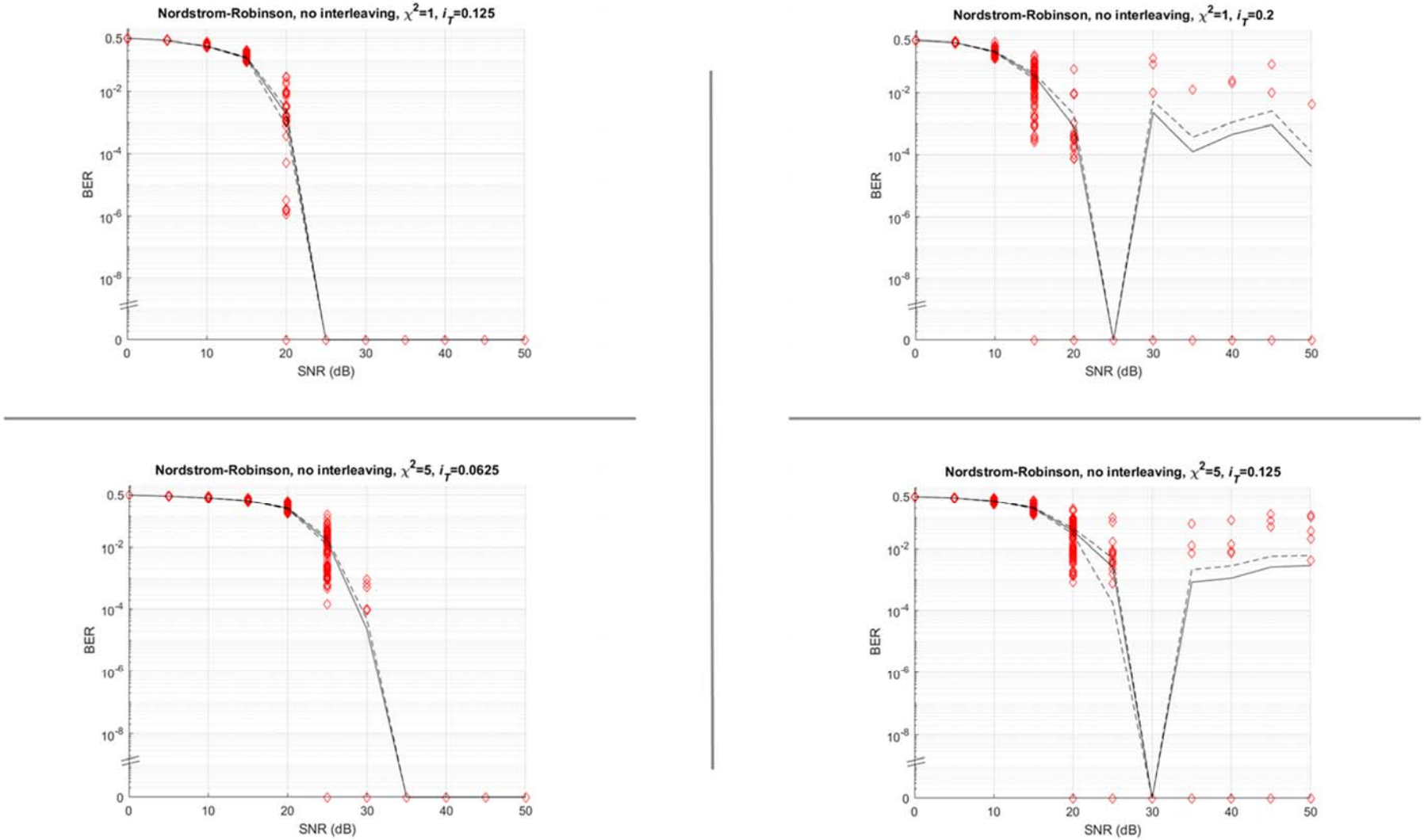

Figure 65. ***NR*/*RS***(255,32) Simulation Results (No Interleaver)

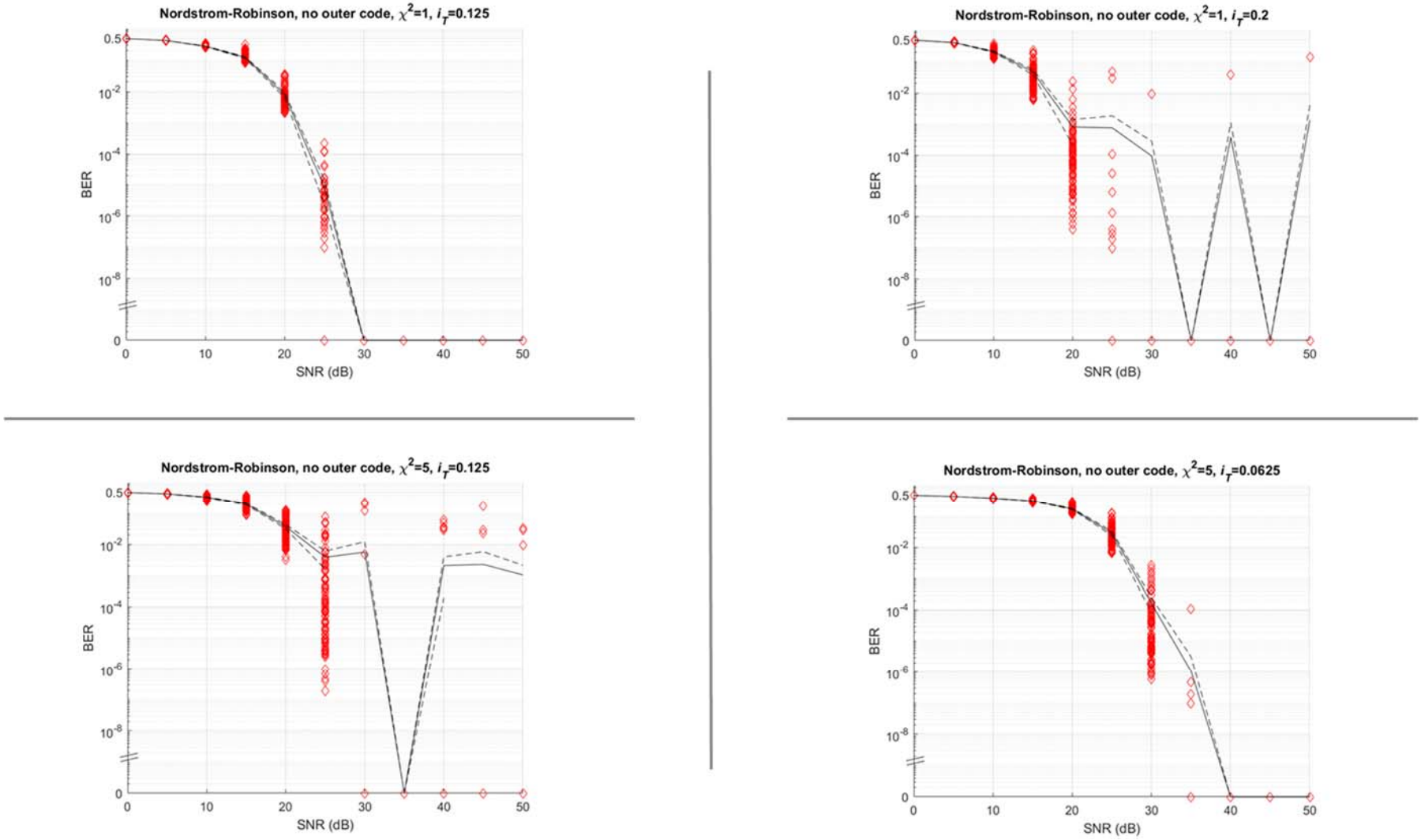

Figure 66. ***NR*** Simulation Results (No Outer Code)

I. G_{24}/*RS*(255,32)

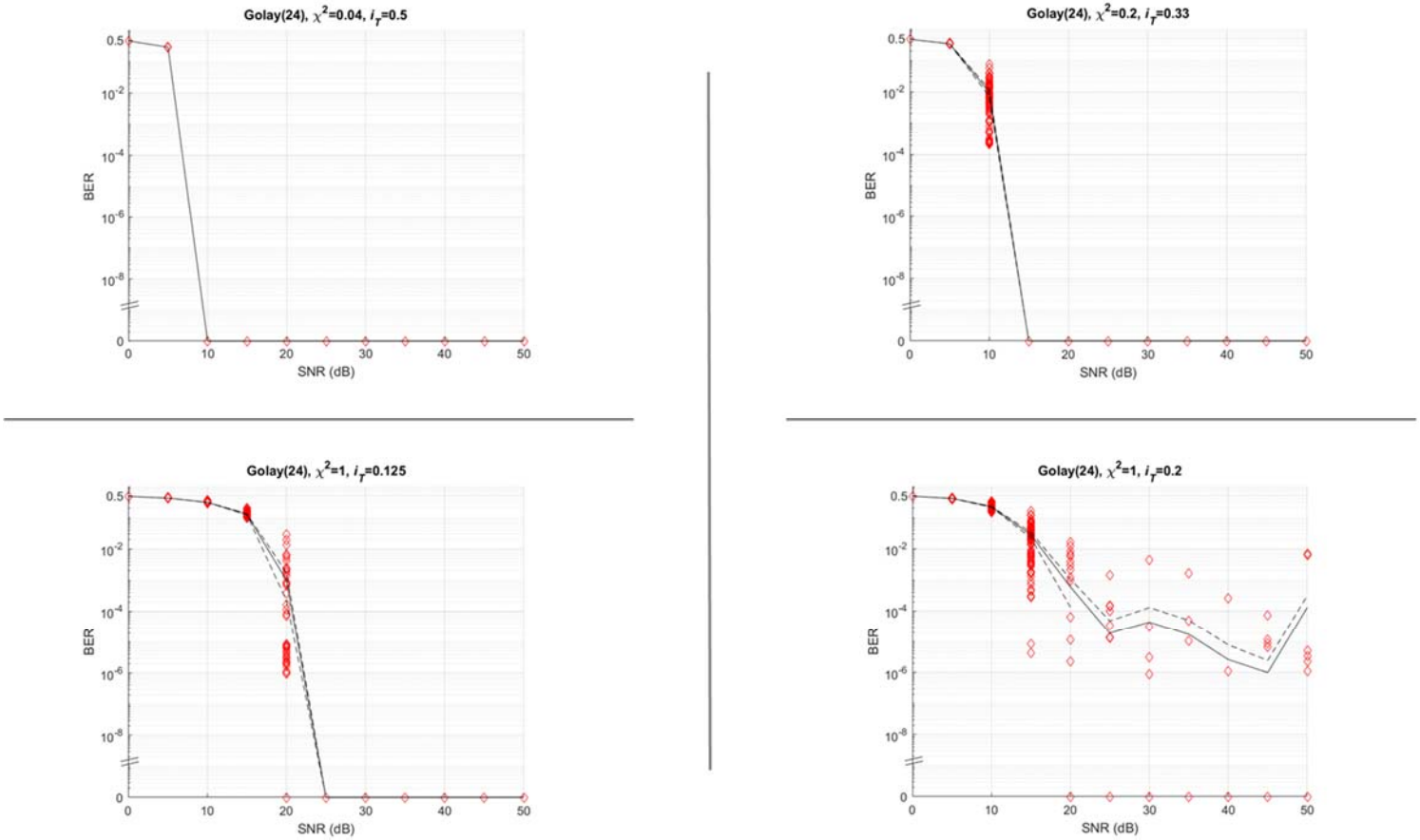

Figure 67. G_{24}/*RS*(255,32) Simulation Results

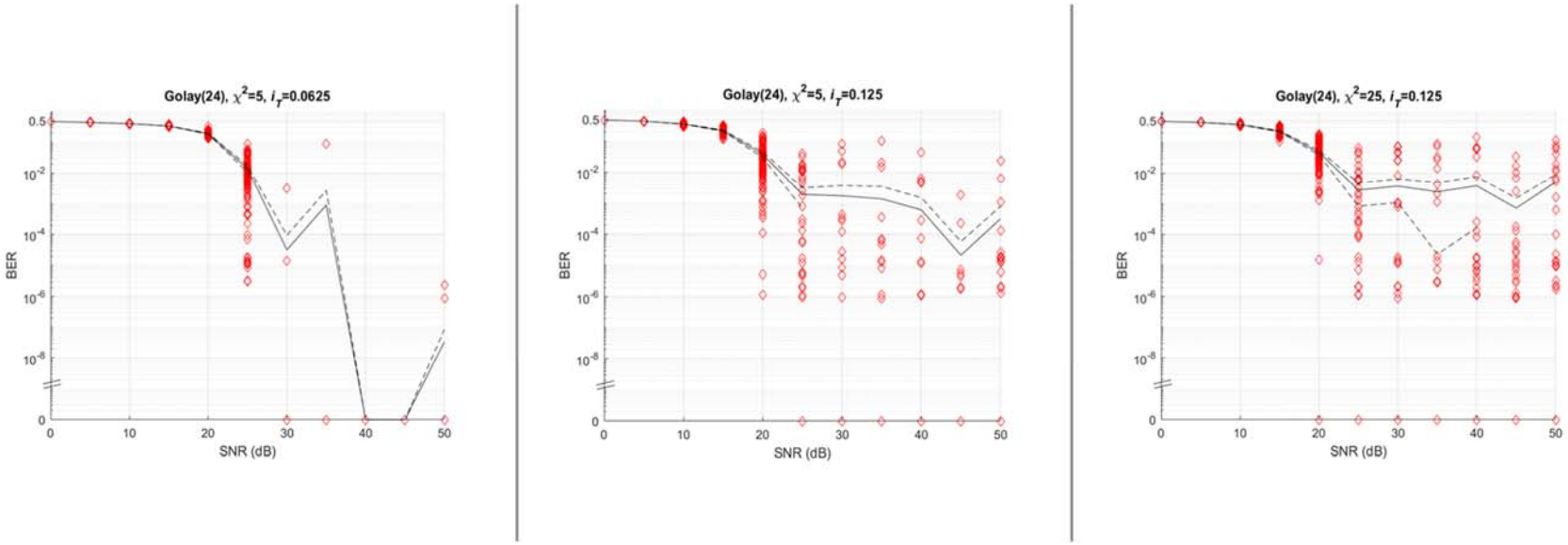

Figure 68. $\boldsymbol{G}_{24}/\boldsymbol{RS}(255,32)$ Simulation Results (Continued)

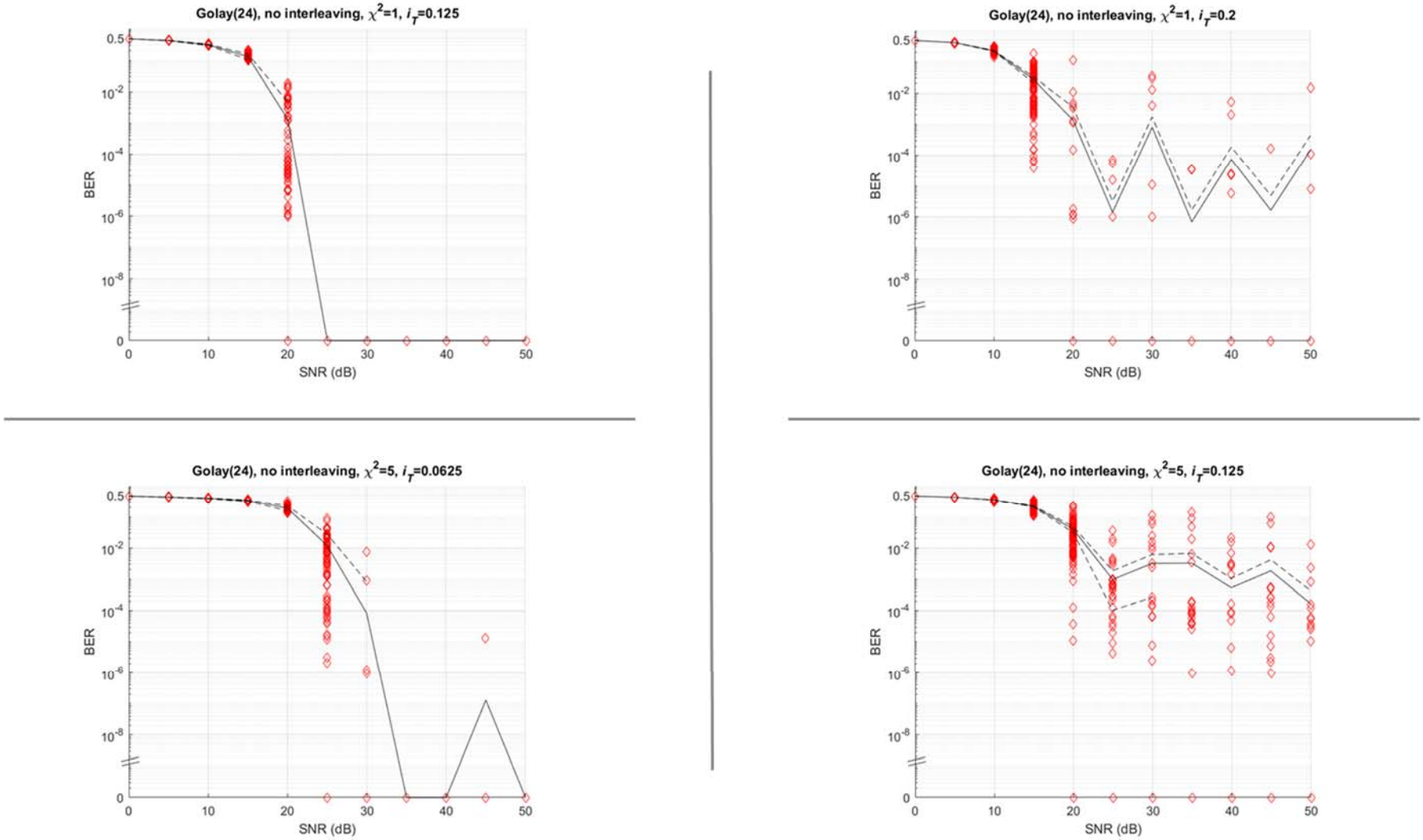

Figure 69. $\boldsymbol{G}_{24}/\boldsymbol{RS}(255,32)$ Simulation Results (No Interleaver)

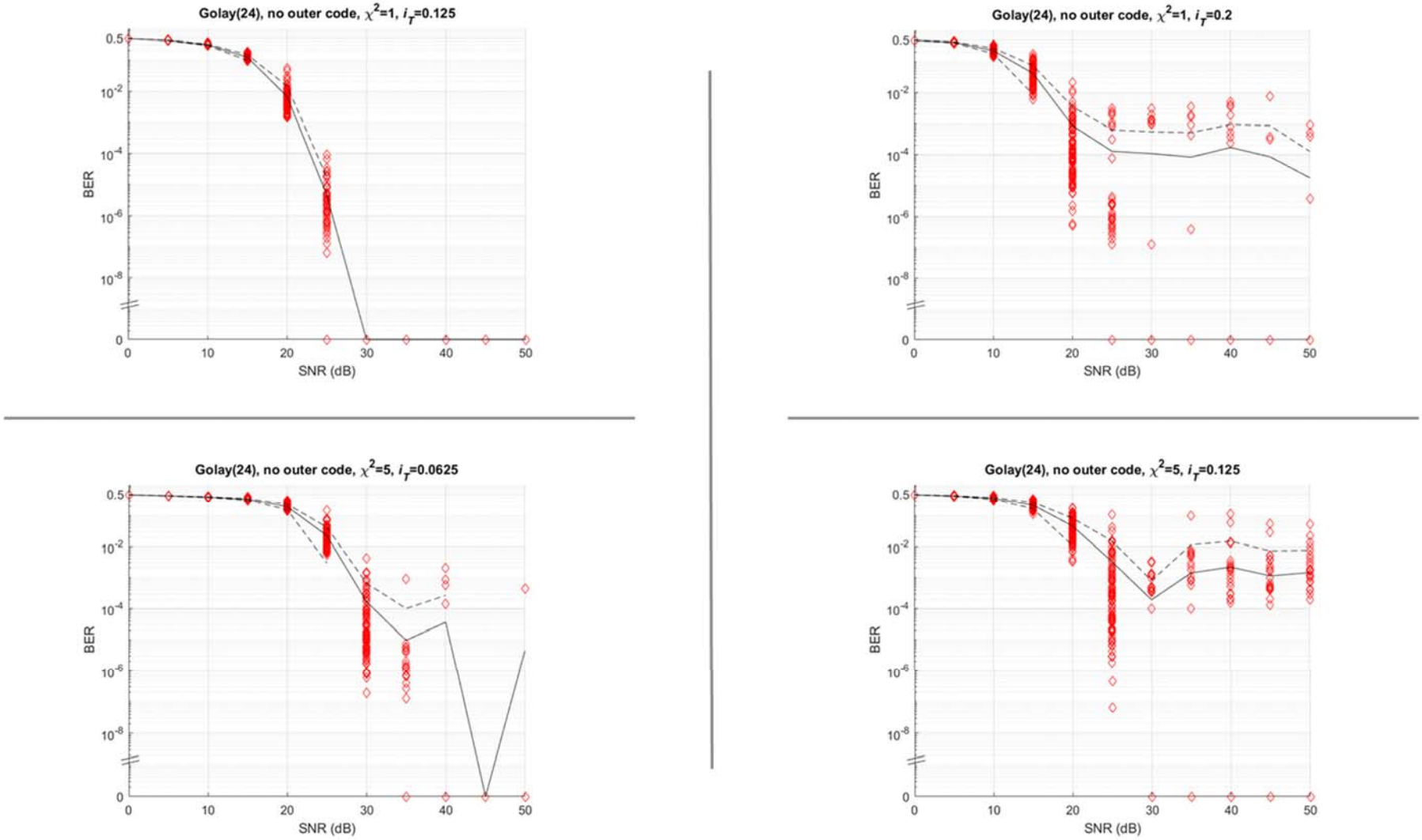

Figure 70. $\boldsymbol{G}_{24}$ Simulation Results (No Outer Code)

J. *REPETITION*(8)

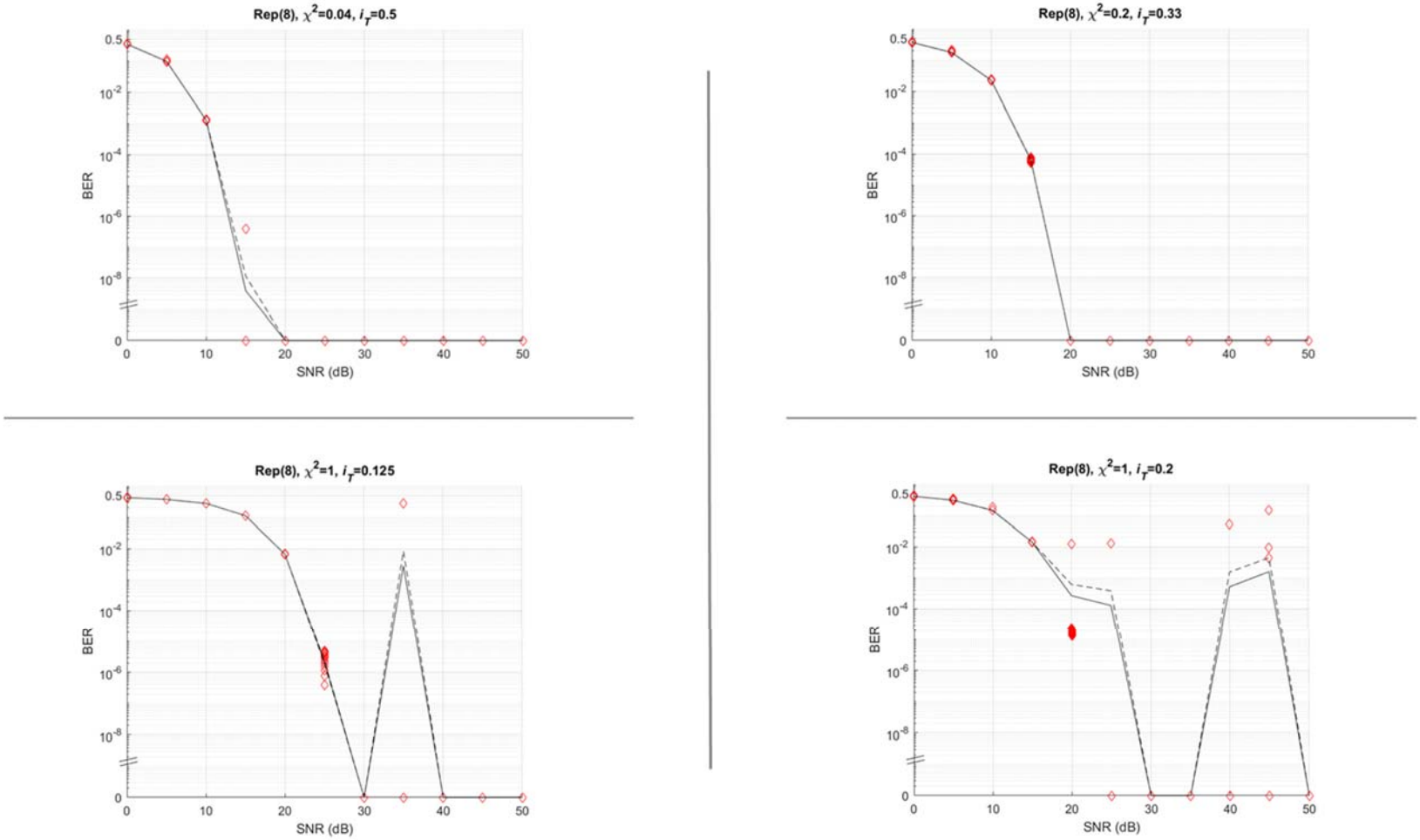

Figure 71. $\boldsymbol{R}_8$ Simulation Results

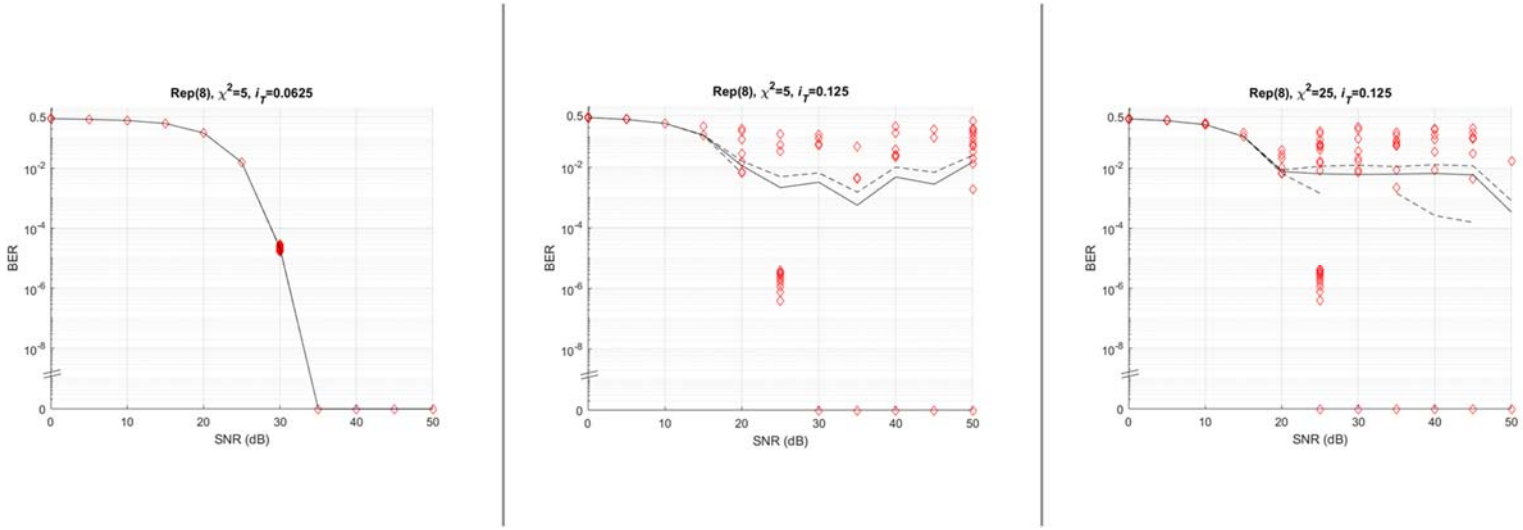

Figure 72. $\boldsymbol{R}_8$ Simulation Results (Continued)

K. *REPETITION*(16)

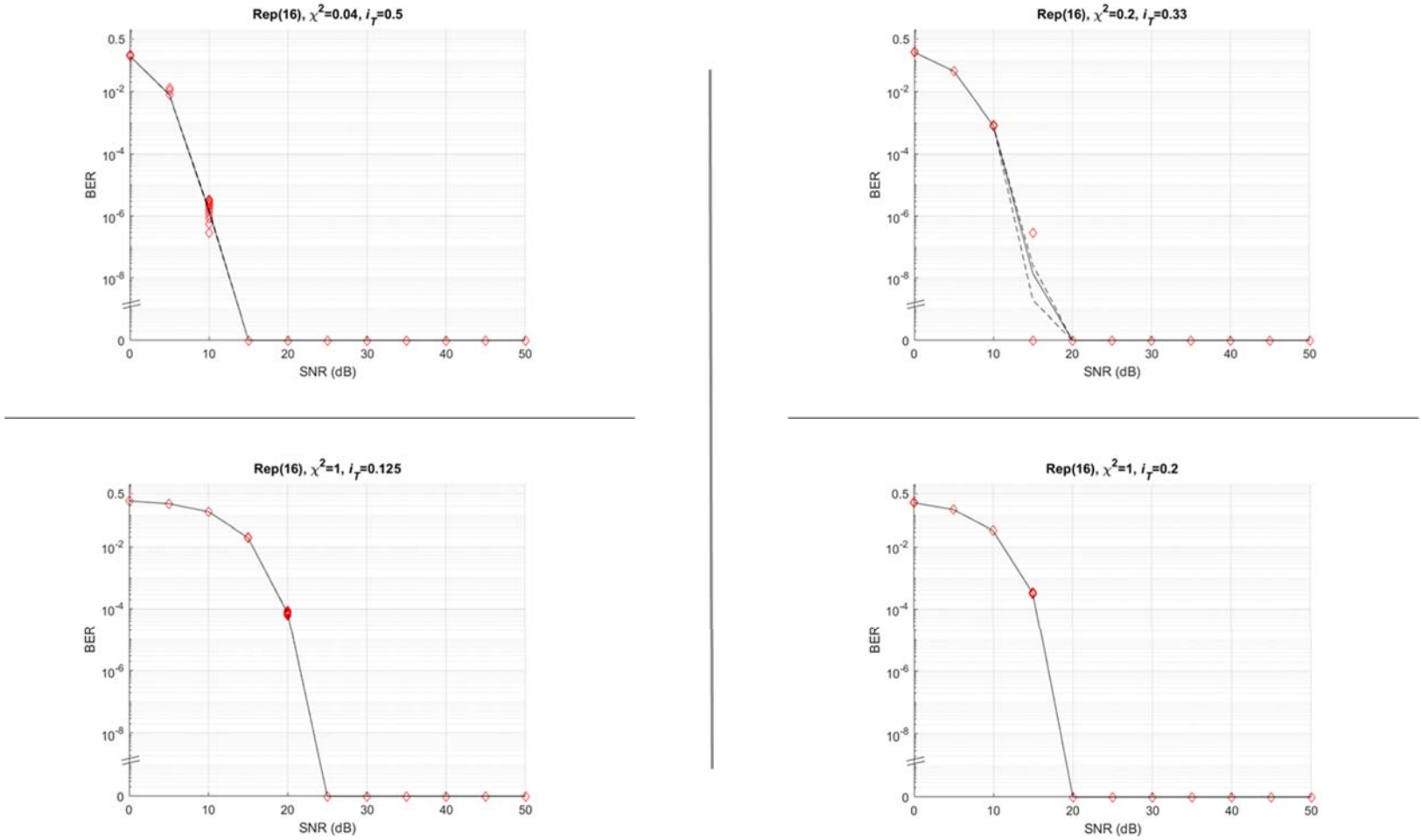

Figure 73. $\boldsymbol{R}_{16}$ Simulation Results

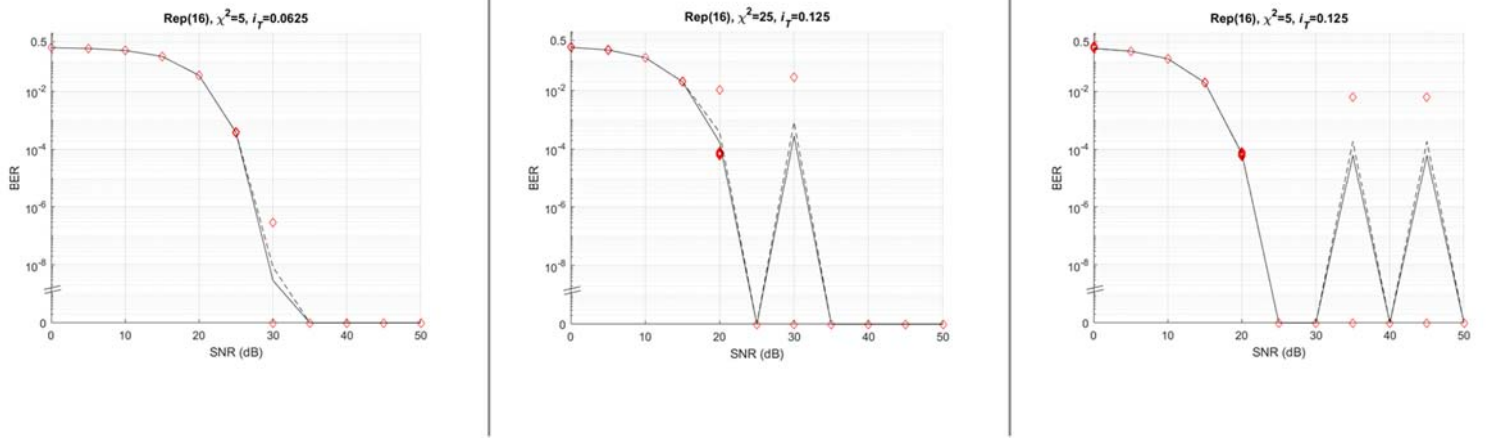

Figure 74. $\boldsymbol{R}_{16}$ Simulation Results (Continued)

L. *REPETITION*(24)

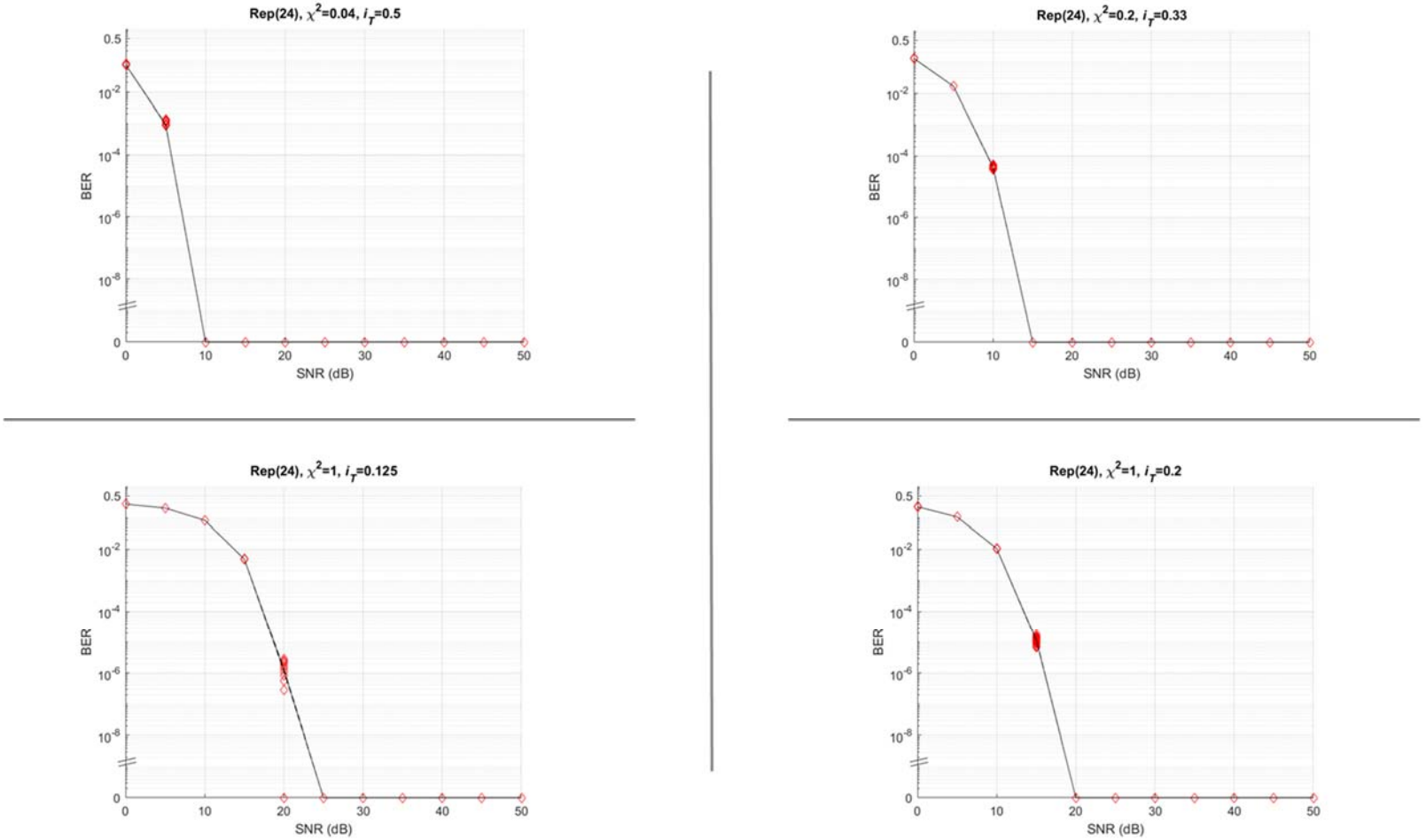

Figure 75. $\boldsymbol{R}_{24}$ Simulation Results

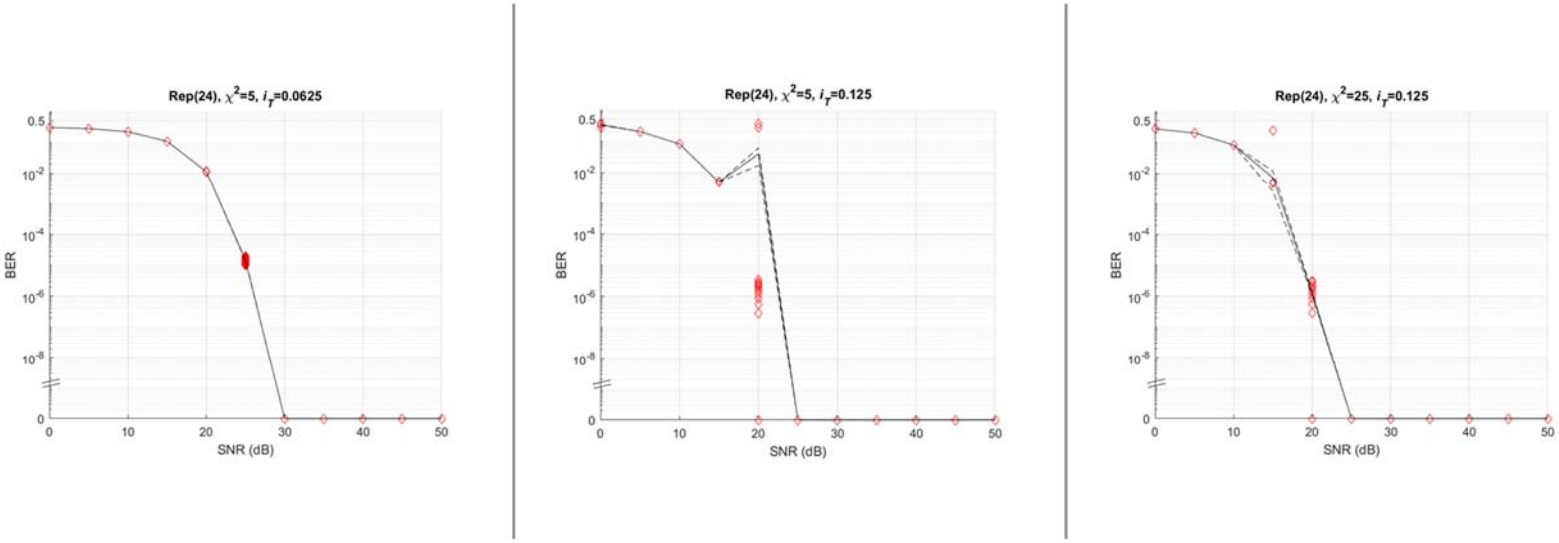

Figure 76. $\boldsymbol{R}_{24}$ Simulation Results (Continued)

M. *REPETITION*(32)

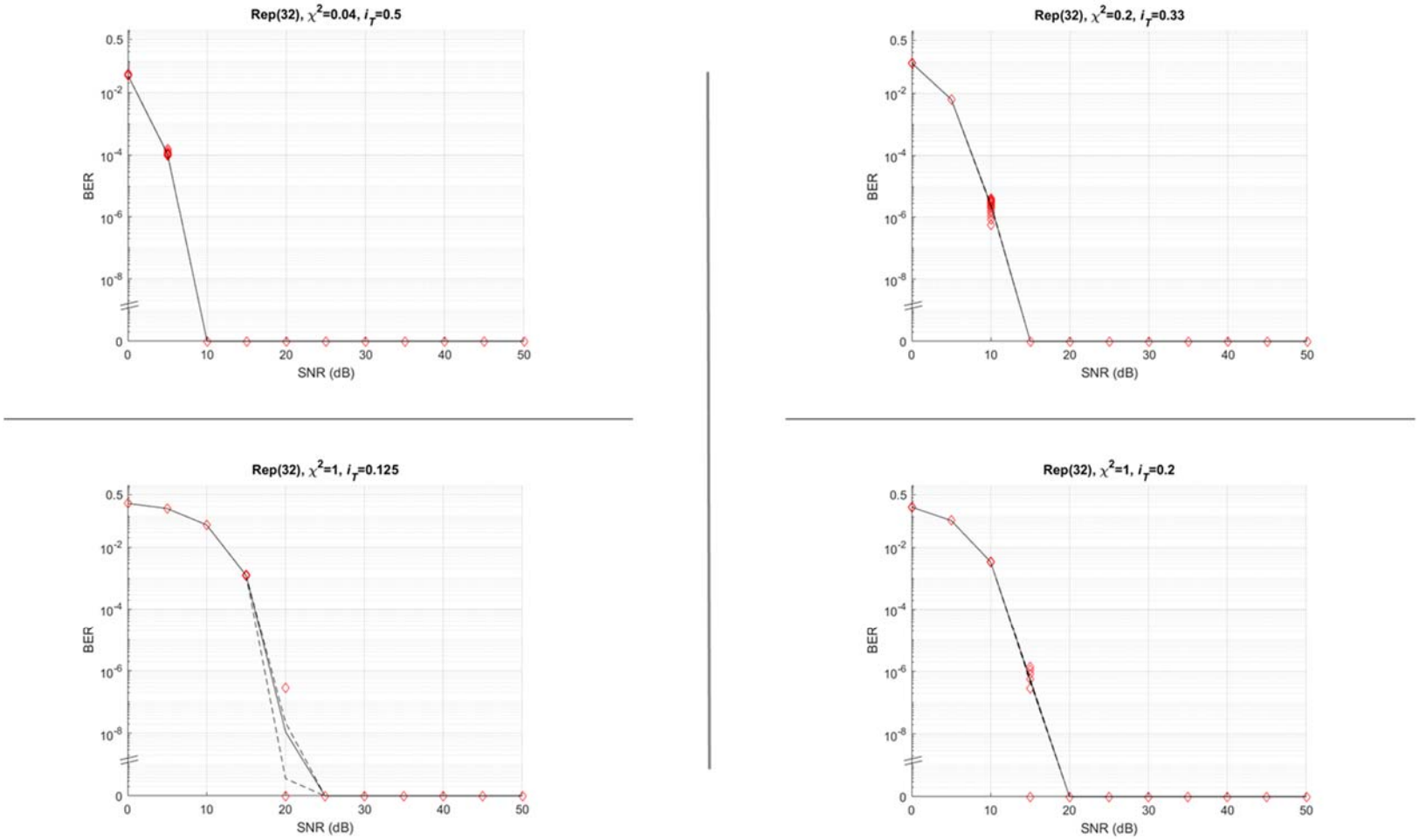

Figure 77. $\boldsymbol{R}_{32}$ Simulation Results

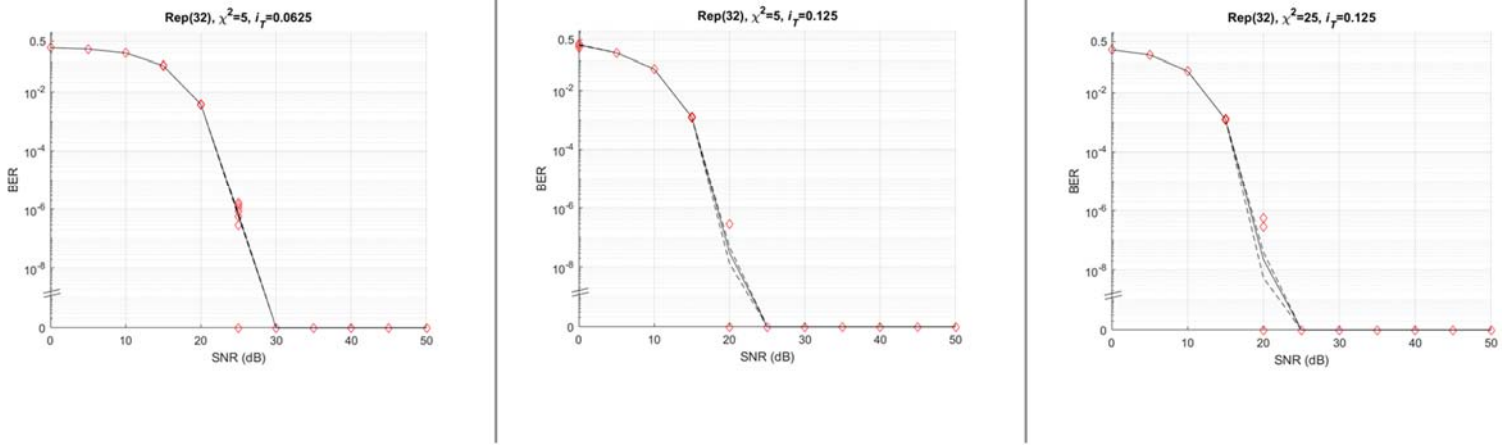

Figure 78. $\boldsymbol{R}_{32}$ Simulation Results (Continued)

THIS PAGE INTENTIONALLY LEFT BLANK

LIST OF REFERENCES

Adoul, J. P. (1987). Fast ML decoding algorithm for the Nordstrom-Robinson code. *IEEE Transactions on Information Theory, IT-33*(8), 931–933.

Ahmed, N., Katabi, D., Perli, S. D. (2010). PixNet: Interference-free wireless links using LCD-camera pairs. *Proceedings of the Sixteenth Annual International Confierence on Mobile Computing and Networking,* 137–148.

Akella, J., Yukse., M., & Kalyanaraman, S. (2007, June 10). *Multi-channel communication in free-space optical networks for the last-mile.* Presented at 15th IEEE Workshop on Local and Metropolitan Area Networks, Princeton, NJ. https://doi.org/10.1109/LANMAN.2007.4295973

Al-Habash, M. C., Andrews, L. C., & Phillips, R. L. (2001). Mathematical model for the irradiance probability density function of a laser beam propagating through turbulent media. *Optical Engineering, 40*(8), 1554–1562.

Alouini, M.S., Gao, X., Yang, L. (2014). Performance analysis of free-space optical communication systems with multiuser diversity over atmospheric turbulence channels. *IEEE Photonics Journal, 6*(2).

Andrews, L. C., Halbing, R. D., Hershberger, C. R., Stalder, J. A., Phillips, R. L. (2004). Fading effects due to scintillation caused by atmospheric turbulence in a wireless optical communication link. *Proceedings of the Society of Photo-Electric Instrumentation Engineering, 5160,* 33–43.

Andrews, L. C., & Phillips, R. L. (2005). *Laser beam propagation through random media* (2nd ed.). Bellingham, WA: The Society of Photo-Optical Instrumentation Engineers.

Anguita, J. A., Djordjevic, I. B., Neifeld, M. A., Vasic, B. V. (2005). *Journal of Optical Networking, 4*(9) 586–601.

Ashikhmin, A. E., Litsyn, S. N. (1995). Fast decoding algorithms for first order Reed-Muller and related codes. *Designs, Codes and Cryptography, 7*(3), 187–214.

Berlekamp, E. R. (1971). Coding theory and the Mathieu group. *Information and Control, 18,* 40–64.

Berrou, C. (2010). *Codes and turbo codes.* Paris: Springer-Verlag.

Blahut, R. E. (2003). *Algebraic codes for data transmission.* Cambridge, UK: Cambridge University Press.

Bourennane, S., Caussé, P., Khalighi, M. A., Xu, F. (2008). Performance of coded time-diversity free-space optical links. *24th Biennial Symposium on Communications,* 146–149.

Bucaille, S., Davidson, F. M., Ricklin, J. C. (2004). Performance loss factors for optical communication through clear air turbulence. *Proceedings of the Society of Photo-Electric Instrumentation Engineering, 5160,* 1–12.

Carlson, A. B., & Crilly, P. B. (2010). *Communication systems: an introduction to signals and noise in electrical communication.* New York, NY: McGraw-Hill.

Carrasco, R. A., & Johnston, M. (2008). *Non-binary error control coding for wireless communication and data storage.* Hoboken, NJ: John Wiley & Sons, Inc.

Chan, V. W. S. (2006). Free-space optical communications. *Journal of Lightwave Technology, 24*(12), 4750–4762.

Chan, V. W. S., & Lee, E. J. (2004). Part 1: Optical communication over the clear turbulent atmospheric channel using diversity. *IEEE Journal on Selected Areas in Communications, 22*(9), 1896–1906.

Chatzidiamantis, N. D., Karagiannidis, G. K., Kriezis, E. E., Michalopoulos, D. S., & Schober, R. (2013). Relay selection protocols for relay-assisted free-space optical systems. *Journal of Optical Communications Networks, 5*(1).

Cheng, J., Holzman, J. F., Yang, L. (2013). Performance of convolutional coded OOK IM/DD systems over strong turbulence channels. *2013 International Conference on Computing, Networking and Communications Workshop on Computing, Networking and Communications,* 35–39.

Cheol-ho, C., Eun-dong, S., Nam-kyu, L., & Tack-don, H. (2006). *U.S. Patent No. 7020327B2.* Washington, D.C: U.S. Patent and Trademark Office. Retrieved from https://patents.google.com/patent/US7020327B2/en

Comer, D. E. (2015). *Computer networks and internets* (6th ed.). Essex, UK: Pearson Education, Ltd.

Davidson, F. M., & Koh, Y. T. (1988). Interleaved convolutional coding for the turbulent atmospheric optical communication channel. *IEEE Transactions on Communications, 36*(9), 993–1003.

Denso Wave. (n.d.). Information capacity and versions of the QR code. Retrieved May 13, 2019, from https://www.qrcode.com/en/about/version.html

Djordjevic, I. B., Neifeld, M. A., Vasic, B. (2006). Multilevel coding in free-space optical MIMO transmission with Q-ary PPM over the atmospheric turbulence channel. *IEEE Photonics Technology Letters, 18*(14), 1491–1493.

Fafalios, M. E., Karagianni, E. A., Nistazakis, H. E., Tombras, G. S., & Tsigopoulos, A. D. (2009). Average capacity of optical wireless communication systems over atmospheric turbulence channels. *Journal of Lightwave Technology, 27*(8) 974–979.

Fath, T., Schubert, F., & Haas, H. (2014). Wireless data transmission using visual codes. *Photonic Research, 2*(5), 150–160.

Felder, A.W. (2018). *Array based free space optic system for tactical communications* (Master's thesis). Retrieved from https://calhoun.nps.edu/handle/10945/59655

Golay, M. J. E. (1949). Notes on digital coding. *Proceedings of the IRE, 37*, 667.

Hao, T., Xing, G., & Zhou, R. (2012). COBRA: Color barcode streaming for smartphone systems. *Proceedings of the 10th International Conference on Mobile Systems, Applications, and Services*, 85–98.

Hamming, R. W. (1950). Error detecting and error correcting codes. *The Bell System Technical Journal, 29*(2), 147–160.

Holmes, J. K., Reed, I. S., Truong, T. K., & Yin, X. (1988). A simplified procedure for decoding the (23,12) and (24,12) Golay codes. *The Telecommunications and Data Acquisition Progress Report*, *42–96*, 49–58.

International Standards Organization (2015). *Information technology -- Automatic identification and data capture techniques -- QR Code bar code symbology specification* (ISO/IEC 18004:2015). https://www.iso.org/standard/62021.html

Jain, V. K., & Parikh, J. (2011). Study on statistical models of atmospheric channel for FSO communication link. Paper presented at the Nirma University International Conference on Current Trends in Technology, Ahmedabad, Gujarat, India. https://doi.org/10.1109/NuiConE.2011.6153263

Javornik, T., Jelovcan, I., Koudelka, O., Leitgeb, E., Muhammad, S. S. (2007, April). Reed Solomon coded PPM for terrestrial FSO links. Paper presented at 2007 International Conference on Electrical Engineering, Lahore, Pakistan. https://doi.org/10.1109/ICEE.2007.4287281

Kaushal, H. & Kaddoum, G. (2015). Free space optical communication: Challenges and mitigation techniques. arXiv:1506.04836 [cs.IT]

Khatoon, A., Cowley, W. G., & Letzepis, N. (2011, January 31). *Channel measurement and estimation for free space optical communications.* Presented at 2011 Australian Communications Theory Workshop, Melbourne, VIC, Australia.

Kienle, F. (2014). *Architectures for signal baseband processing.* New York, NY: Springer.

Kudekar, S., Kumar, S., Mondelli, M., Pfister, H. D., Sasoglu, E., & Urbanke, R. L. (2017). Reed-Muller codes achieve capacity on erasure channels. *IEEE Transactions on Information Theory, 63*(7), 4298–4316.

Lucas, A. R. (2013). *Digital Semaphore: Technical Feasibility of QR Code Optical Signaling for Fleet Communications* (Master's thesis). Retrieved from https://calhoun.nps.edu/handle/10945/34699

MacWilliams, F. J. & Sloane, N. J. A. (2006). *The theory of error-correcting codes.* Amsterdam, NL: Elsevier BV.

Madhavapeddy, A., Scott, D., Sharp, R., & Upton, E. (2005). Using visual tags to bypass Bluetooth device discovery. *ACM SIGMOBILE Mobile Computing and Communications Review, 9*(1), 41–53.

Majumdar, A. K. (2015). *Advanced free space optics (FSO): A systems approach.* New York: Springer.

Muller, D. E. (1954). Application of boolean algebra to switching circuit design and to error detection. *Transactions of the IRE Professional Group on Information Theory, EC-3*(3), 6–12.

Nordstrom, A. W., & Robinson, J. P. (1967). An optimum nonlinear code. *Information and Control, 11*(5 & 6), 613–616.

Preparata, F. P. (1968). A class of optimum nonlinear double-error-correcting codes. *Information and Control, 13*(4), 378–400.

Reed, I. S. (1954). A class of multiple-error-correcting codes and the decoding scheme. *Transactions of the IRE Professional Group on Information Theory, 4*(4), 38–49.

Reed, I. S., & Solomon, G. (1960). Polynomial codes over certain finite fields. *Journal of the Society for Industrial and Applied Mathematics, 8*(2), 300–304.

Richter, S. P. (2013). *Digital semaphore: Tactical implications of QR code optical signaling for fleet communications* (Master's thesis). Retrieved from https://calhoun.nps.edu/handle/10945/34727

Roman, S. (1997). *Introduction to coding and information theory.* New York: Springer-Verlag.

Rohs, M. (2005). Visual code widgets for marker-based interaction. *ICDSW '05 Proceedings of the 5th International Workshop on Smart Appliances and Wearable Computing, 5*, 506–513.

Saptharishi, R., Shpilka, A., Volk, B. L. (2016). Efficiently decoding Reed-Muller codes from random errors. *Proceedings of the Forty-Eighth Annual ACM Symposium on Theory of Computing,* 227–235.

Sari, M. (1997). *Designing fast Golay encoder/decoder in Xilinx XACT with Mentor graphics CAD interface* (Master's thesis). Retrieved from https://calhoun.nps.edu/handle/10945/8225

Schneier, B. (1996). *Applied cryptography: Protocols, algorithms and source code in C* (2nd ed.). Hoboken, NJ: John Wiley & Sons, Inc.

Shannon, C. E and Weaver, W. (1949). *The mathematical theory of communication*. Chicago: University of Illinois Press.

Vardy, A. (1994). The Nordstrom-Robinson code: Representation over GF(4) and efficient decoding. *IEEE Transactions on Information Theory, 40*(5), 1686–1693.

THIS PAGE INTENTIONALLY LEFT BLANK

INITIAL DISTRIBUTION LIST

1. Defense Technical Information Center
   Ft. Belvoir, Virginia

2. Dudley Knox Library
   Naval Postgraduate School
   Monterey, California